University of Southampton

Faculty of Engineering, Science and Mathematics
Optoelectronics Research Centre

Intensity Noise Suppression Using A Semiconductor Optical Amplifier:

Characterisations and Applications

A thesis submitted for the degree of Doctor of Philosophy

by

Anoma Dayawansa McCoy

March 2005

UNIVERSITY OF SOUTHAMPTON

ABSTRACT

FACULTY OF ENGINEERING, SCIENCE & MATHEMATICS
OPTOELECTRONICS RESEARCH CENTRE

Doctor of Philosophy

Intensity Noise Suppression Using a Semiconductor Optical Amplifier: Characterisations and Applications

by Anoma Dayawansa McCoy

In this thesis I present a comprehensive system-level study of the intensity noise suppression offered by a saturated semiconductor optical amplifier (SOA), and its application to high channel count spectrum-sliced and optical code division multiplexed (OCDMA) systems incorporating low-cost incoherent light sources.

The saturated SOA provides significant suppression of the input intensity fluctuations, providing substantial improvement in signal quality. However, narrow, steep roll-off incoherent light spectra experience prominent spectral broadening within the SOA, and I have found that subsequent optical filtering of this broadened output yields increased intensity noise, compromising the benefits of the technique. Correlation characterisations performed on the noise-suppressed light, show strong anticorrelations between the intensity fluctuations of the constituent spectral components. The observed increase in noise due to optical filtering, is attributed to the loss of these correlations when the signal spectrum is altered. Numerical simulations show that these adverse effects can be significantly reduced by optimised amplifier design.

The post-SOA filtering effects introduce a design tradeoff between intensity noise and crosstalk in high channel density spectrum-sliced systems. I experimentally characterise this tradeoff, and find the optimum receiver bandwidth for varying channel spacing configurations. The SOA is also characterised for concurrent amplitude modulation, with no observed degradation in noise suppression performance. An investigation of the relative merits of employing the SOA at the receiver, instead of at the transmitter, is also presented.

SOA-based noise reduction is also studied as a means to improve the performance of spectral amplitude coded OCDMA systems. Two-channel system measurements are used to examine SOA per channel, and SOA per chip configurations, with different encoding and decoding filter functions. The SOA per chip approach is seen to provide higher system performance. The feasibility of SOA-based noise reduction for a high channel count OCDMA system is discussed in view of these results.

Preliminary investigations into incorporating a saturated SOA to reduce low frequency noise of a highly coherent fibre distributed feedback laser are also presented.

Table of Contents

List of Figures

List of Tables

Declaration of Authorship

I, Anoma Dayawansa McCoy declare that the thesis entitled *Intensity Noise Suppression Using a Semiconductor Optical Amplifier: Characterisations and Applications* and the work presented in it are my own. I confirm that:

- this work was done wholly or mainly in candidature for a research degree at this University;
- where any part of this thesis has previously been submitted for a degree or any other qualification at this University or any other institution, this has been clearly stated;
- where I have consulted the published work of others, this is always clearly attributed;
- where I have quoted from the work of others, the source is always given. With the exception of such quotations, this thesis is entirely my own work;
- I have acknowledged all main sources of help;
- where the thesis is based on work done by myself jointly with others, I have made clear exactly what was done by others and what I have contributed myself;
- parts of this work have been published. (see *List of publications*).

Anoma D. McCoy
March 2005

Acknowledgements

It is with much gratitude and appreciation that I pause to reflect on the many individuals who have supported me throughout this exciting, illuminating, rewarding, and at times painful journey known as a Ph.D.

Somewhere at the top of this long list of people, is my supervisor, Professor David Richardson, who provided me the very unique opportunity of working here at the ORC. I consider myself fortunate to have been under his supervision and guidance. In particular, I very much appreciate his valuable insight into writing research papers and his patience and encouragement throughout the rough times.

Thank you to Dr. Benn Thomsen for the valuable discussion times, for the eager hands-on lab support, and for 'keeping me on my toes', especially during the early system experiments. I would also like to take this opportunity to thank Dr. Periklis Petropoulos, who has given me advice and feedback numerous times throughout my research, despite his busy schedule. A very special thank you to Dr. Peter Horak for his theoretical support with the numerical model of the SOA which has added much value to the experimental work presented in this thesis. Thank you Peter for the many rewarding technical discussions we have had, and your extensive proofreading of some of the research papers (not to mention the entire thesis).

I would like to thank Dr. Morten Ibsen, our gratings guru, for providing many of the grating filters used in the various characterisations. Having 'voluntarily' taken on the arduous task of being 'Anoma's mentor' he has patiently encouraged me through many a difficult time. I will always be grateful for your support, kindness and friendship throughout these Ph.D. years.

Thanks also to Dr. Peh Chiong Teh for helping me find my way in the lab during my first few months as a new student, and to Dr. Ju Han Lee and Mr. Taichi Kogure

for helpful discussions at numerous times. I would also like to thank Dr. Ron Haaksman for introducing me to the wonderful world of noise measurements and for getting me started with the fringe visibility experiments. Thank you also to Dr. Li Bin Fu for his help with the fibre laser work, and to Dr. Ridzuan Mokhtar for providing the tunable bandwidth grating used in the spectrum-slicing experiments. I would also like to take this opportunity to thank Mr. Chris Nash and Mr. Simon Butler for help on a wide range of activities. A special thank you to our postgraduate student mentor, Dr. Eleanor Tarbox for her valuable support with preparing presentations and patiently proofreading many a boring paper/thesis that has come her way. I would also like to thank our postgraduate coordinator Mrs. Eveline Smith for her ever helpful support and kindness throughout my stay at the ORC.

The many hours in the lab would not have been much fun without the company of the 'systems gang', Michaël, Francesca, Paulo, and Chun, who, I am sure, cannot wait for me to leave so they can finally use all of my amplifiers. I have enjoyed getting to know each of you. A big thank you also to Jo, Ami, and Tanya who through their friendship, helped me get settled into my new surroundings soon after my arrival at the ORC. Thanks also to my office-mates for all the fun times we have had - I will miss you all!

I am also deeply grateful for the support, encouragement and love I have received from my parents and sister throughout the years, in particular for their strong example of hard work and dedication.

Finally at the end of this long list, I acknowledge my greatest support of all, my husband and best friend, Philip McCoy. He has been my chief advisor, primary proofreader, IT-support, late night lab companion, tirade-listener, pizza delivery boy, taxi driver, and much much more. Thank you Phil, for the confidence you have shown in me throughout the years, for moving to England for me, for wholeheartedly sharing this adventure, and above everything, for loving me through it all.

-ADM

Principal Abbreviations

WDM wavelength division multiplexing

EDFA erbium doped fibre amplifier

FWM four wave mixing

SOA semiconductor optical amplifier

ASE amplified spontaneous emission

FBG fibre Bragg grating

PSD power spectral density

RIN relative intensity noise

SNR signal-to-noise ratio

SMF single mode fibre

DFB distributed feedback

CW continuous wave

OCDMA optical code division multiple access

SAC spectral amplitude coding

EOM electro-optic modulator

BER bit error rate

To Phil with Love

I was taught that the way of progress is neither swift nor easy.

- Marie Curie

Chapter 1

Introduction

Within the last ten years, the growth of the Internet has fuelled a dramatic increase in the universal demand for communication capacity, and this burgeoning appetite for bandwidth has spurred rapid technological advances in telecommunication systems worldwide. Since the advent of the erbium doped fibre amplifier (EDFA), dense wavelength division multiplexing (WDM) based long-haul optical links have achieved greater than Tbit/s data rates through a single fibre. Commercial terrestrial systems providing multiple Tbit/s total capacity and covering many thousands of kilometers are now available, allowing a truly global telecommunications infrastructure [1].

However, closer to the end user, metropolitan-area and access networks have been slower to capitalise on the tremendous data bandwidth obtainable with optical fibre systems [2]. Although these networks are less demanding in terms of total system throughput, they require simple, flexible network management and low component and operation costs, while maintaining a high channel count. To date, dense WDM has not been an effective solution for this market [3]. Researchers are investigating alternatives such as coarse WDM [4], spectrum-sliced WDM [5] and optical code division multiple access (OCDMA) [6] to economically address these medium and short-haul network requirements.

One topic that has generated interest in the metro/access community, is the use of low-cost broadband sources which have the potential to allow considerable savings in these markets. A single broadband source located at the central office distribution point, for example, can replace multiple wavelength-specific lasers, while

reducing replacement stock inventory requirements, thus providing a distinct advantage for telecom carriers. Specifically, *incoherent light* sources such as light emitting diodes (LEDs), superluminescent diodes (SLDs) or fibre based amplified spontaneous emission (ASE) sources, have the potential to meet the performance and flexible management requirements of these cost-sensitive metro/access networks [7]. Other benefits of incoherent sources include reduced sensitivity to environmental changes, reduced Brillouin scattering [8], low-coherence[1], and reduced manufacturing cost.

However, a significant disadvantage of incoherent sources is the intensity noise that arises from the random nature of spontaneous photon emission, and is manifested through the square-law characteristics of the photodetection process. One approach to reducing this intensity noise, proposed in the context of spectrum-slicing, is to use the nonlinear signal processing offered by a saturated semiconductor optical amplifier (SOA) [10]. The SOA provides a substantial improvement in signal quality and, through the economy of scale, has the potential to become a low-cost device. Simultaneous use of the SOA for modulation and amplification can provide further system cost savings for the metropolitan and access markets.

However, at the outset of my Ph.D. studies (August 2001), published results in this area were limited to preliminary spectrum-slicing experiments, and thus lacking in detailed system investigations. As such, little was known about the general suitability of this technique for different system applications. In this thesis I present a comprehensive study of the feasibility of SOA-based noise reduction, from a photonic systems perspective, with particular emphasis on its application to spectrum-slicing and OCDMA.

My initial Ph.D. research investigated the performance of SOA-based noise reduction in spectral amplitude coded OCDMA applications. As expected from previously reported experiments, the SOA provided significant noise reduction of the spectrally encoded signal. However, system experiments revealed that spectral decoding at the receiver gave rise to an increase in noise, thus diminishing the noise suppression benefit of the technique. These post-SOA optical filtering effects pose an imped-

[1]Low-coherence is a desirable property for interferometer based OCDMA systems, such as that discussed in [9].

iment to system implementation, which had not been reported prior to my work. Consequently, the emphasis of my research shifted toward examining the underlying physical mechanisms responsible for the signal degradation and exploring system and device optimisations to minimise their effects. This understanding was then used to analyse the performance of SOA-based noise suppression in telecommunication system applications.

As a consequence, this thesis is organised as a logical progression rather than a chronological record. The initial chapters present theoretical background, along with experimental and numerical analysis of intensity noise, nonlinear noise suppression, and post-SOA filtering effects. Subsequent chapters report system characterisations of SOA-based noise suppression in spectrum-slicing and OCDMA applications.

Thesis Outline

Chapter 2 begins with a review of the properties of narrowband incoherent light, with particular emphasis on the relationship between the spectral profile and intensity noise level. Theoretical predictions were confirmed by experimental measurements and numerical simulations, providing a baseline for evaluating intensity smoothed light in subsequent chapters.

The use of a gain-saturated SOA for noise suppression of incoherent light is examined in Chapter 3, where measurements and numerical analysis are used to characterise the nonlinear noise suppression process. I show that the improvement in signal quality is accompanied by spectral distortion, which renders it susceptible to deterioration in the presence of subsequent optical filtering. Experimental and numerical results are used to verify the hypothesis that the observed increase in intensity noise originates in the loss of intensity correlation between spectral components of the SOA output when the signal spectrum is modified. I also investigate methods of overcoming these post-SOA filtering effects using system and device design optimisations.

In Chapter 4, I discuss the feasibility of using SOA-based noise reduction in spectrum-slicing applications, in view of the broadening and spectral filtering effects. The increase in noise due to receiver filtering is quantified in terms of Q, and the associated system penalty is assessed. Despite the signal degradation caused by

post-SOA optical filtering, narrow receiver filters are required to reduce the crosstalk in high channel density spectrum-sliced systems. I characterise this tradeoff in a three-channel spectrum-sliced system and show that an optimum receiver filter bandwidth exists for which the crosstalk and intensity noise counterbalance. The noise suppression performance of the SOA, when used as a modulator, is also assessed. The chapter concludes with a comparative study of several different system configurations that have been proposed for SOA-based noise suppression in spectrum-slicing.

Chapter 5 introduces spectral amplitude coded OCDMA, providing a comprehensive literature review of the historical development of this technique. OCDMA using incoherent light is suited to the flexibility requirements of cost-sensitive metro/access networks, and provides additional benefits of asynchronous transmission, high spectral efficiency, and increased security between users [9]. Experimental results are presented for three different two-channel system configurations, using custom fibre Bragg gratings (FBGs) to perform the encoding and decoding functions. System and grating design optimisations are investigated to minimise the adverse effects of spectral decoding. I conclude this chapter by discussing the feasibility of the technique for low-cost applications.

Although the main focus of this thesis is the feasibility of SOA-based noise reduction for communication systems, it is to be appreciated that the gain-saturated SOA is in fact a powerful and versatile tool that has potential in several key areas where low-noise, high sensitivity and high accuracy are highly desirable. In Chapter 6, I present the first demonstration of the use of a saturated SOA to reduce the low frequency noise of a highly coherent fibre distributed feedback laser, for sensor applications. A substantial reduction of the relaxation oscillation noise peak was achieved. In contrast to the incoherent light scenario, I show that this suppression was not accompanied by spectral broadening of the laser linewidth, thus enhancing the potential of the technique for high coherence, high stability sensing systems.

The thesis concludes with Chapter 7, where I summarise the key results and discuss directions for future work.

Chapter 2

Intensity Noise of Incoherent Sources

Overview: In this chapter I discuss the characteristics of intensity noise in incoherent sources and examine how this noise is influenced by factors such as source intensity, spectral shape and bandwidth. Experimental results and numerical predictions are used to verify and understand these properties, providing a baseline for evaluating noise suppression techniques presented in subsequent chapters.

2.1 Statistical Properties of Incoherent Light

Light generation by spontaneous emission is the underlying process of the majority of today's common optical sources. Light emitted by such sources, both natural and man-made, is the result of radiation from large collections of excited atoms or molecules as they spontaneously drop down to their lower energy states. The emitted packets of light or photons are generated independently of each other, at random time intervals over a wide spectral range. The individual photons are random in phase, producing light of an *incoherent* nature, frequently referred to as *thermal* light. In contrast, laser light is highly coherent, consisting of well-ordered photons produced through stimulated emissions [11].

Spontaneous emissions are inherently *noisy* by nature, giving rise to random fluctuations of the continuous wave (CW) optical intensity. This intensity noise is caused

by the beating of the randomly phased spectral components that comprise the optical bandwidth [12], and manifests itself through the square-law nature of the photodetection process. Analytically, the complex electric field of thermal light can be expressed in terms of statistically independent Fourier components as given by Equation (2.1), where the integral is calculated across the entire optical bandwidth, $\Delta\nu$, of the source [13].

$$E(t) = \int_{\Delta\nu} \mathbf{E}(\nu) e^{j2\pi\nu t} d\nu \tag{2.1}$$

Here, $\mathbf{E}(\nu) = |E|e^{j\phi}$ is the component of the complex field at frequency ν, and $|E|$ and ϕ are random variables that represent the amplitude and phase of the field oscillation. For polarised light, $|E|$ and ϕ follow the Rayleigh and uniform distributions respectively, while it can be shown that the complex field $E(t)$ at a given point in space and time follows circular Gaussian statistics [11].

The work presented in this thesis primarily concerns narrowband[1] polarised incoherent light. This narrowband light retains the statistical properties of the polarised thermal source as shown in [11, 14], and can thus be described by Equation (2.1), where $\Delta\nu$ now represents the bandwidth of the spectrally filtered signal.

2.2 Measuring Intensity Noise

The intensity noise of an optical signal can be characterised in terms of the power spectral density (PSD) of the detector photocurrent. However, the photocurrent also includes *shot* and *thermal* noise components, which must be taken into consideration to obtain an accurate measurement of the *source* intensity noise[2].

Shot noise is caused by the random arrival times of photons at the detector, and for a PIN photodiode, the shot noise PSD, S_{shot}, is given by Equation (2.2).

[1]Narrowband light refers to bandpass filtered incoherent light where the optical bandwidth is much smaller than the centre frequency.

[2]Intensity noise or beat noise is also sometimes referred to as *excess photon noise*, a term which has been traditionally used to distinguish the added noise component at the detector that arises from the spontaneous nature of incoherent light [12].

$$S_{shot} = 2qI_pR_L \tag{2.2}$$

Here, I_p is the average photocurrent, which relates directly to the input optical power. q and R_L are the electron charge and detector load resistance respectively. *Thermal noise* on the other hand, is independent of the input optical intensity [1], and is produced by the random thermal motion of electrons in the load resistor. Its PSD, $S_{thermal}$, can be described by Equation (2.3), where k_B is the Boltzmann constant and T is the absolute temperature. Note that the power spectral densities of both thermal and shot noise are flat across a wide frequency range, and as such are frequently modelled as white noise processes [1].

$$S_{thermal} = \frac{4k_BT}{R_L} \tag{2.3}$$

In practical systems employing incoherent light, thermal and shot noise levels are typically much lower than source intensity noise [14], and as such, do not significantly affect the detected signal quality. The total noise at the detector output can be expressed as the summation of the independent contributions of source, shot and thermal noise:

$$S_{tot} = S_{source} + S_{shot} + S_{thermal} \tag{2.4}$$

The relationship between the different noise contributions for a typical optical receiver is further discussed in Section 2.4.

In addition to the PSD, noise can also be characterised in terms of relative intensity noise (RIN), a figure of merit that directly quantifies the level of intensity noise of a CW optical signal [15]:

$$RIN = \frac{\langle \Delta P_o^2 \rangle}{(P_{o,avg})^2} \qquad (Hz^{-1}) \tag{2.5}$$

Here, $\langle \Delta P_o^2 \rangle$ is the mean square intensity fluctuation spectral density (in W^2/Hz) of an optical signal and $P_{o,avg}$ is the average optical power (in W). Note that $\langle \Delta P_o^2 \rangle$ is measured at a specific electrical frequency. Since optical power is proportional to electrical current in the receiver, Equation (2.5) can also be expressed in terms of electrical noise power, P_e, as given by Equation (2.6).

$$RIN = \frac{(\Delta P_e)}{(P_{e,avg})} \qquad (Hz^{-1}) \tag{2.6}$$

Therefore, by taking the ratio of the measured electrical noise PSD, ΔP_e, to the average electrical power, $P_{e,avg}$, one obtains the RIN of the optical signal. The total RIN (RIN_T) is then given by Equation (2.7), where f represents the frequency of interest:

$$RIN_T = \int_{-\infty}^{\infty} RIN(f)df \tag{2.7}$$

In a general sense, RIN can be thought of as a form of inverse signal-to-noise ratio (SNR), and is a good figure of merit for assessing signal quality. While the noise spectral density gives the total noise of the system at the frequency of interest, RIN is a measure of system performance and thus relates directly to the achievable bit error rate (BER).

All noise measurements presented in this thesis were performed using one of two methods (the specific technique will be identified where noise measurements are presented), depending on the desired electrical bandwidth. Most noise measurements were performed using a low noise (noise equivalent power of 2.5 pW/$\sqrt{Hz}$) New Focus model 1811 photoreceiver which consisted of an InGaAs PIN photodiode followed by a transimpedance amplifier. The receiver 3 dB bandwidth was 125 MHz and its optical power to current conversion factor was approximately 600 A/W at 1550 nm. The output of the detector was connected to a Marconi (model 2382) RF spectrum analyser, which was used to measure the electrical noise PSD at the desired frequency of 100 MHz. For the RIN measurements, a digital oscilloscope was used to measure the average voltage, V_{avg}, at the output of the photodetector, and the average power of the electrical signal was calculated using $P = V_{avg}^2/R_L$. The uncertainty of the measurement was estimated based on the rated accuracy of the spectrum analyser and the oscilloscope [16], and was calculated to be ± 1 dB. Alternatively, an Agilent lightwave analyser with a bandwidth of 22 GHz was used to measure the RIN spectrum when a wider electrical bandwidth was required.

2.3 Numerical Model

In order to better understand the influence of different system parameters on the source noise, a numerical model was developed to predict the intensity noise properties of narrowband incoherent light. The model is based on the mathematical analysis presented by H.S. Kim et al. in reference [14]. In this analysis, the intensity fluctuations of a polarised thermal light source are related to the statistical properties of the optical field by using the relationship $cov_I(\tau) = |\Gamma_E(\tau)|^2$ where $cov_I(\tau)$ is the covariance of the intensity and $\Gamma_E(\tau)$ is the self-coherence function of the input optical field. Using this relationship, together with the well known Wiener-Khinchin theorem [11], an analytical expression for the source noise PSD, $S_{source}(f)$, is derived in terms of the spectral density of the narrowband optical signal:

$$S_{source}(f) = \alpha^2 I_o^2 R_L \int_{-\infty}^{\infty} \psi(x + \frac{f}{2})\psi(x - \frac{f}{2})dx \tag{2.8}$$

Here, α is the optical power to current conversion factor, I_o is the intensity of the optical source, and R_L is the load resistance of the photodetector. $\psi(\nu)$ is the spectral envelope function of the optical PSD, normalised to unit power and shifted to a centre frequency of zero. Conceptually, this formula indicates that the noise at a specific frequency f is the superposition of the products of all pairs of spectral components with difference frequency f. Equation (2.8) can therefore be used to numerically evaluate the intensity noise at the output of the photodetector for an arbitrarily shaped input optical spectrum. Further details of the numerical calculations are given in Appendix A. Note that the input optical PSD to the model can be an analytical function or experimentally measured spectral data.

The accuracy of the numerical model was experimentally verified using the setup shown in Figure 2.1. All experiments performed throughout this investigation used ASE from an EDFA as the source of incoherent light[3], as these fibre sources were readily available in our laboratory. The required narrowband input is formed by shaping this broadband spectrum using passive optical filters, such as FBGs. The filter shapes used in this experiment are shown in Figure 2.3. RIN measurements

[3]Previous studies have shown that ASE from an EDFA is thermal-like in nature [14, 17].

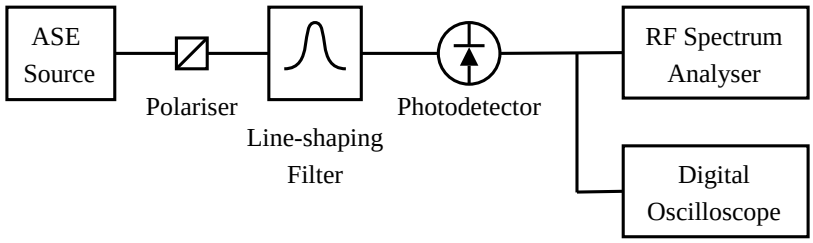

Figure 2.1: Experimental setup for verifying thermal light noise model accuracy.

were performed at 100 MHz using a low noise photodetector and spectrum analyser (as outlined in Section 2.2), and are given in Figure 2.2, together with predicted RIN values. Note that in this case the experimentally measured filter functions were used as input to the model. It is clear from Figure 2.2 that the theoretical predictions are in excellent agreement with measurements. Having thus demonstrated the accuracy of the numerical model, we can use it with confidence to predict the RIN associated with polarised thermal light of arbitrary spectral shape.

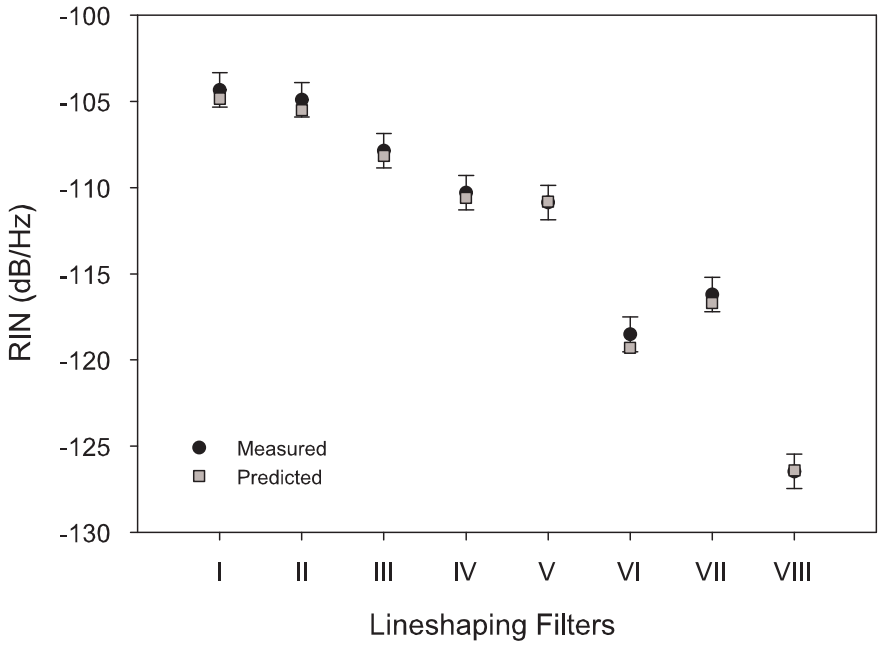

Figure 2.2: Experimental and predicted RIN for different lineshaping filters; the corresponding input spectra are shown in Figure 2.3.

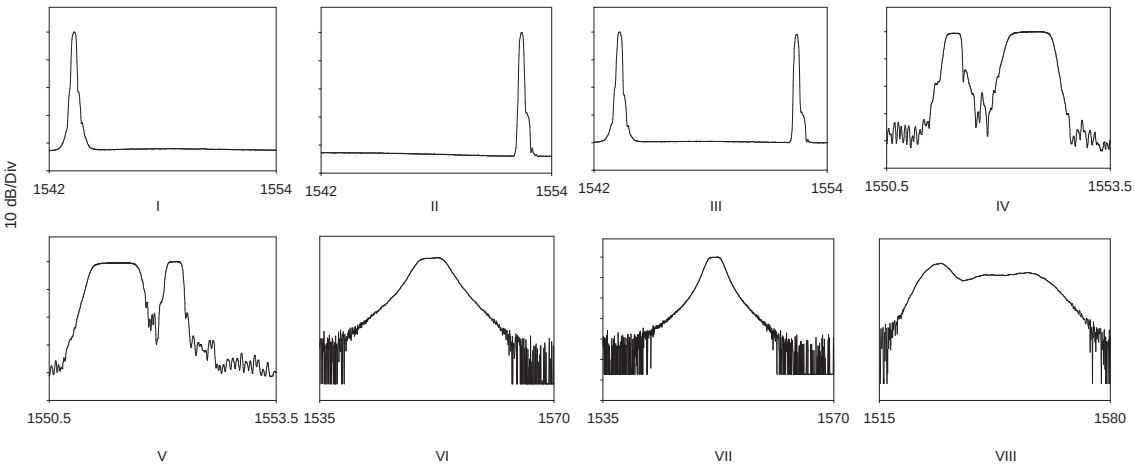

Figure 2.3: Thermal light spectra for the different lineshaping filters depicted in Figure 2.2. The horizontal axis is the wavelength in nm and the vertical axis is the normalised power spectrum. Number viii is the unfiltered ASE spectrum.

The next section explores the properties of intensity noise in further detail. In particular, I look at RIN as a function of source intensity, bandwidth, spectral shape, electrical frequency and dispersion.

2.4 Properties of Intensity Noise

The experimental setup used for the characterisations to follow is shown in Figure 2.4. As before, ASE from an EDFA was used as the incoherent broadband light source while the 5 nm bandpass filter[4] and inline EDFA are used to increase the optical spectral density in the bandwidths of interest. In each case, the predicted noise PSD is estimated using the numerical model, as outlined in the previous section.

2.4.1 Noise as a Function of Optical Intensity

To investigate the effects of source power on intensity noise, a variable optical attenuator was used to control the input power to the photoreceiver. The noise was measured at an electrical frequency of 100 MHz, while the lineshaping filter used for this particular characterisation was of bandwidth 0.48 nm (59 GHz). Experimental

[4]Unless stated otherwise, all filters are specified in terms of their 3 dB bandwidth.

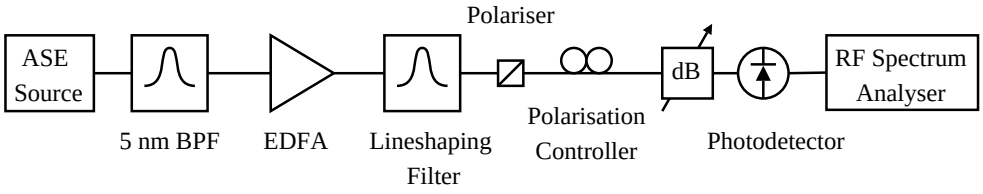

Figure 2.4: Basic experimental setup for intensity noise characterisations presented in Section 2.4.

and predicted results for the noise PSD are shown in Figure 2.5, together with shot noise and the detector thermal noise floor. The shot noise, S_{shot}, was calculated using Equation (2.2) with a load resistance of 50 Ω. The detector floor was experimentally measured and is the noise power at the detector output with no optical input present.

As expected, the predicted total noise is in excellent agreement with experimental measurements. The source noise predictions also closely follow measurements at higher power levels where source intensity noise dominates. The predicted source noise is a line with a slope of ∼2 (on a log-log scale), and corresponds to the quadratic relationship between the optical intensity and the noise PSD as given in Equation (2.8). At lower powers, measurements follow the detector noise level, since in this regime the system is clearly detector noise limited. Note that for the power levels considered in this characterisation, the shot noise contribution was insignificant.

The corresponding RIN as a function of optical intensity is given in Figure 2.6. As expected from Equation (2.6), the predicted RIN is invariant with received optical intensity. However, at lower power levels the experimental RIN values deviate significantly from calculations. This discrepancy is a result of the detector noise limit, in which regime, a decrease in optical power does not correspond to a measurable decrease in total noise. On the other hand, as the optical power increases, the source noise increases accordingly. Once the source noise exceeds the detector noise floor, any further increase in optical intensity yields a proportional increase in the measured intensity noise level, allowing the RIN to remain constant. This is visible in Figure 2.6, where we can see that at power levels ≥-20 dBm, the measured RIN approaches the predicted value of approximately -110 dB/Hz. In the rest of the thesis, all presented RIN measurements were performed at an optical power of -14 dBm,

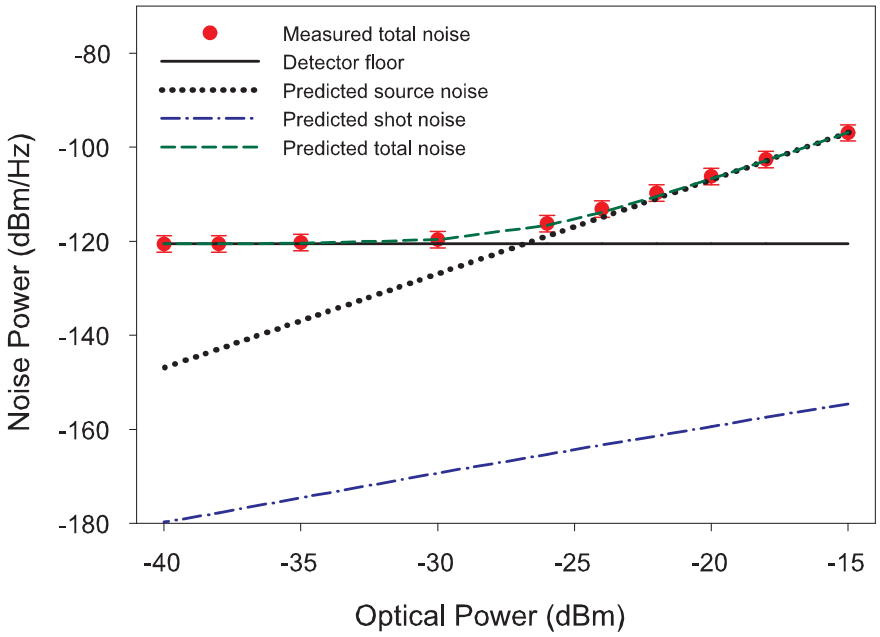

Figure 2.5: Spectral noise PSD as a function of detector input power. Measurements are performed at 100 MHz.

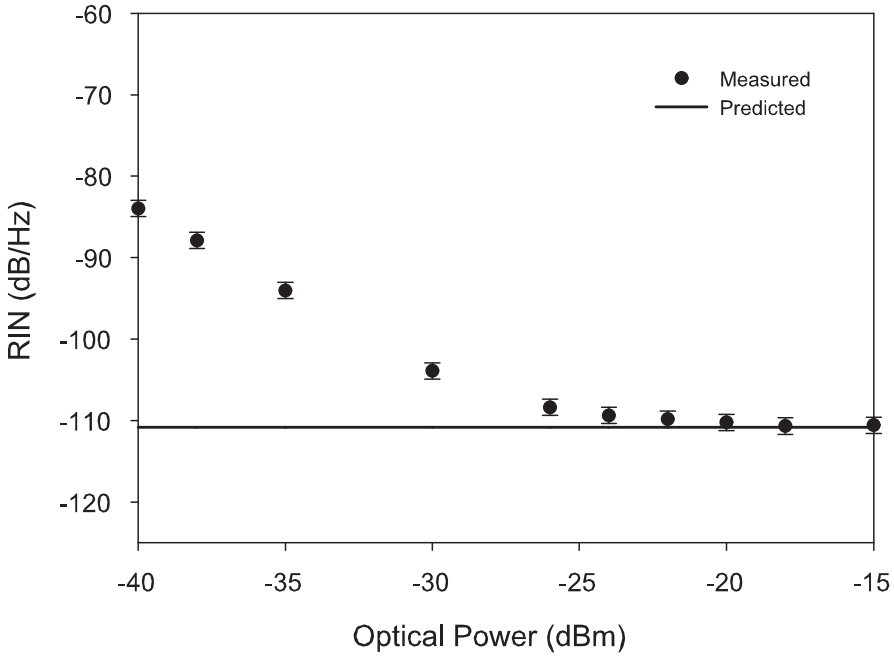

Figure 2.6: RIN as a function of detector input power.

where source noise far exceeds the detector noise floor. It is clear from the above results that the RIN, and therefore SNR of narrowband incoherent light cannot be improved by increasing the received signal power.

2.4.2 Noise as a Function of Source Bandwidth

To quantify the noise as a function of source bandwidth, RIN measurements were repeated for eight different lineshaping filters of widths 0.05, 0.24, 0.5, 0.8, 1.0, 1.3, 1.5, and 2.0 nm. Corresponding RIN values were also calculated for each filter function, and are shown in Figure 2.7 along with experimental data. All filters used in this experiment were similarly shaped, FBGs with steep roll-off, as depicted in the inset.

We see that the RIN decreases (i.e. SNR increases) with increasing bandwidth. As the lineshaping filter width varied from 0.05 to 2.0 nm, the RIN decreased by greater than 12 dB, a factor of 16 in linear units.

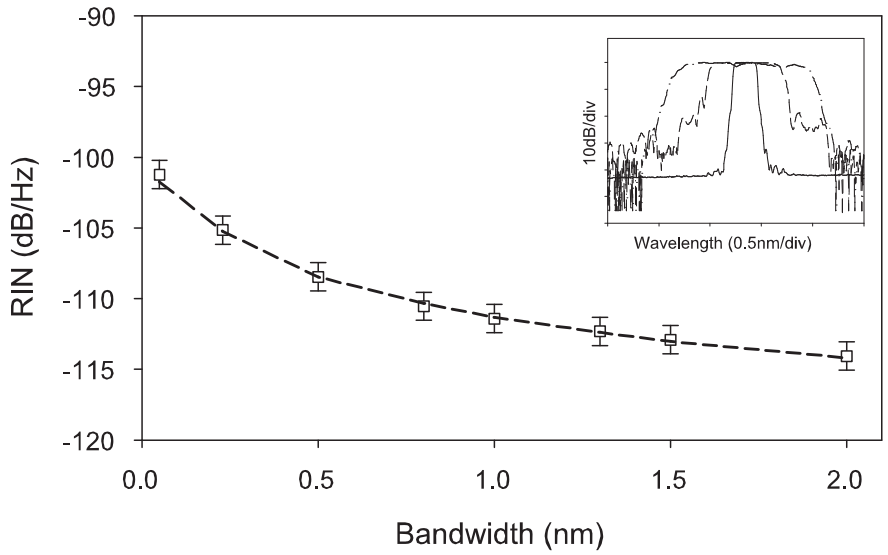

Figure 2.7: Experimental (□) and simulation (– – –) results of RIN as a function of the source bandwidth. A few representative spectra of selected lineshaping filters are shown in the inset.

In order to assess the noise and source bandwidth relationship over a much larger range of filter widths than available in the laboratory, I used the numerical model to calculate the RIN for analytically generated Gaussian slices of varying width. The results, which are given in Figure 2.8, display the same trend as that of Figure 2.7 and show that the RIN is inversely proportional to the source bandwidth [14]. It

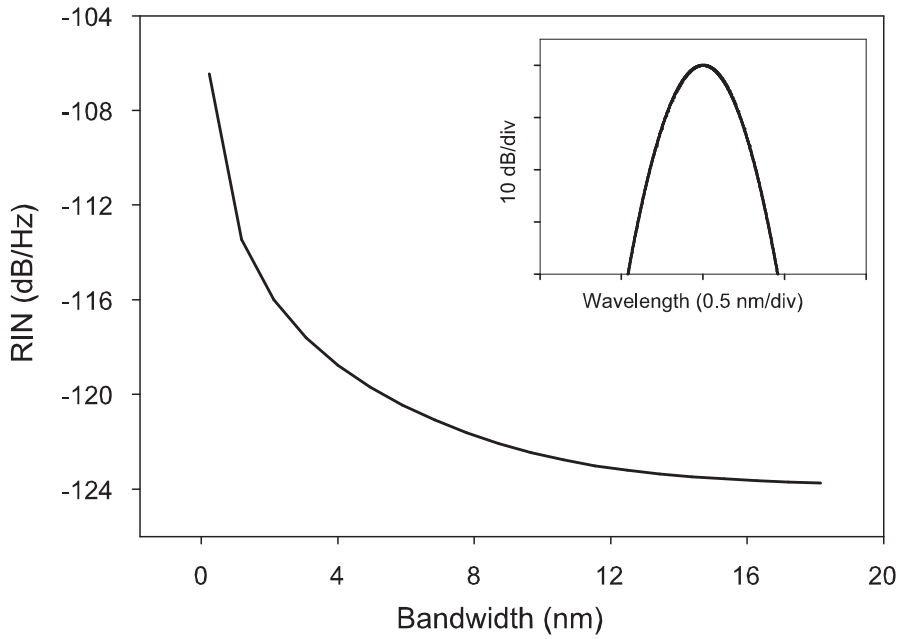

Figure 2.8: RIN as a function of source bandwidth for an analytically generated Gaussian spectral-slice (inset shows representative filter shape).

is clear from these results that significantly better signal quality can be achieved by increasing the source bandwidth.

2.4.3 Noise as a Function of Source Spectral Shape

It is clear from Equation (2.8) that the shape of the source spectrum, $\psi(\nu)$, should also affect signal noise. Thus, it should be appreciated that while Figures 2.7 and 2.8 discussed above show the same trend, the actual RIN values cannot be directly compared, because of the noticeable difference in filter shapes. I examined this further using three analytically generated spectral shapes (sinc, Gaussian, and super Gaussian[5] of order 10; illustrated in Figure 2.9) with identical 3 dB bandwidths. The calculated RIN values for the three spectra are given in Table 2.1. As can be seen from these results, the varying spectral shapes give rise to different levels of RIN, despite identical 3 dB filter bandwidths.

This was also confirmed experimentally using two filters of approximately the

[5]Recall that a super Gaussian function, $g(x)$, is given by, $\frac{1}{\sqrt{2\pi\sigma^2}} exp(\frac{-(x-\mu)^{2n}}{2\sigma^2})$, where n is the order of the function. When $n = 1$, $g(x)$ is known as Gaussian.

same 3 dB bandwidth (0.24 nm); filter functions are given in Figure 2.10. A RIN value of -105.2 dB/Hz was obtained with the steep roll-off filter (a), while a noticeably improved RIN value of -109.1 dB/Hz was recorded for the more bell-shaped filter (b).

These results indicate that for the same 3 dB bandwidth, filters with steeper roll-off show a distinctly higher noise level than their counterparts with wider 20 dB bandwidths. It is clear therefore that the source spectral shape plays an important role in the noise properties of narrowband thermal light.

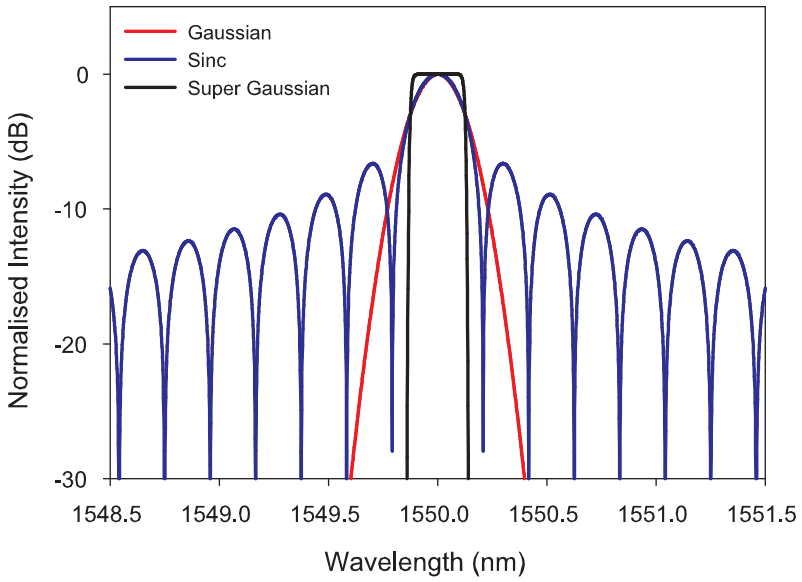

Figure 2.9: Filter functions used for RIN vs spectral shape calculations shown in Table 2.1.

Table 2.1: RIN as a function of spectral shape

Shape	RIN (dB/Hz)
Super Gaussian	-108.1
Gaussian	-109.8
Sinc	-111.9

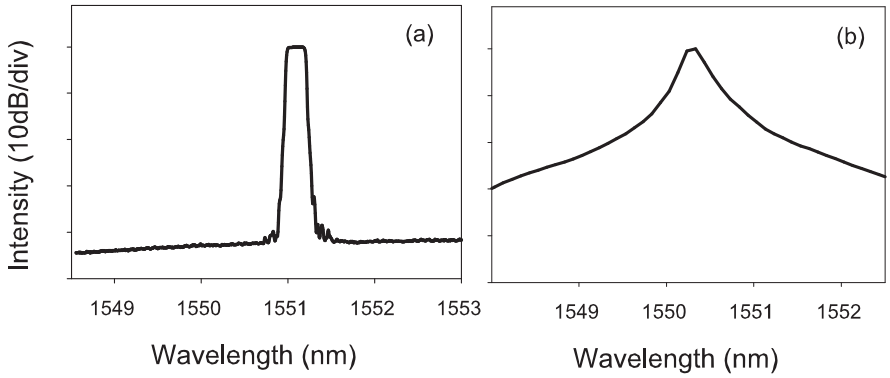

Figure 2.10: Two filter shapes of approximately 0.24 nm bandwidth, used to quantify RIN as a function of spectral shape.

2.4.4 Noise as a Function of Electrical Frequency

As discussed previously in Section 2.3, the source noise, $S_{source}(f)$, given by Equation (2.8), is the summation of all beat components with difference frequency f. As long as f is much smaller than the source bandwidth, $\Delta\nu$, the source RIN can be approximated to be invariant with measurement frequency (i.e. the white noise approximation is valid). However as the frequency of interest approaches the optical bandwidth, it is clear from Equation (2.8) that the number of beat components with difference frequency f will decrease accordingly, thus reducing the RIN. This is clear from Figure 2.11(a), where I have shown RIN calculations for a 0.24 nm ($\sim$30 GHz) source bandwidth over a 30 GHz frequency range; a noticeable 'roll-off' in the RIN occurs after $\sim$5 GHz.

Experimentally, the white noise approximation holds as long as the source bandwidth $\Delta\nu$ is much larger than the detector bandwidth. This was also verified by measuring the RIN spectrum of a 30 GHz source slice over a 22 GHz bandwidth. Once again, the RIN is approximately constant over a 5 GHz spectral range, after which point a slight roll-off is observed.

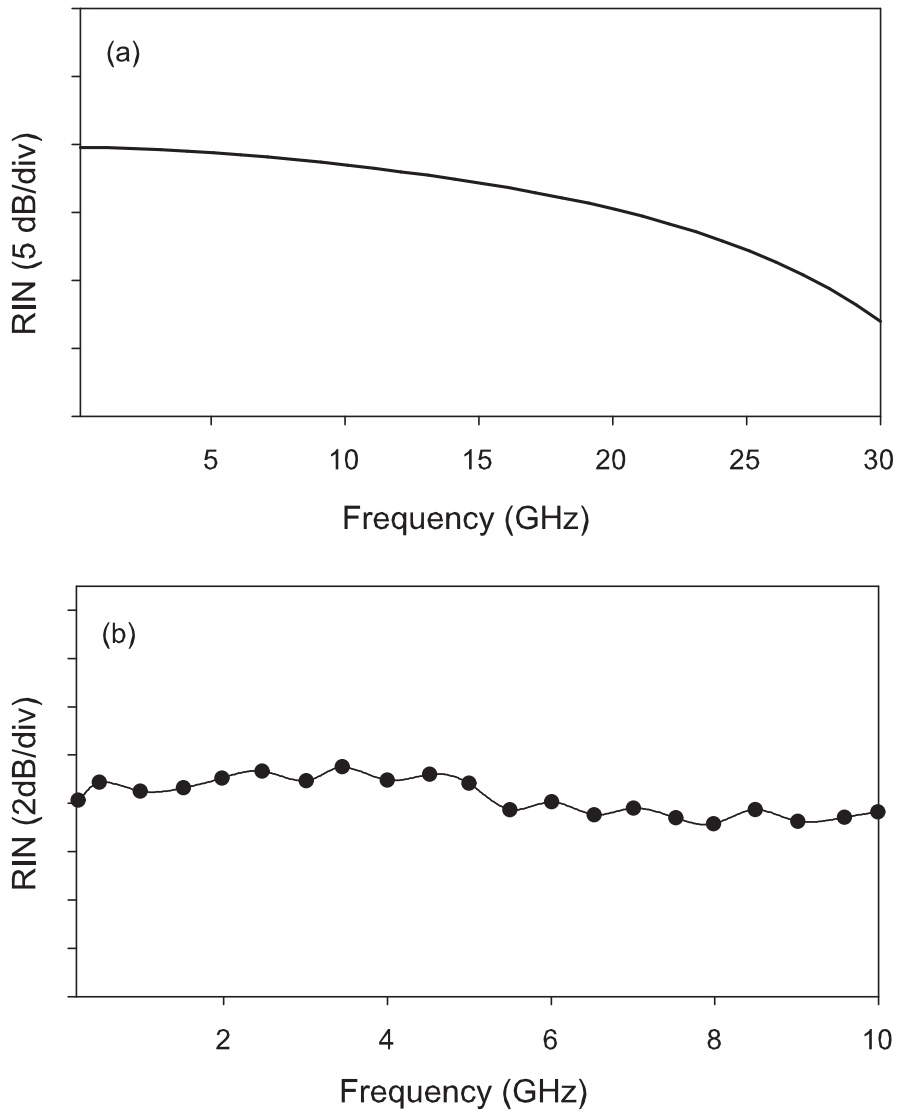

Figure 2.11: Calculated (a) and experimental (b) results of RIN spectra for a 0.24 nm (30 GHz) source bandwidth. Measurements are performed using a 22 GHz bandwidth Agilent lightwave analyser.

2.4.5 Noise as a Function of Chromatic Dispersion

As discussed in Section 2.1, due to the statistically independent nature of individual phase components, a relative phase delay between different spectral components does not alter the statistical properties of the thermal light field. I confirmed this experimentally by subjecting the light to chromatic dispersion.

This is accomplished by launching narrowband thermal light (of 0.24 nm spectral bandwidth) into varying lengths of single mode fibre (SMF) of known dispersion, and then monitoring the output RIN. The measured RIN at 100 MHz is shown in Figure 2.12 and, as expected, is indeed invariant with added dispersion. In contrast, introducing a saturated SOA to suppress the intensity fluctuations of thermal light, gives rise to light of a very different statistical nature, the noise properties of which are in fact altered by chromatic dispersion. This will be discussed in much greater detail in Chapter 3.

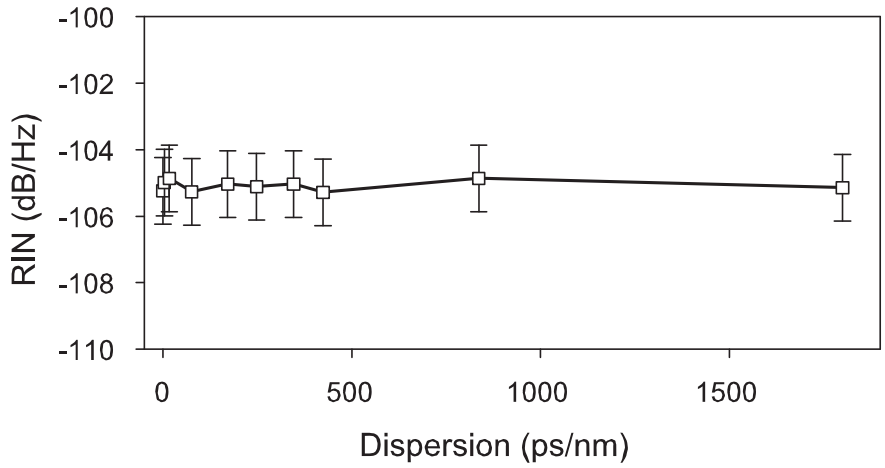

Figure 2.12: Measured RIN as a function of chromatic dispersion.

2.5 Summary and Discussion

In this chapter I have experimentally and theoretically examined the properties of intensity noise in narrowband thermal light. I have confirmed that the excess photon noise is proportional to the optical intensity, and consequently, that the SNR cannot be improved by increasing the signal power. The noise is also shown to be inversely proportional to the source bandwidth and strongly dependent on the shape of the spectral profile. The white noise approximation for thermal light was confirmed to be valid over a wide electrical bandwidth. Finally, the measured noise was seen to be unaffected by the presence of chromatic dispersion, as expected, due to the random relative phase relationship of incoherent light.

In Chapter 3 I will be looking at reducing the intensity noise of incoherent light using a saturated SOA. It is to be appreciated that both the numerical and experimental investigations presented herein, were crucial to the understanding and study of intensity noise reduction. Having clearly confirmed the thermal-like nature of the fiberised ASE source used in these experiments, any non-thermal properties of intensity smoothed light may safely be attributed to changes introduced by the noise suppression process. The characterisations presented here form a solid basis for comparison with noise suppressed light, to be examined in detail in the following chapter.

Chapter 3

Intensity Noise Suppression Using a Saturated SOA

Overview: In this chapter I investigate the use of a gain-saturated SOA for intensity noise reduction of incoherent light, using experimental measurements and numerical analysis to characterise the nonlinear noise suppression process. These characterisations are used to determine an optimum operating point of the SOA which would maximise the achievable suppression benefit. I have given particular emphasis to understanding the properties of the intensity smoothed SOA output light, which is shown to be distinctly non-thermal in nature. I also demonstrate that the improvement in signal quality is accompanied by spectral distortion, which renders it susceptible to deterioration in the presence of subsequent optical filtering. However, these adverse affects can be alleviated by amplifier and system design optimisations, yielding significant improvements in signal quality.

3.1 Introduction

Though an economical alternative to laser technology, incoherent sources such as LEDs or fibre based ASE sources are limited in performance due to their excess photon noise, thus becoming a critical design issue for applications employing such sources. It is therefore of great interest to explore techniques to reduce this intensity noise and improve the received signal quality. To date, a number of noise suppression

schemes have been proposed.

One optoelectronic technique uses two balanced photodetectors and a unity gain differential amplifier (with AC and DC coupled ports) to subtract out the intensity fluctuations from the received signal [18]. Although this approach gives an improvement in signal quality, the noise reduction is limited by the bandwidth of the electronic circuit; in the experiment reported here, the suppression bandwidth was limited to ∼1 MHz. This particular noise mitigation method was investigated for sensor applications as a means of reducing source noise in fibre optic gyroscopes.

Many of the proposed intensity noise mitigation schemes have been investigated in the context of spectrum-sliced WDM applications, and will be discussed in greater detail in Chapter 4. A different optoelectronic approach to the one above, uses a feed-forward technique to subtract out the noise from the forward propagating light [19]. However, precise phase and gain matching of the relevant circuitry limits the use of this technique in high speed applications. An all-optical technique was also proposed which uses fibre nonlinearities to significantly increase the bandwidth of the received light, resulting in improved signal quality [20].

One particular all-optical approach that has aroused interest in the research community is the use of the nonlinear signal processing properties of a gain-saturated SOA [21, 22]. The simplicity and effectiveness of this technique has attracted attention as a potentially low-cost, low-complexity solution for metropolitan and access markets, and this chapter presents a detailed examination of the properties, merits and drawbacks of this approach, as a means to reduce the excess intensity noise of narrowband incoherent light.

3.2 Theoretical Background

The noise suppression offered by the SOA is primarily the result of small signal gain compression arising from the nonlinearity of the saturated amplifier. An analytical study of these effects presented by Zhao et al. [23], gives useful insight into the noise suppression mechanism, and is therefore briefly reviewed here as an introduction to the technique.

Consider a time-varying optical signal incident into a travelling-wave SOA. Ignoring added ASE from the amplifier, the power, P, and carrier density, N, can be described by the standard semiconductor laser rate equations (for example, see [24, 25]) as follows:

$$\frac{\partial P}{\partial z} + \frac{1}{v_g}\frac{\partial P}{\partial t} = \Gamma g(N)P - \alpha_{int}P \tag{3.1}$$

$$\frac{\partial N}{\partial t} = \frac{I}{qV} - \frac{N}{\tau_s} - \frac{\Gamma}{h\nu A}g(N)P \tag{3.2}$$

Here, v_g is the group velocity, Γ the mode confinement, $g(N)$ the gain coefficient, α_{int} the internal loss, I the injected current, q the electronic charge, h Planck's constant, V the active layer volume of the device, A the area of the active region, τ_s the spontaneous carrier lifetime and ν the input centre frequency.

The power and carrier density through the device can each be expressed as the sum of a CW component and the Fourier decomposition of the time-varying noise fluctuations (i.e. $P = P_0 + \frac{1}{2\pi}\int \Delta P(\Omega)e^{j\Omega t}d\Omega$ and $N = N_0 + \frac{1}{2\pi}\int \Delta N(\Omega)e^{j\Omega t}d\Omega$, where P_0 and N_0 are the time averaged values of the power and carrier density respectively). By making this substitution into the rate equations, and linearising the amplifier gain[1] ($g(N) = a(N - N_o)$, where a is the differential gain coefficient), small signal equations for the power and carrier density can be derived:

$$\frac{\partial \Delta P}{\partial z} = j\frac{\Omega}{v_g}\Delta P + \left[\Gamma g(N) - \alpha_{int}\right]\Delta P + \Gamma a \Delta N P_0(z) \tag{3.3}$$

$$\Delta N = -\frac{\Gamma g(N_0)\Delta P}{h\nu A}\frac{1}{j\Omega + \frac{1}{\tau_s} + \frac{\Gamma a P_0}{h\nu A}} \tag{3.4}$$

Here, ΔP and ΔN are the noise power and carrier density fluctuation at a *single electrical frequency* Ω. Equation (3.3) represents the rate of change of intensity noise (at frequency Ω) with propagation distance through the device, while Equation (3.4), describes the carrier density perturbations that occur in response to the noise of the

[1]Linearising the gain is a valid approximation in the case of small signal modulation [26].

incoming optical signal. The negative sign in Equation (3.4) indicates the inverse relationship between the carrier density and input optical power, where an increase (decrease) in power gives rise to a depletion (increase) in carrier density. It can be seen in Equation (3.3) that the time averaged component of the power, P_0, occurs only once, in the last term of the expression. When P_0 is small, this term has little effect and any incoming light, including any signal noise/modulation, is linearly amplified through the device. However, as P_0 increases, the negative contribution of the last term results in a noticeable reduction or compression of the noise component. Therefore when the input power is sufficiently large (i.e. when the amplifier is saturated), the output noise will be substantially reduced, resulting in intensity smoothing of the amplifier input. This is depicted graphically in Figure 3.1.

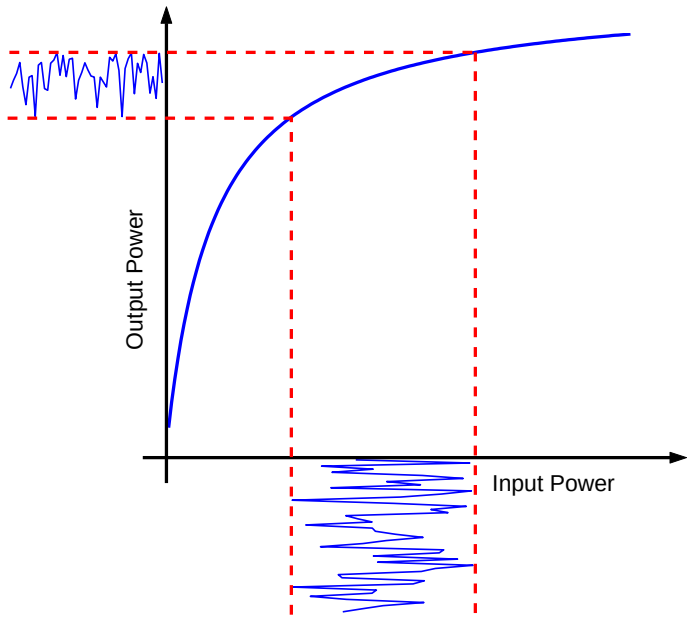

Figure 3.1: Conceptual illustration of the small signal gain compression in a saturated SOA.

Note from Equation (3.4) that the carrier density perturbation, ΔN, follows a low-pass response to the intensity noise of the input light. The 3 dB frequency of this low frequency noise suppression, $\frac{1}{\tau_{eff}}$, is given by,

$$\frac{1}{\tau_{eff}} = \frac{1}{\tau_s} + \frac{\Gamma a P_0}{h\nu A}. \tag{3.5}$$

This low-pass filtering gives rise to a high-pass response of the output noise power to input intensity fluctuations. Therefore in contrast to thermal light, the noise PSD

of an intensity smoothed signal will display a dip at DC, with a gradual rise in noise power with increasing frequency [23]. A more extensive analysis of the intensity noise suppression process can be found in [27], where the authors derive analytical expressions for the noise PSD of a *noisy coherent* signal amplified by a saturated SOA.

Assuming a homogeneously broadened amplifier that becomes equally saturated across the entire gain bandwidth [28], gain compression is not restricted to the high intensity components of the input light, but occurs across the entire signal spectrum. Thus gain saturation is accompanied by other nonlinear effects of cross-gain modulation, phase modulation and four wave mixing (FWM), which are interrelated via the carrier density [1, 26]. Their impact on the noise suppression process is examined later in this chapter.

3.3 Properties of SOA-Based Noise Reduction

3.3.1 SOA Operating Point

It is expected from the preceding analysis that the achievable noise suppression and associated bandwidth will depend heavily on operating parameters such as input intensity and drive current, and also on SOA device parameters. Experimental characterisations are presented in this section which illustrate this point and were used to determine an optimum SOA operating point for use in future communication system experiments. These characterisations were based on the following experimental setup and procedure.

A polarised ASE source was spectrally filtered using a 0.24 nm (30 GHz) FBG (see Figure 3.2). An EDFA was inserted after the FBG in order to ensure sufficient input power to saturate the SOA. The input power and polarisation to the amplifier were then optimised using a variable attenuator and polarisation controller respectively. Single frequency RIN measurements were performed at 100 MHz, using a 125 MHz photodetector and an electrical spectrum analyser, while as before, RIN spectra were measured using the 22 GHz bandwidth lightwave analyser.

Let us first consider the noise PSD before and after noise suppression for two

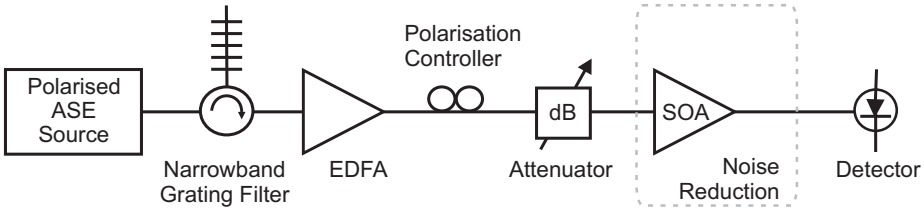

Figure 3.2: Block diagram of experimental setup for SOA operating point and suppression bandwidth characterisations.

different SOAs, over a 125 kHz to 10 GHz range (Figure 3.3). The amplifiers are conventional bulk devices from Alcatel (model 1901) and JDS Uniphase (model CQF874) respectively[2]. Although the SOAs are operated at approximately the same level of gain, the Alcatel SOA gives ∼7 dB greater suppression at low frequencies. This measurement qualitatively illustrates the dependence of the noise suppression process on the SOA device parameters, which is an important consideration when choosing an appropriate amplifier. Furthermore, as expected from the previous analysis, we observe a roll-off in the noise PSD towards DC for the SOA output spectrum. This is in contrast to thermal-like light, where the RIN is essentially flat across a wide frequency range.

I focus now on the noise suppression offered by a single SOA; unless otherwise specified, results presented are for the Alcatel SOA. To quantify output signal quality as a function of amplifier operating point, RIN measurements were performed as a function of the SOA input power and drive current. Note that for each measurement, the polarisation at the input to the SOA was optimised to obtain the lowest noise floor. A difference in noise of approximately 1.5 dB was observed between the best and worst polarisation alignment into the amplifier. We see from Figure 3.4 that the RIN suppression does not improve appreciably for drive currents and input power levels greater than 150 mA and +5 dBm respectively. However, high input power reduces the amplification benefit of the SOA, a desirable feature in communication applications. The majority of experiments presented in the rest of the thesis were performed at an amplifier drive current of 200 mA, and an input power of +5 dBm.

[2]SOA specifications are given in Appendix D.

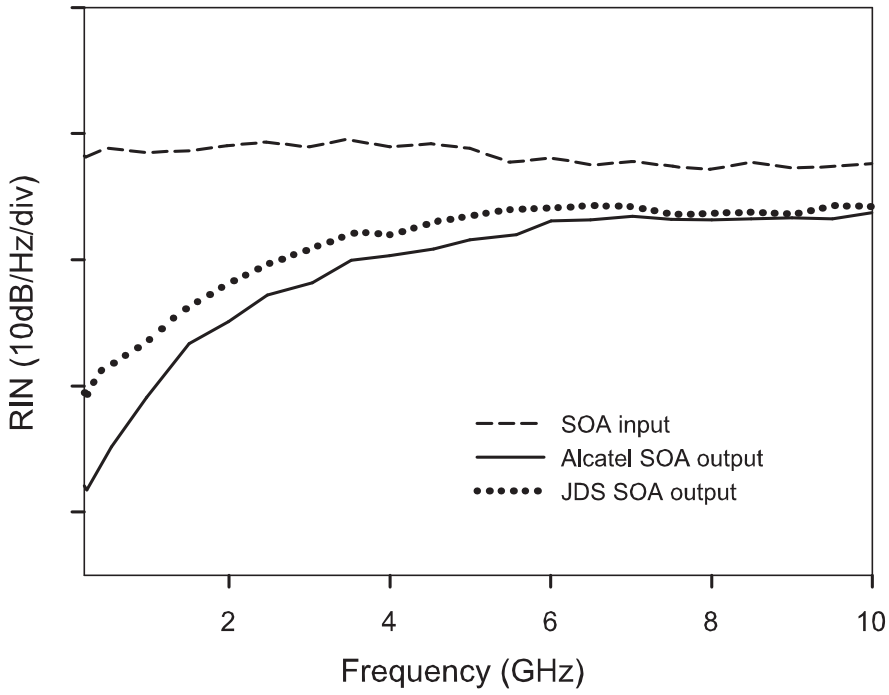

Figure 3.3: RIN spectra for two different commercial SOAs operated at similar gain levels. Input slice bandwidth is 0.24 nm.

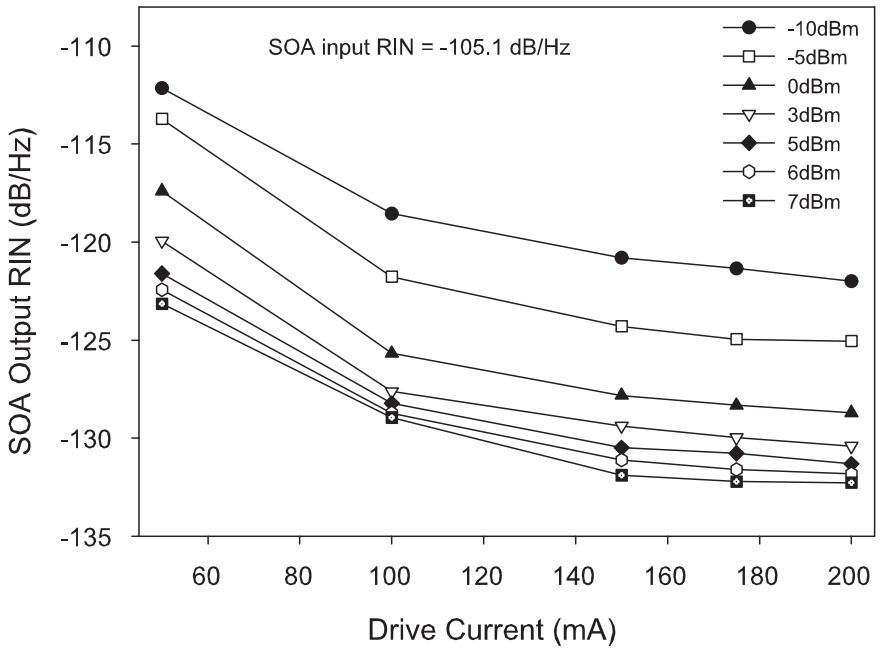

Figure 3.4: SOA output RIN as a function of the amplifier drive current and input power. SOA input RIN for the 0.24 nm spectrum-slice is -105.1 dB/Hz.

3.3.2 Suppression Bandwidth

The achievable suppression bandwidth directly determines the maximum usable channel bit-rate for communications applications and is therefore a critical parameter in any noise compensation technique. I next investigated the dependency of the noise suppression bandwidth on device operating point by measuring the SOA output RIN spectrum as a function of input power and drive current. In the first instance, I varied the SOA drive current while the input power was held constant at +5 dBm. In the second characterisation, I varied the SOA input power while the drive current was fixed at 200 mA. The 3 dB suppression bandwidth was then determined for each measurement and is shown in Figure 3.5. For the purposes of these characterisations, the noise suppression bandwidth is defined as the frequency at the half-power point from the maximum value of the noise spectrum curve within a 20 GHz bandwidth. In Figure 3.5(a) we see that as the drive current was varied from 50 mA to 200 mA, the bandwidth improved from ∼1 GHz to ∼4 GHz. At fixed drive current (Figure 3.5(b)) the bandwidth increased from ∼2.6 GHz to ∼4.2 GHz as the input power was varied from -10 dBm to +7 dBm. It is clear from these results that the SOA offers appreciable suppression bandwidth even at relatively low saturation levels.

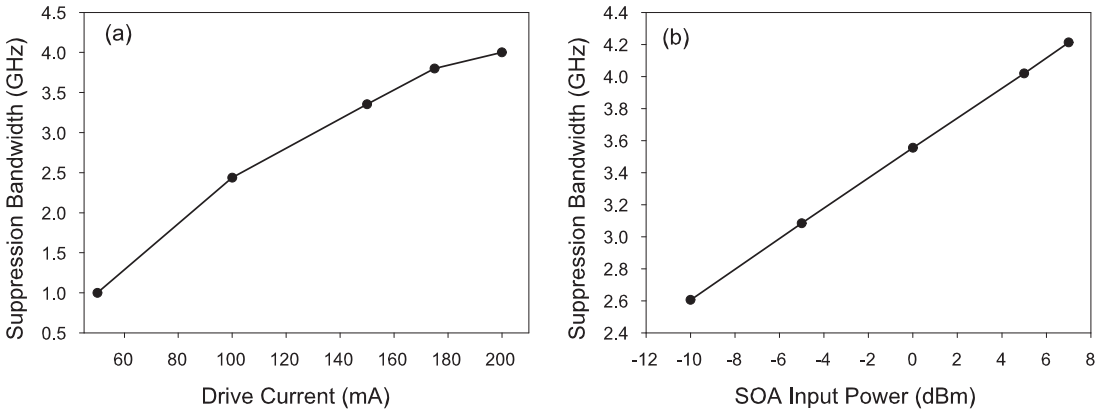

Figure 3.5: Noise suppression bandwidth as a function of (a) the drive current while the input power is fixed at +5 dBm and (b) the input power while the drive current is fixed at 200 mA.

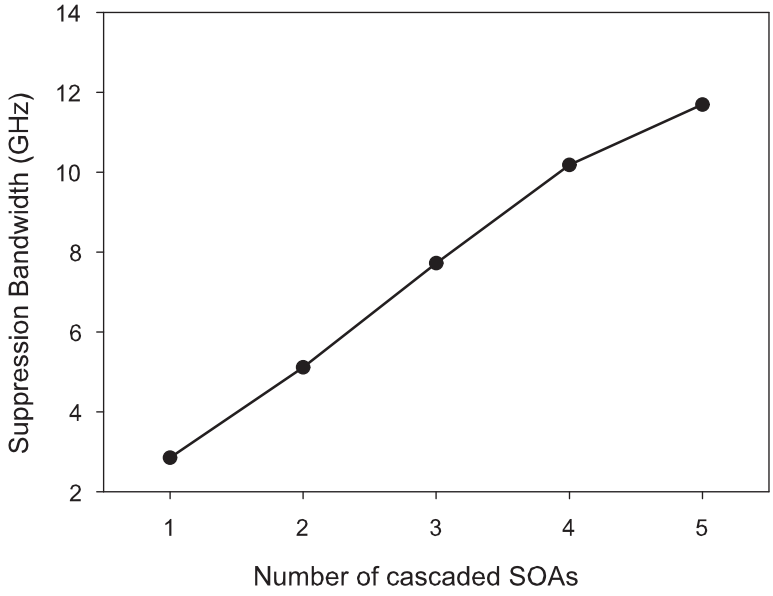

Figure 3.6: Noise suppression bandwidth as a function of the number of cascaded SOAs.

3.3.3 Multistage SOAs for Added Noise Suppression

The noise suppression bandwidth can also be improved by cascading SOAs in series as discussed in [22], and I examined the effectiveness of this approach using a five-stage SOA arrangement. All five JDS amplifiers used in this experiment were operated at the same gain compression level (+5 dBm input power, 450 mA drive current) and the SOA output RIN spectrum was measured for each additional amplifier stage. The increase in required drive current (in comparison with the 200 mA drive current of the Alcatel SOA) is due to the difference in amplifier design. Figure 3.6 shows the suppression bandwidth as a function of the number of SOAs. With a five-stage SOA cascade I was able to achieve a suppression bandwidth of 12 GHz, a factor of four improvement over the single stage JDS SOA bandwidth of $\sim$3 GHz. These results are not directly comparable with a single-stage SOA with the same total device length, due to the additional attenuators and polarisation controllers between each pair of amplifiers. The added ASE would also be reduced in the single amplifier arrangement. Although cascaded SOAs give considerable improvement in the suppression bandwidth, conventional single-stage SOAs still offer substantial noise mitigation for bandwidths relevant to metro and access applications.

3.3.4 Spectral Broadening and Distortion

From the experimental results presented thus far, it is clear that the SOA efficiently suppresses the intensity fluctuations over a bandwidth determined by the carrier lifetime, operating point and device parameters. However, in the course of my experimental investigations it became increasingly clear that the technique was not without caveats. In particular, it was observed that the saturated SOA caused pronounced spectral broadening for steep roll-off, narrow input spectral bandwidths. This is illustrated in Figure 3.7, which shows the SOA spectral response to two filters of approximately the same 3 dB bandwidth (∼0.24 nm) but with differing spectral shapes. It is clear that the steep bandwidth slice in Figure 3.7(a), which has higher intensity noise (see Section 2.4), incurs more prominent spectral distortion. Additionally, I found that spectral filtering of this broadened SOA output degraded the quality of the intensity smoothed signal [29]. These post-SOA filtering effects could significantly undermine the value of the technique, thus posing a challenge to its applicability in communication applications.

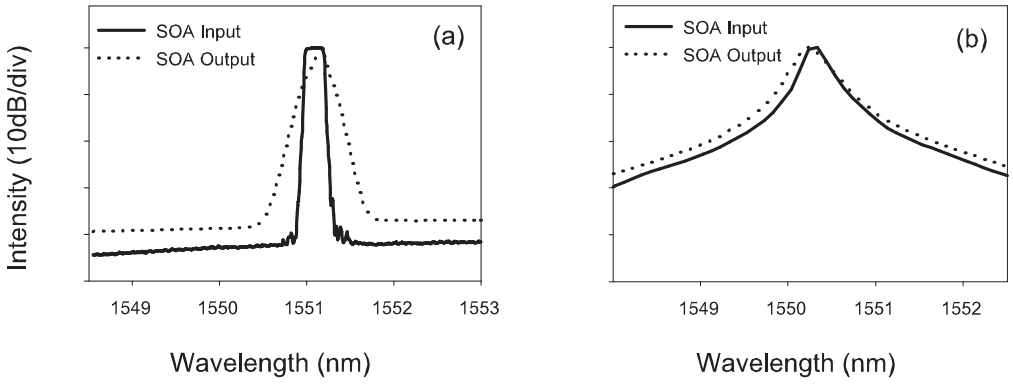

Figure 3.7: Spectral broadening of the SOA output for two different filter shapes, both with ∼0.24 nm bandwidths. More pronounced broadening and distortion is observed with the steep filter.

It became clear therefore, that a travelling-wave SOA model would be very valuable in order to gain a better understanding of the spectral properties of intensity-smoothed light. Although the noise reduction can be modelled by the intensity and carrier density rate equations alone, as discussed in Section 3.2, the field equation is required to predict the spectral properties of the SOA output light [30], including the

effects of post-SOA filtering.

It is appropriate therefore to take a slight detour from the main theme of the current section, (i.e. the properties of SOA-based noise reduction) in order to acquaint the reader with the main aspects of our numerical model. These simulations are used to support my experimental observations, and provide valuable insight into the entire noise suppression process.

3.3.5 Numerical Model of Travelling-Wave SOA

As introduced above, to better understand the spectral properties of the intensity-smoothed light, the system shown in Figure 3.8 was modelled using the field $E(z,t)$ and carrier density $N(z,t)$ equations [31]:

$$\frac{\partial E}{\partial z} + \frac{1}{\upsilon_g}\frac{\partial E}{\partial t} = \frac{\Gamma}{2}(1 - i\alpha)g(N)E - \frac{\alpha_{int}}{2}E \tag{3.6}$$

$$\frac{\partial N}{\partial t} = \frac{I}{qV} - \frac{N}{\tau_s} - \frac{\Gamma}{h\nu}g(N)\left|E\right|^2 \tag{3.7}$$

Here, υ_g is the group velocity, Γ the mode confinement, α the linewidth enhancement factor, $g(N)$ the gain ($g(N) = a(N - N_o)$, where a is the differential gain coefficient), α_{int} the internal loss, I the injected current, q the electronic charge, V the active layer volume of the device, τ_s the spontaneous carrier lifetime, h Planck's constant, and ν the input centre frequency.

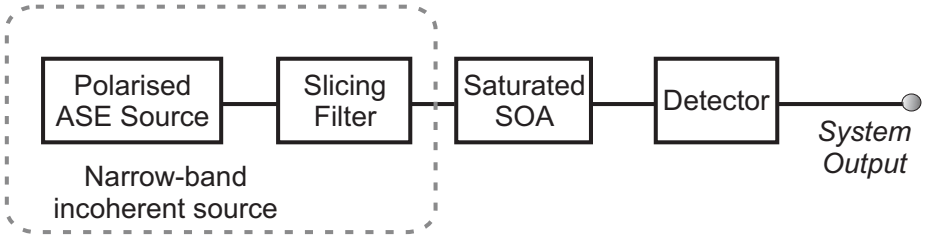

Figure 3.8: System modelled by numerical simulations.

The SOA output field is calculated by numerically propagating an input thermal light field through the travelling-wave SOA model. The amplifier is divided into short

segments where the length of each segment is small relative to the spatial variations of the input intensity. The field and carrier density equations are solved on this spatial grid using an ordinary differential equation solver which calculates the field at the device output, $E(t, z = L)$. The SOA output spectrum $E(\nu)$ is the Fourier transform of $E(t, z = L)$, and was obtained by averaging $E(\nu)$ over many samples of the input incoherent field. The Alcatel SOA used for this study is an InGaAsP bulk device, and device parameters used in the simulations are given in Table 3.1. As in the previous analysis presented in Section 3.2, additional ASE introduced by the SOA was ignored in our calculations. This model was developed in collaboration with Dr. Peter Horak and Dr. Benn Thomsen, and the code was written and implemented in C by Dr. Peter Horak. A detailed flow chart of the model is available in Appendix B.

Table 3.1: Alcatel SOA device parameters used for simulations

Device Parameter	Value
Linewidth enhancement, α	5
Group velocity, υ_g	10^8 m/s
Confinement factor, Γ	0.6
Area, A	2 x 10^{-13} m^2
Differential gain coefficient, a	2.5 x 10^{-20} m^2
Length, L	600 μm
Transparency carrier density, N_o	1.1 x 10^{24} m^{-3}
Carrier lifetime, τ_s	2.6 x 10^{-10} s
Internal loss, α_{int}	4944.2 m^{-1}
Current, I	200 mA
Input intensity, I_o	3 mW
Facet coupling loss	3 dB

In view of the newly developed model, the agreement between measurements and numerical predictions are now discussed. First, experimental and simulation results of the SOA output spectra are presented for input bandwidths of 0.24, 0.5, 1.0 and 1.3 nm (Figure 3.9). As expected, the numerical model closely follows the output

spectra, clearly showing the broadening and distortion observed in the experimental measurements over a wide spectral range. In each case, a red-shift in the peak power wavelength was observed in the SOA output spectrum, along with considerable spectral broadening. For example, for the 0.24 nm slice, the 20 dB bandwidth increased by about a factor of 2 from ∼0.38 nm to ∼0.7 nm after the SOA. Note that the red-shift is more pronounced in the narrower bandwidth slices, where the intensity noise is more significant.

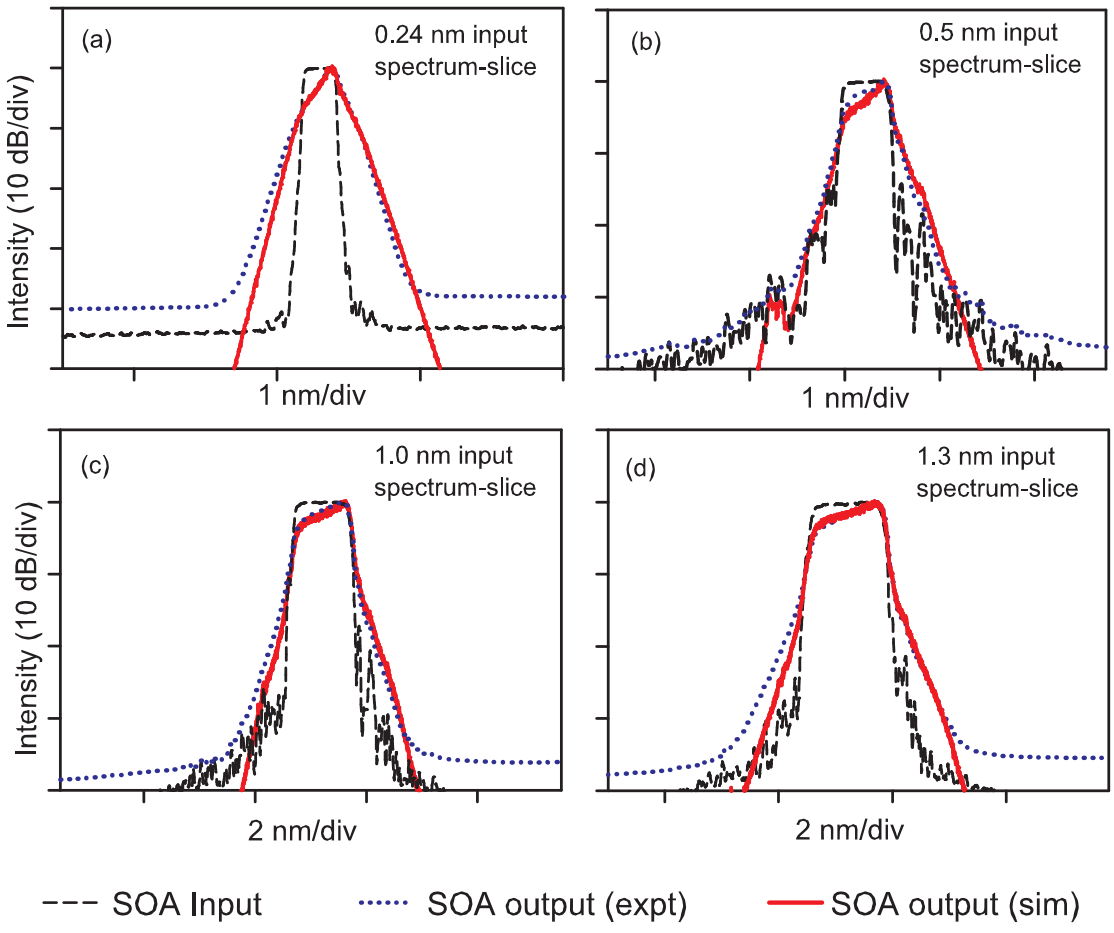

Figure 3.9: Spectra before and after the saturated SOA for 0.24, 0.5, 1.0 and 1.3 nm bandwidth input FBG filters.

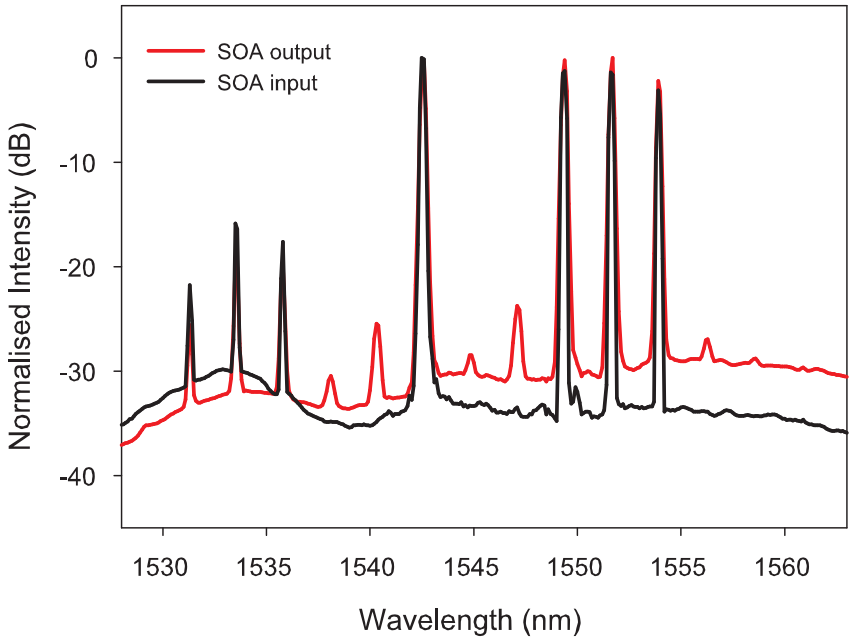

Figure 3.10: Spectra before and after the saturated SOA for a multi-sliced incoherent signal. Evenly spaced additional frequencies present at the SOA output illustrate FWM effects.

Qualitative Approach to Understanding Spectral Distortion

The good agreement observed in Figure 3.9, between measurements and numerical predictions, suggests that Equations (3.6) and (3.7) effectively represent the nonlinear interactions imposed by the saturated SOA. Amplitude-to-phase coupling that occurs in the device as a result of material index perturbations [26], is represented in Equation (3.6), by the linewidth enhancement factor, α, and governs the nonlinear effects of phase modulation and FWM [31,32]. The effects of FWM are illustrated in Figure 3.10 using a multi-sliced thermal light input spectrum; additional frequencies are created at the SOA output due to beating within the saturated amplifier[3].

The spectral broadening that we observe at the SOA output is attributed primarily to the two effects of phase modulation and intra-channel FWM. The relative efficiencies of the two processes depend on the input slice bandwidth; wider slices generate more FWM products, while the phase modulation is more pronounced in

[3]More information on the different nonlinear mechanisms can be found in standard text books on nonlinear optics [33,34].

the narrower bandwidth slices where the larger intensity fluctuations produce greater phase noise [30]. Phase modulation, and therefore induced chirping/broadening has the effect of shifting the peak power toward longer wavelengths as the light travels through the amplifier as discussed in [31], thus accounting for the red-shift observed in experiment and simulation.

3.3.6 Noise Suppression as a Function of Input Bandwidth

Previously in Section 2.4, intensity noise of incoherent light was found to decrease with increasing slice bandwidth. Corresponding RIN measurements were performed to investigate the dependency of noise suppression on input slice bandwidth.

All filter transfer functions used in this experiment are similar in shape with steep roll-off, as illustrated previously in the inset of Figure 2.7. The numerical model gives good agreement with measured values, as shown in Figure 3.11. For bandwidths above 0.8 nm, the discrepancies are due to the detector noise floor in the measurement; once the detector floor is factored into the simulation, the predicted values closely match the experimental results. I also include SOA output RIN measurements after a 5 nm ASE blocking filter for comparison with simulations which do not include added ASE. For lower input bandwidths where the measurements are not detector noise limited, we observe an increase in the RIN due to ASE filtering, giving better agreement with the model. This suggests that the added ASE in fact aids in the noise suppression process.

Similar issues have been addressed by Shtaif and Eisenstein in their studies on coherent light propagation in a saturated SOA [27, 35, 36]. In view of our observations, it is appropriate to briefly discuss their work, specifically with regard to the contribution of amplifier ASE to the nonlinear noise suppression process. One study presented by the authors investigated the effect of amplifier ASE on the noise properties of a nonlinearly amplified 'clean' input signal [27]. Here, they show that added amplifier noise is suppressed as the saturation level increases, and suggest that this is caused by nonlinear interactions between the input light and the amplifier ASE. The effect on signal noise after propagation through a noiseless amplifier has also been considered in another investigation [35], where it was shown that the intensity noise

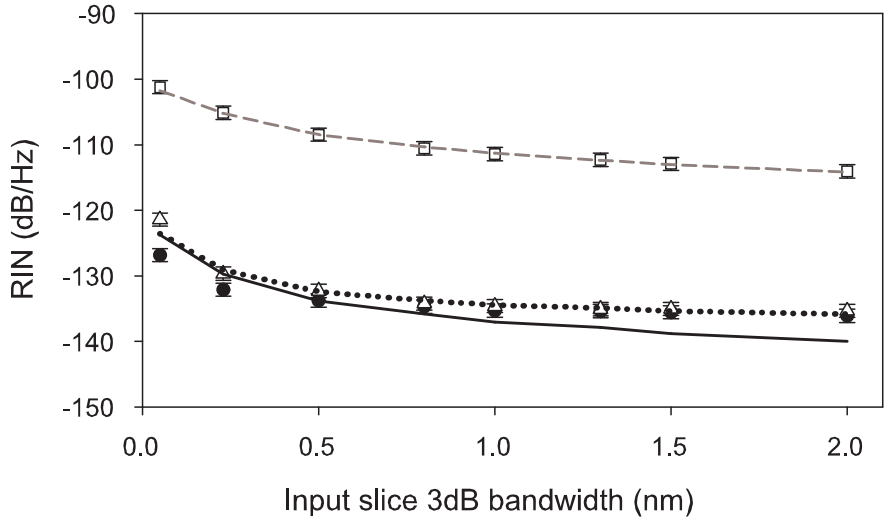

Figure 3.11: Measured (□) and predicted RIN (- -) at SOA input, measured (•) and predicted RIN (—) at SOA output, measured SOA output RIN after ASE filter (Δ) and predicted RIN at SOA output with detector floor (....) as a function of input filter bandwidth.

of the coherent signal was significantly suppressed. However, the authors have not considered the interactions between amplifier ASE and intensity noise in the input signal. Nevertheless our observations presented above indicate an increase in noise when amplifier ASE is filtered. The added ASE appears to suppress the noise of the input, increasing the signal SNR. However, a direct analysis and claim is not possible at this time, since our model does not include amplifier noise, and experimentally the effects of ASE within the amplifier cannot be eliminated. Note that in my experiments, the input to the SOA is far noisier than in [35]. My results, together with these previous studies, suggest that nonlinear interactions occur between all spectral components propagating through the amplifier, including added ASE by the amplifier.

The results presented in Figure 3.11 show RIN improvement at the SOA output with increasing input slice bandwidth. A RIN suppression of ∼25 dB is observed in simulation for all input bandwidths, a substantial deviation from the properties of thermal light. These results are in contradiction to previous reported measurements [22] where the electrical SNR of the SOA output light (post modulation) was observed to be independent of input bandwidth. I attribute this reported bandwidth independence to limitations in measurement equipment (such equipment limitations

were also visible in Figure 3.11 where the measured RIN at filter bandwidths greater than 0.8 nm were invariant with increasing slice width; in this regime the detector thermal floor obscures actual suppression benefit.)

3.4 Post-SOA Filtering

As discussed previously, my initial investigations into SOA-based noise suppression revealed that spectral filtering of the SOA output spectrum gives rise to increased intensity fluctuations, thus reducing the benefit of the technique. However, in communication applications, it is essential to perform spectral filtering at the receiver/demultiplexer for channel selection purposes. Thus in order to carefully assess the penalty of spectrally filtering the broadened SOA output, I measured the RIN of the post-SOA filtered signal as a function of the *receiver* filter bandwidth (Figure 3.12). Note that excellent agreement between experimental and simulation results is once again obtained, and the signal quality was seen to degrade with decreasing receiver filter bandwidth. In Figure 3.12, I have also shown the SOA output RIN for the equivalent thermal light spectrum (squares), calculated numerically as discussed in Section 2.3.

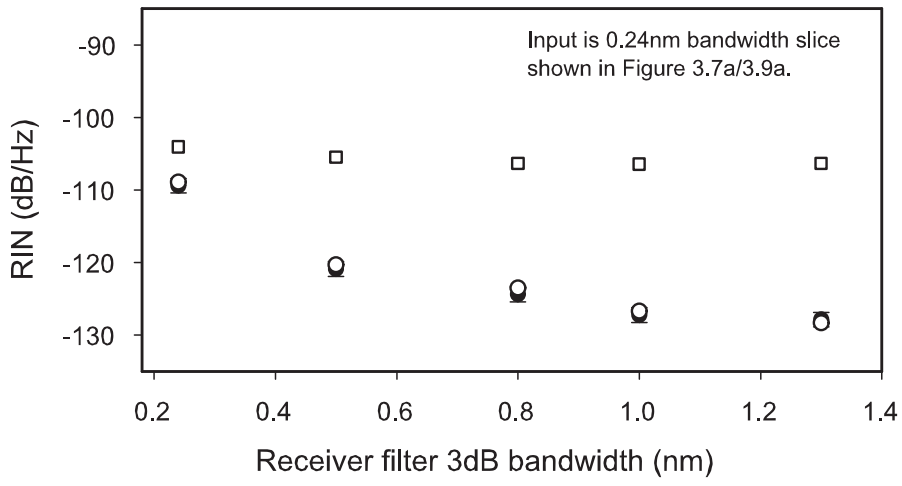

Figure 3.12: Measured (•) and predicted (○) SOA output RIN for varying receiver filters. Simulation results include detector floor. SOA output RIN predicted from received spectra, using a thermal light model, is also shown (□). Receiver filter spectra are as shown in Figure 4.6 inset.

Recall that using Equation (2.8) we are able to predict the RIN for an arbitrarily

shaped incoherent light spectrum. The results show that, unlike thermal light, the intensity-smoothed output exhibits a pronounced increase in noise as the receiver filter bandwidth is reduced, suggesting once again, a deviation from the statistical properties of incoherent light. This observed noise increase relates directly to the extent of spectral filtering.

Origin of Post-SOA Filtering Effects

To understand the origins of the noise increase, it is important to appreciate the physical mechanisms underpinning the noise suppression process. As previously suggested, the nonlinearities that occur within the gain-saturated SOA cause interactions between the various spectral components present in the amplifier; this includes the original input signal, new frequencies generated by the nonlinear processes, and added ASE.

3.4.1 Noise Correlation Measurement Procedure

I investigated the impact of these interactions on the statistical properties of the intensity-smoothed light by measuring the correlation between the intensity fluctuations of the different spectral components in the SOA output. My experimental procedure was as follows.

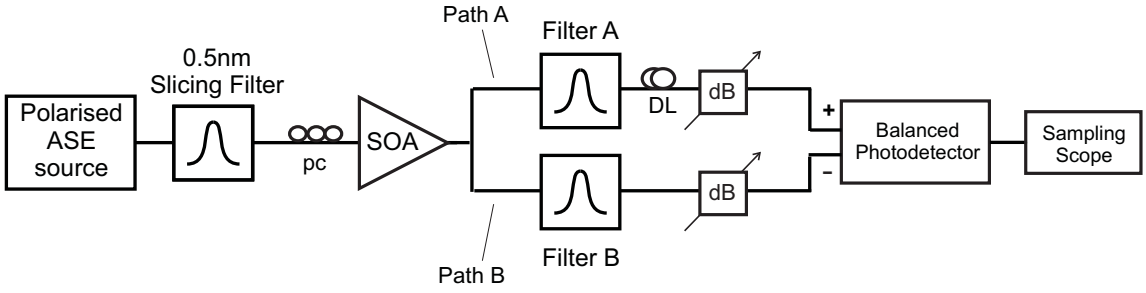

Figure 3.13: Experimental setup to investigate the intensity correlation between different spectral components in the SOA input and output light. pc: polarisation controller, DL: delay line

Polarised ASE light of 0.5 nm spectral bandwidth was launched into the saturated amplifier, and after amplification and intensity smoothing, the signal was split into

two paths as shown in Figure 3.13. Both paths contain similarly shaped 0.24 nm filters (Filters A and B) which were used to slice the SOA output spectrum. The centre wavelength of Filter A was held fixed, while Filter B was tuned across the SOA output spectrum as illustrated in Figure 3.14. A delay line was used to match the path-lengths of the two branches (matched to within 55 ps), and the powers of paths A and B were balanced for the zero-offset position of Filter B. The signals were then detected by an 800 MHz New Focus balanced differential receiver and viewed on a high speed sampling oscilloscope. The histogram function of the scope was used to measure the standard deviation of the fluctuations in the intensity *difference* between the two signal paths, as well as the standard deviation of the intensity noise in each path individually (using the shutters of the attenuators). These measurements were repeated while the centre wavelength of Filter B was scanned across the SOA output bandwidth. The covariance of the intensity in the two frequency segments is then calculated using the well known relation [37],

$$Var(A-B) = Var(A) + Var(B) - 2Cov(A,B) \tag{3.8}$$

where $Var(A)$ and $Var(B)$ represent the intensity variance of the signals in paths A and B respectively, and $Cov(A,B)$ is the covariance of the intensity in the two frequency segments. The *correlation coefficient*,

$$\rho = \frac{Cov(A,B)}{\sqrt{Var(A)Var(B)}} \tag{3.9}$$

is then calculated, to compensate for the change in power as Filter B is tuned across the SOA output spectrum. The correlation coefficients calculated from the measured data for both the SOA input (thermal light) and output are shown in Figure 3.15, along with simulation results. The thermal light measurements were obtained by removing the SOA from the experimental setup shown in Figure 3.13. Filter B was tuned from -0.4 nm to +0.3 nm relative to the centre wavelength of Filter A. Note that due to limitations in available filters, Filter A is not aligned to the centre of the input slice, but is in fact offset approximately +0.1 nm as depicted in Figure 3.14.

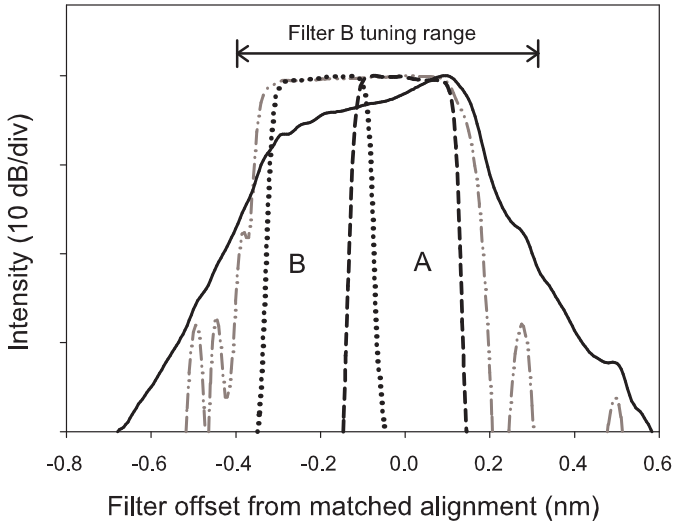

Figure 3.14: Spectra of 0.5 nm thermal input slice (grey dash-dot line), SOA output (solid line), Filter A (short dashes), Filter B (dotted line) for offset of -0.2 nm.

This experiment was also repeated for a 0.8 nm input slice width.

3.4.2 Results and Discussion

For thermal light (Figure 3.15(a)), we see that the correlation coefficient approaches zero as Filter B is detuned from Filter A. The correlation observed at small detunings is due to the spectral overlap between the filters, and as expected, when the bands are disjoint, the correlation is negligible.

In comparison, Figure 3.15(b) clearly shows negative intensity correlations between the different spectral components of the SOA output. These *anti*correlations exist both within the original signal bandwidth ($\rho < 0$ at -0.2 nm offset) and between the new frequency components generated by the nonlinearities of the SOA. For filter detunings of ± 0.1 nm, this effect is partially masked by the significant overlap of the filters.

The correlation results for the 0.8 nm input slice are given in Figure 3.16. As expected, the same trend is observed, where the SOA output displays noticeable negative correlations. It is difficult to draw a comparison between the relative magnitudes of ρ for the 0.5 and 0.8 nm slice bandwidths considered above (Figures 3.15 and 3.16). When the input filter bandwidth is varied, the intensity noise level into

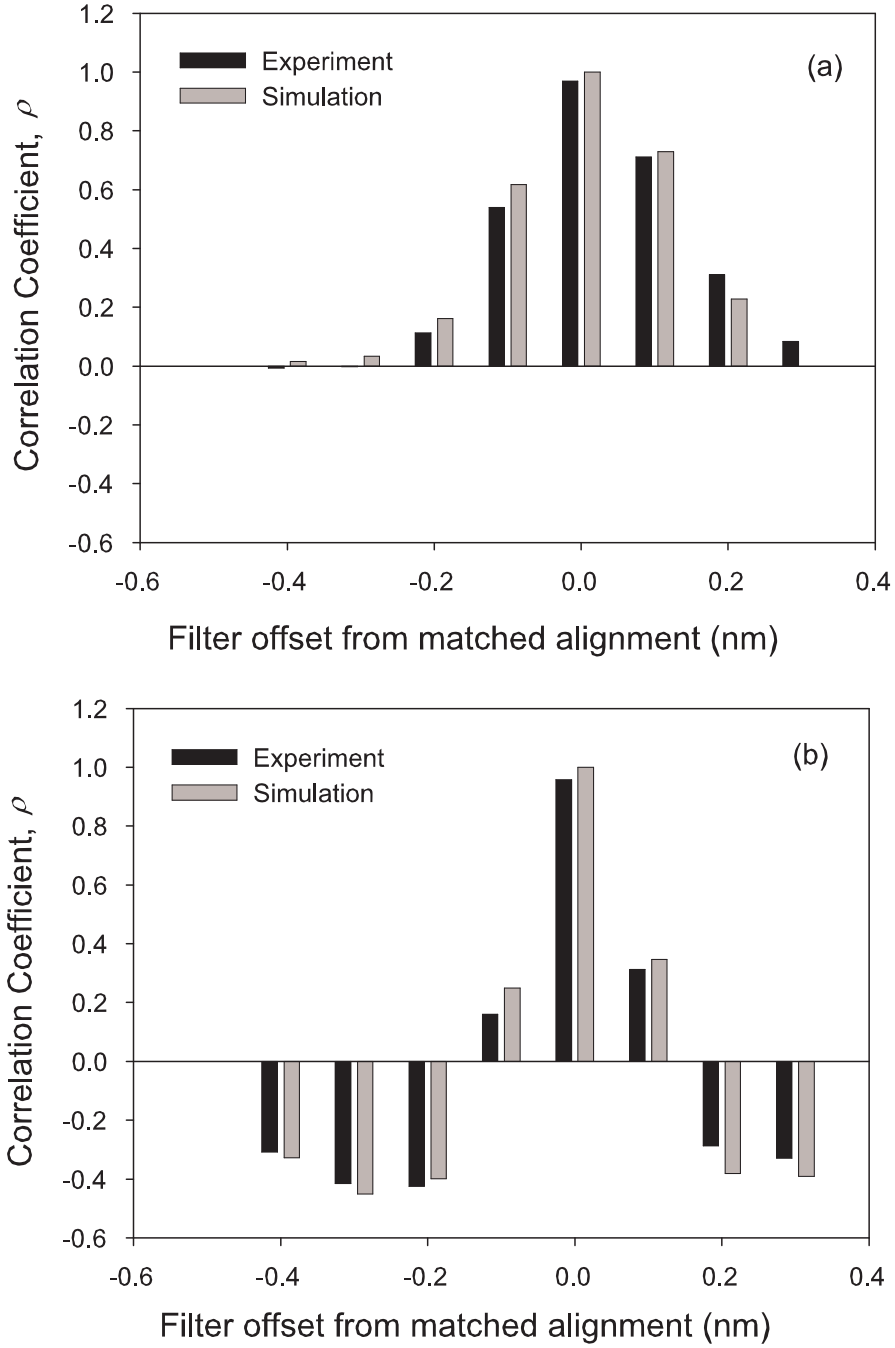

Figure 3.15: Experimental and simulation results of the correlation coefficient ρ, for (a) the spectrum-sliced input light (0.5 nm bandwidth) and (b) the SOA output light, as a function of Filter B offset.

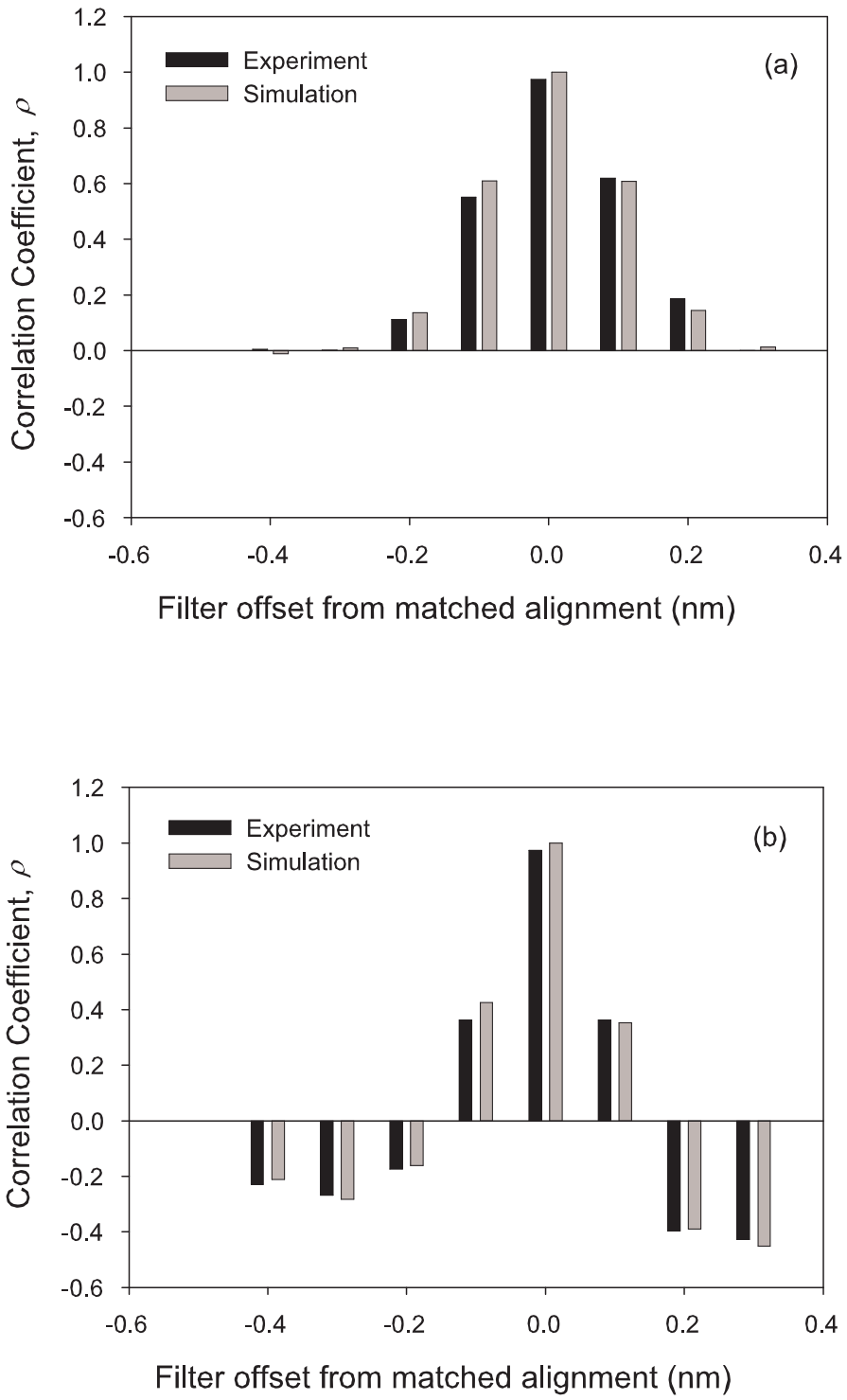

Figure 3.16: Experimental and simulation results of the correlation coefficient ρ, for (a) the spectrum-sliced input light (0.8 nm bandwidth) and (b) the SOA output light, as a function of Filter B offset.

the saturated amplifier changes accordingly, thus modifying the nonlinear interactions between different spectral components. It is important to note that the width and position of Filters A and B, relative to the SOA output spectrum, will affect the absolute correlation value. Thus a direct comparison between the two measurements is not possible with the current measurement procedure.

Qualitative Approach to Understanding Post-SOA Filtering Effects

The distinct anticorrelations observed in the noise-suppressed light clearly confirm the non-thermal properties of the SOA output. As discussed previously in Section 3.2, the nonlinear gain compression effects occur over the entire gain bandwidth of the SOA, and act to compress any intensity fluctuations present in the input light. The fluctuations of an individual frequency component inversely modulate the gain, and this gain modulation is in turn imprinted onto the other spectral components propagating through the amplifier. This gives rise to the observed anticorrelation between the different spectral components present in the SOA output light. The superposition of these anticorrelated noise components then yields reduced fluctuations in the total output intensity. Optical filtering after the SOA removes frequency components that contribute to the total noise suppression, thus compromising the added benefit of the technique. Attention is drawn to the fact that anticorrelations were observed not only within the original signal spectrum but also between additional frequencies introduced by FWM and phase modulation.

3.4.3 Dispersion Effects on SOA Output Light

As the noise suppression depends on the intensity correlation between the spectral components of the SOA output, we would further expect that a phase decorrelation of the various optical frequencies would also lead to RIN degradation. To investigate this, I measured the RIN at the SOA output for varying fibre lengths, i.e. varying levels of dispersion. The experimental and simulation results are shown in Figure 3.17. The calculated values are obtained by applying the appropriate amount of phase delay to the SOA output temporal field. Also shown in the graph is the system output RIN for the spectrum-slice without noise suppression, which as discussed previously in

Section 2.4, is unaffected by dispersion. However, the RIN of the SOA output light clearly degrades with increasing dispersion. This effect becomes observable as the introduced group delay approaches the period of the suppressed noise fluctuations.

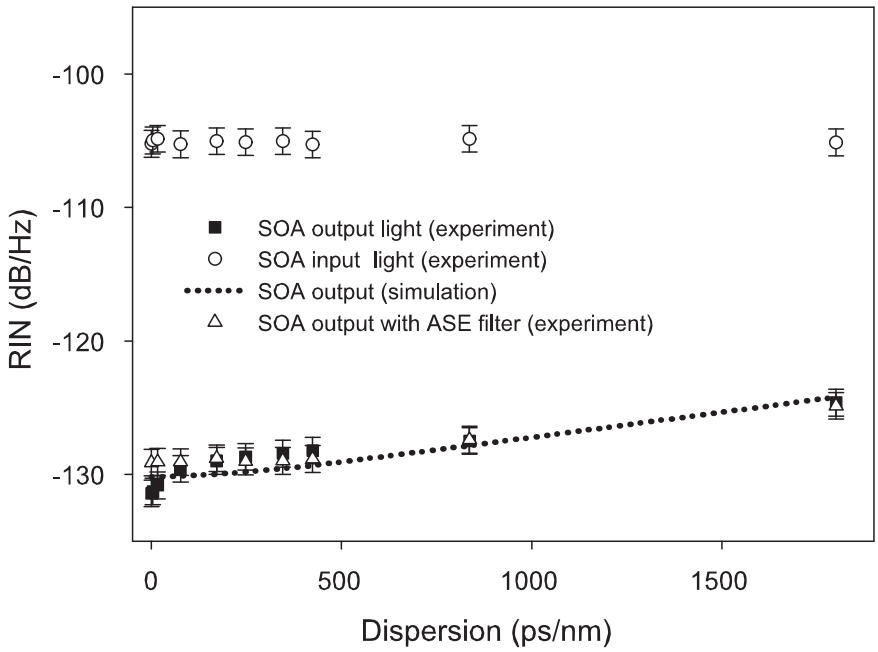

Figure 3.17: RIN (at 100 MHz) vs. dispersion: Measured SOA input (□) and output RIN (•), predicted SOA output RIN (...) and measured SOA output RIN with ASE blocking filter (△).

At very low levels of dispersion, the measured SOA output RIN exhibits a steeper rise than the corresponding calculated values. However it is observed that adding a 5 nm ASE blocking filter at the SOA output removes this trend. This suggests that the discrepancy is caused by the absence of amplifier noise in the numerical model, reinforcing the argument that ASE participates in the nonlinear noise suppression process (see Section 3.3). Due to its wide bandwidth, the ASE rapidly looses correlation with increasing dispersion. This eliminates the ASE contribution to the noise suppression, as seen from the good agreement between experiment and simulation at higher levels of dispersion.

I have also confirmed that the dispersion induced signal degradation can be overcome by employing dispersion compensation. Using dispersion compensating fibre (DCF), the RIN (at 100 MHz) after 25 km of single-mode fibre was reduced from -125.95 dB/Hz to -131.05 dB/Hz (the measured RIN for zero dispersion was

$\sim$ -131.3 dB/Hz; the slight discrepancy is due to the fact that the exact length of DCF was not available for full compensation of the 25 km of single-mode fibre, thus leaving a small amount of residual net dispersion).

3.5 Temporal Coherence of SOA Output Light

As discussed in Section 3.3, the nonlinearities of the gain-saturated SOA give rise to phase modulation of the input thermal light field, which in turn causes the spectral broadening observed at the amplifier output. This excess phase noise introduced by the SOA is described in the equations by the device linewidth enhancement factor, α. An alternative way of assessing this phase noise increase is by measuring the temporal coherence before and after noise suppression.

In this section I discuss the impact of the noise suppression process on the temporal coherence of the input incoherent field. The temporal coherence can be quantified using the interference pattern or interferogram generated at the output of an interferometer as the path length difference is varied. By measuring the interference fringe visibility, which is the envelope of the interferogram pattern, the coherence time of the light can be calculated [11]. Further details on visibility measurements and temporal coherence can be found in Appendix C. By measuring the maximum and minimum detected intensity (I_{max} and I_{min} respectively) at the output of the interferometer, the visibility, $V(\tau)$ can be calculated using,

$$V(\tau) = \frac{I_{max} - I_{min}}{I_{max} + I_{min}} \tag{3.10}$$

My experimental setup is shown in Figure 3.18 and uses a fibre based Mach-Zehnder interferometer (MZI) constructed using two 3 dB couplers. The variable delay line is used to change the relative time delay of the signals in the two different arms of the interferometer. The piezo-electric device acts as a full-wavelength phase-shifter to ensure accurate capture of the minimum and maximum intensity of the interferogram pattern. The use of the piezo-electric device in this manner reduces the impact of temperature fluctuations on the measurement. The polarisation controllers also help to minimise polarisation-induced errors in the experiment, while the variable

optical attenuator is used to match the powers in both arms of the interferometer. The output of the MZI is characterised using a 125 MHz low noise detector and a digital oscilloscope. The narrowband incoherent input to the SOA was generated by slicing the ASE source bandwidth with a 0.1 nm bandwidth FBG; the filter spectral profile is shown in Figure 3.19.

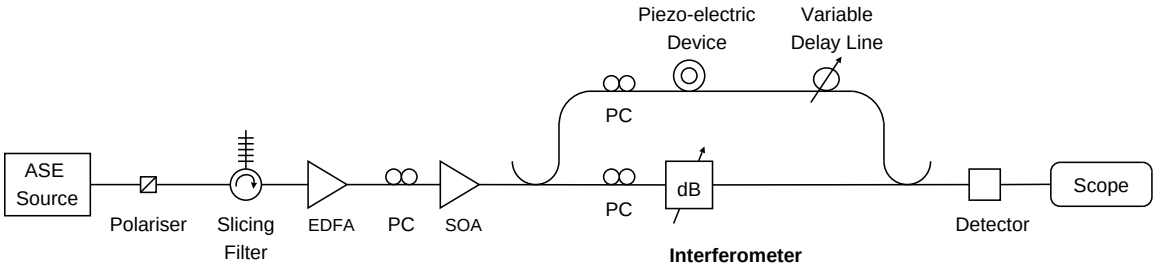

Figure 3.18: Visibility measurement to assess coherence of SOA input and output light.

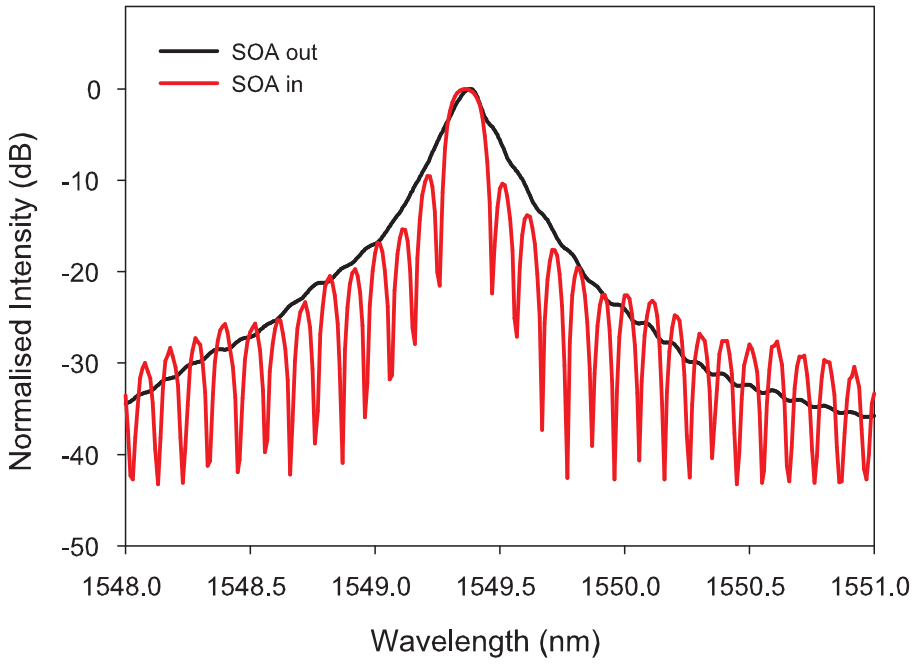

Figure 3.19: SOA input and output optical PSD.

The measured visibility pattern for both the SOA input (thermal light) and SOA output light is given in Figure 3.20 as a function of the path delay between the two interferometer arms. Also shown is the calculated visibility for both scenarios. Recall

that the according to the Wiener-Khinchin theorem, the autocorrelation function of an optical disturbance E(t), and its PSD form a Fourier transform pair [11]. It is therefore straight forward to calculate the visibility pattern, which is the normalised self coherence function (autocorrelation) $\gamma(\tau)$ of the optical field. As expected, excellent agreement is obtained between calculations and measurement.

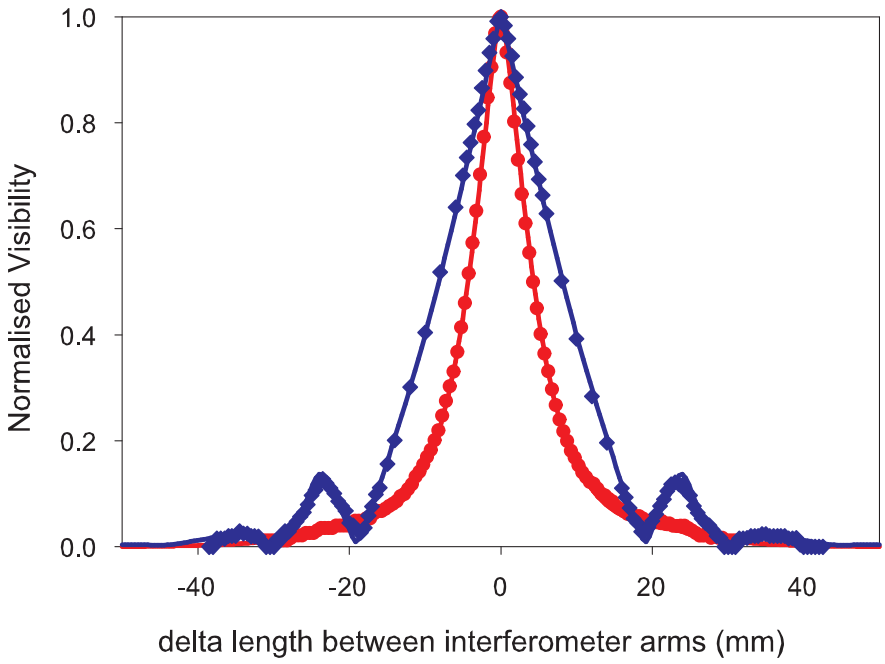

Figure 3.20: Experimental visibility measurements for SOA input (blue diamond) and output (red circle) and calculated values for the SOA input (blue line) and output (red line).

$$\tau_c = \int_{-\infty}^{\infty} |\gamma(\tau)|^2 d\tau \tag{3.11}$$

In order to calculate the temporal coherence, τ_c, I use Equation (3.11) as defined by Goodman [11], where $|\gamma(\tau)|$ is the measured visibility pattern. The coherence time of the 0.1 nm narrowband input used in this investigation is calculated to be 38 ps (coherence length of 11.30 mm) while the phase noise introduced by the SOA reduces this to 22 ps (coherence length of 6.5 mm).

On similar lines, Munroe et al. have theoretically quantified the maximum visibility at the output of the interferogram, as a function of α, when the intensity smoothed light is interfered with the incoherent input light field [30]. As expected, the visi-

bility decreases with increasing α as a result of the increased phase noise. These calculations together with my measurements, demonstrate the reduction in temporal coherence at the SOA output, as a result of the excess phase noise introduced by the non-zero α-parameter.

3.6 Improving Post-SOA Filtered Signal Quality

Optical filtering at the receiver is a necessity in communication applications such as spectrum-slicing and spectral amplitude coded OCDMA, where the desired channel selection is based on relative spectral positioning. In order to obtain high channel density, it is advantageous to use steep, narrow channel filters, and corresponding matched receiver filters. However, as we have observed, spectral filtering at the receiver poses considerable difficulties for systems employing SOA-based noise reduction. In view of these challenges, I now discuss potential techniques to overcome the post-SOA filtering effects and improve the signal quality at the receiver.

3.6.1 Red-shift compensation

One simple technique which makes a noticeable improvement in signal RIN is detuning of the receiver filter to align with the shifted peak of the SOA output. As discussed previously, a red-shift in the peak wavelength occurs as the light travels through the saturated amplifier. By positioning the post-SOA receiver filter to account for this frequency shift relative to the input spectrum slice we observed a noticeable improvement in signal quality. Figure 3.21 shows the RIN after receiver filtering as a function of the frequency offset between the 0.24 nm input spectrum slice and the receiver filter. The lowest RIN is obtained when the receiver filter is aligned $\sim$10 GHz (0.08 nm) below the centre frequency of the input spectrum slice. The observed RIN improvement is due to the decrease in filtering of the high intensity spectral components present in the SOA output light.

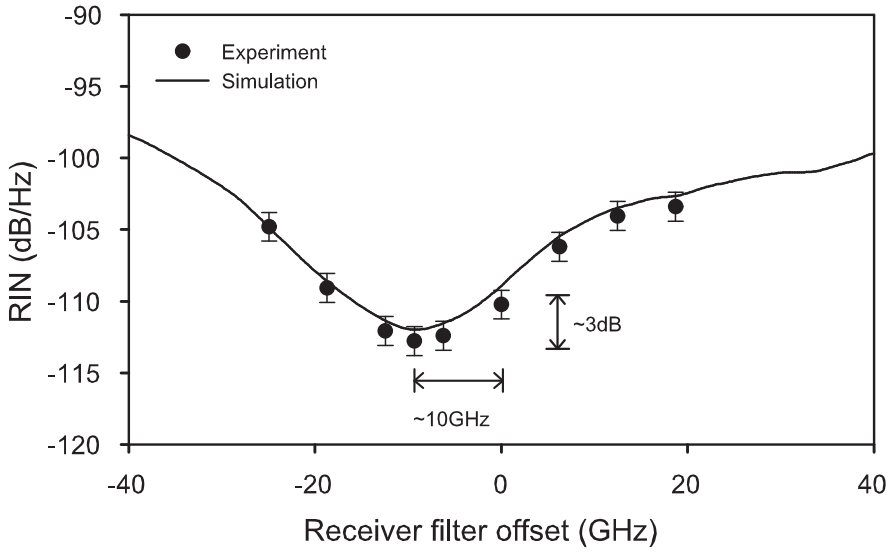

Figure 3.21: RIN at receiver filter output, as a function of frequency offset between the 0.24 nm input spectrum slice and a 0.24 nm receiver filter (same shape as slicing filter).

3.6.2 SOA design optimisations

3.6.2.1 Linewidth-Enhancement factor

We have also used the numerical model to investigate potential improvements in received signal quality by optimised SOA design. As discussed previously, the phase modulation and FWM processes within the SOA are governed by the device linewidth-enhancement factor, α. As these effects are responsible for the observed spectral distortion, we used simulations to assess the impact of α on the post-SOA filtered signal. Using a 0.24 nm narrowband input, we calculated the RIN as a function of α directly after the SOA and at the output of the receiver filter. Simulation results are shown in Figure 3.22, for post-SOA receiver filters (aligned to input filter) of 0.24 and 0.5 nm bandwidths.

As expected [30], the noise suppression directly after the SOA (shown by the dotted curve in Figure 3.22) is not affected by α. However, α clearly has a strong effect on the post-SOA filtered signal quality. Typical bulk SOAs have linewidth-enhancement factors between 3 and 8 (recall that $\alpha = 5$ was used as a best fit to our experimental data). Reducing the linewidth-enhancement factor of semiconductor laser diodes is a subject of ongoing research, and advances in this area have shown that α can be

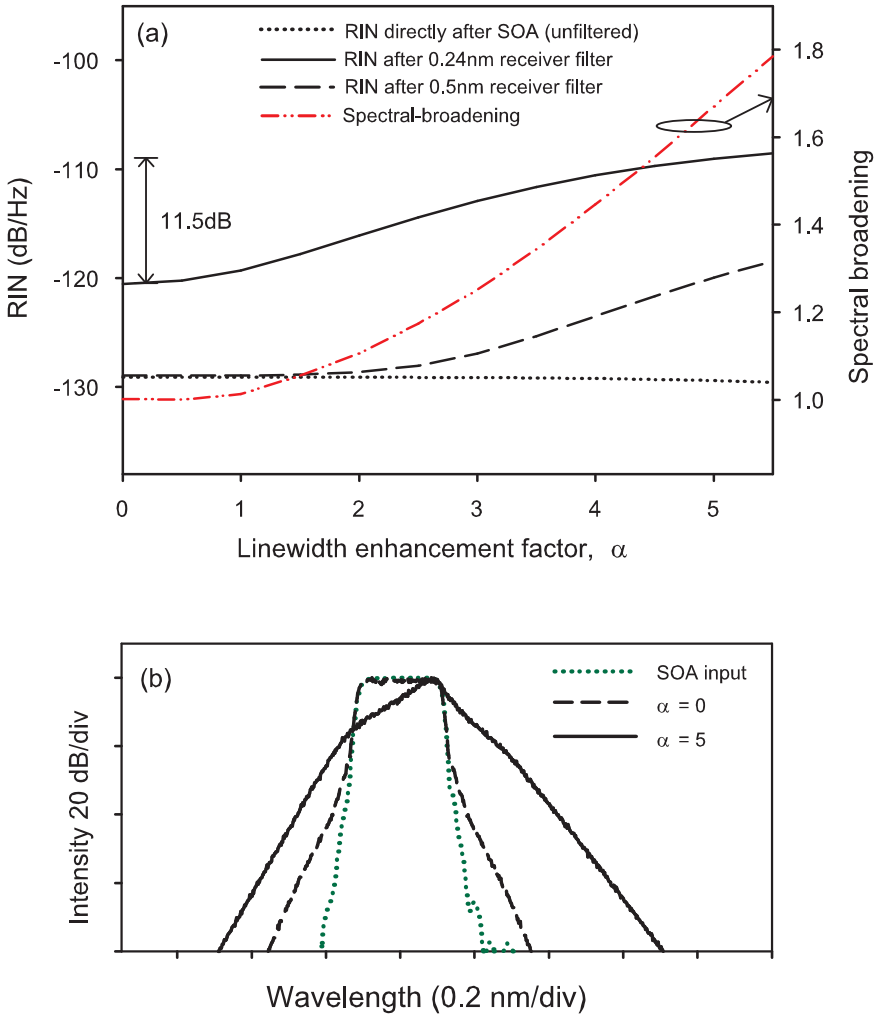

Figure 3.22: Simulation results for varying α: (a) Unfiltered SOA output RIN, RIN at filter output (0.24 and 0.5nm filters), and spectral broadening (ratio of SOA output 10dB bandwidth to input 10dB bandwidth) (b) SOA output spectra for $\alpha = 0$ and 5. Input spectrum also shown.

reduced by optimising the design of the device. Particularly, optimised quantum well and quantum dot structures have been shown to yield lower linewidth enhancement factors [38, 39]. By reducing α in our simulations, we obtained a maximum RIN improvement of 11.5 dB over the experimental values for the 0.24 nm filter and a 9 dB improvement with the 0.5 nm filter. The spectral broadening at the SOA output is also shown relative to the input filter bandwidth, illustrating the significant influence of the SOA linewidth-enhancement factor on the slice bandwidth. As α is reduced, the spectral broadening due to phase modulation-induced chirp decreases as does the FWM. This reduces the impact of post-SOA filtering, resulting in improved RIN. For α=0 slight broadening occurs in the tails of the spectrum [40] due to remaining FWM contributions. These simulation results clearly show that the post-SOA filtered signal quality can be improved significantly by reducing the linewidth-enhancement factor.

It is worth noting that recent progress in the development of quantum dot SOAs shows potential in achieving both low α and high gain compression [41]. This would ensure excellent noise suppression, while minimising the spectral broadening.

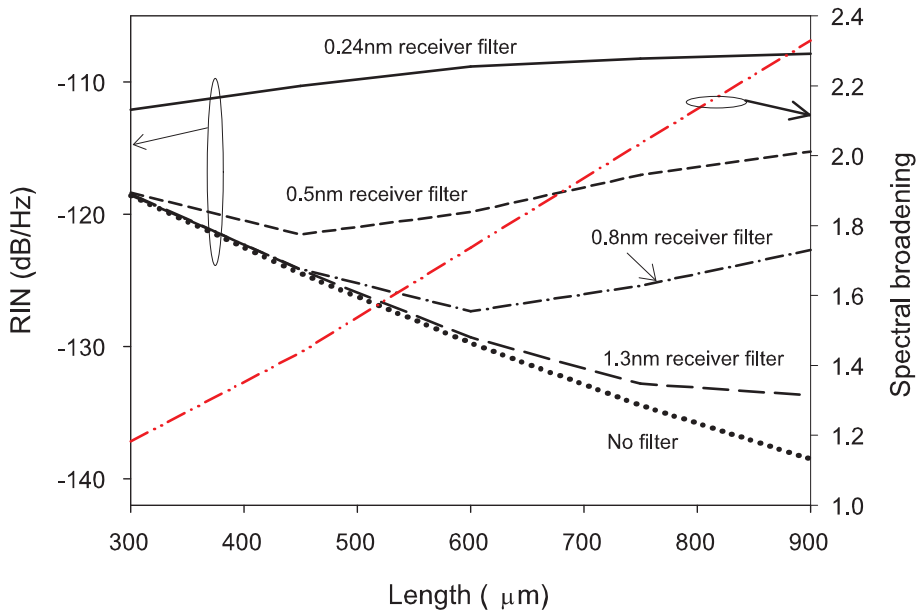

Figure 3.23: Simulation results for varying device length, L: Unfiltered SOA output RIN (dots), RIN at filter output (1.3 nm (long dashes), 0.8 nm (dash-dots), 0.5 nm (short dashes) and 0.24 nm filters (solid)), and spectral broadening (ratio of SOA output 10 dB bandwidth to SOA input 10 dB bandwidth, given by red curve). Device current per unit length was held fixed.

3.6.2.2 Device Length

In Section 3.3 I discussed the use of multi-stage SOAs for additional suppression benefit over the single stage amplifier. Similar benefits are possible by increasing the length of the single-stage device. This was examined using simulations where we calculated the RIN as a function of SOA length for different receiver filter bandwidths (Figure 3.23).

Optimisations of device parameters (e.g. gain, area) to allow for superior noise suppression was also discussed briefly in [23]. However it is important to note that better noise suppression at the SOA output does not necessarily result in improved post-SOA filtered signal quality, and this should be considered when optimising device parameters. For example, from Figure 3.23 we see that as the length L increases, the broadening significantly increases (shown by the red line), while also providing higher noise suppression benefit at the SOA output (dotted line). Consequently there is an optimum device length for which the increased suppression benefits counterbalance the post-filtering effects. For the 0.24 nm receiver filter, the filtering effects dominate and the received signal quality does not improve with increased device length.

Similar results are obtained in simulations when varying the device gain. Note that decreasing α in the design, as discussed in the preceding subsection, will reduce the impact of post-SOA filtering, allowing RIN improvement with increasing device length (or gain).

3.7 Summary and Discussion

In this chapter I have examined the fundamental properties of the noise suppression benefit offered by a gain-saturated SOA. In particular, special emphasis was placed on understanding parameters that influenced the suppression bandwidth, as this directly determines the useable data rate for communication applications incorporating this technique.

The nonlinearities of the saturated amplifier also generates spectral broadening, and I have demonstrated that optical filtering of this broadened output causes an increase in the intensity fluctuations of the intensity smoothed signal. Correlation characterisations performed on the intensity smoothed light show strong anticorrelations between the intensity fluctuations of the constituent spectral components. The observed increase in noise due to optical filtering, originates from the loss of these intensity correlations when the SOA output spectrum is altered. Any occurrence that affects these correlations, such as dispersion or polarisation, can also lead to signal degradation.

It is also shown that the spectral filtering effects can be overcome by system and device design optimisations. In particular, significant improvement in signal quality can be achieved by decreasing the device linewidth-enhancement factor, α, while maintaining a high level of gain compression. Although the design parameters of an actual SOA device are intricately related, for the simulations presented in Section 3.6, we have varied the device parameters independently of each other. It should therefore be appreciated that our work illustrates the *potential* to reduce the undesirable effects accompanying the noise suppression process, and does not in fact address the challenges of designing and fabricating an optimised structure.

Chapter 4

Spectrum-Slicing Applications

Overview: In this chapter I discuss the feasibility of using SOA-based noise reduction in spectrum-slicing applications, in view of the broadening and spectral filtering effects detailed in Chapter 3. The increase in noise due to receiver filtering is quantified in terms of Q, and the associated system penalty is assessed. Despite the signal degradation caused by post-SOA optical filtering, narrow receiver filters are required to reduce the crosstalk in high channel density spectrum-sliced systems. I characterise this tradeoff and show that there is an optimum receiver filter bandwidth for which crosstalk and intensity noise counterbalance. In this chapter I also present investigations into the performance of the saturated SOA for simultaneous noise suppression and modulation. Finally, a comparative study of the different SOA-based noise reduction approaches (for spectrum-slicing applications) is presented, and the relative merits of the different techniques are discussed.

4.1 Background

Spectrum-slicing using incoherent sources has been proposed as an attractive and viable solution for cost-sensitive WDM access networks. It is a method of sharing a single broadband optical source (such as an EDFA, high power LED or SLD) among many user channels by allocating a unique spectral-slice to each channel [42].

It is perhaps appropriate to point out that the term *spectrum-slicing* is not reserved for this incoherent technique alone, but is also generally used to denote any

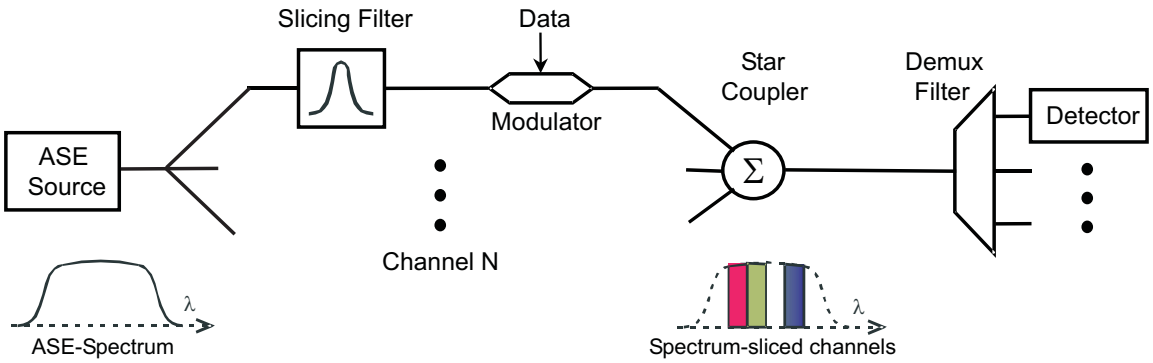

Figure 4.1: Spectrum-sliced WDM using a broadband incoherent light source.

approach whereby a broadband spectrum is sliced to form channels. For example, greater than 100 channels have been generated using spectral-slices from a femtosecond mode-locked pulse source which were subsequently transmitted over 362 km at 2.35 Gb/s per channel [43]. However, coherent methods require expensive sources and do not provide the cost advantages and low complexity benefits offered by the incoherent approaches. Another *spectrum-slicing* method is to use a low power LED slice *per channel* whereby the more costly, wavelength specific lasers are replaced by individual LEDs [7, 44]. Direct modulation of the LED offers advantages for the upstream-link where a low power LED can be used at each subscriber node. For the purposes of this work, I consider spectrum-slicing using a shared broadband incoherent source (see Figure 4.1). It has the advantage of being more economical in the downstream-link where a single shared source can be used among multi-users at the head-end. However, it is to be appreciated that the principles and results that are discussed in this chapter are valid for any scheme utilising a spectrally filtered incoherent source.

As discussed previously in Section 2.4, due to the excess intensity noise present in thermal light, the SNR of a single spectral-slice cannot be improved by increasing the signal power. For a given channel width, this intensity noise imposes an upper limit on the achievable system performance and the signal quality can only be improved by reducing the bit rate and/or increasing the channel bandwidth. However, the use of larger slice widths results in increased dispersion and lower achievable channel

counts.

To address this limitation of incoherent sources, several intensity noise suppression techniques have been investigated in the context of spectrum-slicing. A novel opto-electronic compensation scheme was proposed in [19], where the noise was reduced by subtracting out the fluctuations from the forward propagating light. Successful transmission at 2.5 Gb/s using a 0.23 nm spectral-slice has been demonstrated using this technique. However, the precise phase and gain matching required in the associated RF circuitry increases the overall system complexity. An all-optical method using intra-channel FWM has also been demonstrated to reduce intensity noise by significantly increasing the received channel bandwidth and thus the SNR [20]. The FWM was produced at the receiver using a high power EDFA and 20 km of dispersion shifted fiber. Intensity noise reduction is achieved due to the bandwidth expansion of the spectral-slice resulting from intra-channel FWM. A BER $< 10^{-10}$ is demonstrated in [20] at 2.5 Gb/s using a 0.1 nm input slice; the final channel bandwidth was expanded to $\sim$1.64 nm.

As discussed previously, the nonlinearities of a saturated SOA can also be used to improve the signal quality of the spectrum-sliced incoherent light. This technique is more compact than the bandwidth expansion using dispersion shifted fiber and offers additional benefits in that the SOA can be used simultaneously for both signal modulation and amplification [10, 45]. The SOA efficiently suppresses the intensity fluctuations in the input light across a bandwidth determined by the device operating point and carrier lifetime, and can be used with channel bit rates as high as several Gb/s. Using this technique, error free transmission at 2.5 Gb/s has been demonstrated with an input slice width of 0.32 nm [22]. Reducing the intensity noise enables finer channel granularity and thus higher spectral efficiency. A representative example (from my own measurements) of the achievable performance improvement is presented in Figure 4.2, which shows eye diagrams with and without noise reduction at a bit rate of 2.5 Gb/s for an input spectrum-slice width of 0.24 nm. The simplicity and effectiveness of this technique makes it an attractive option for spectrum-sliced WDM applications.

However as also discussed previously, optical filtering after the SOA (e.g. in a

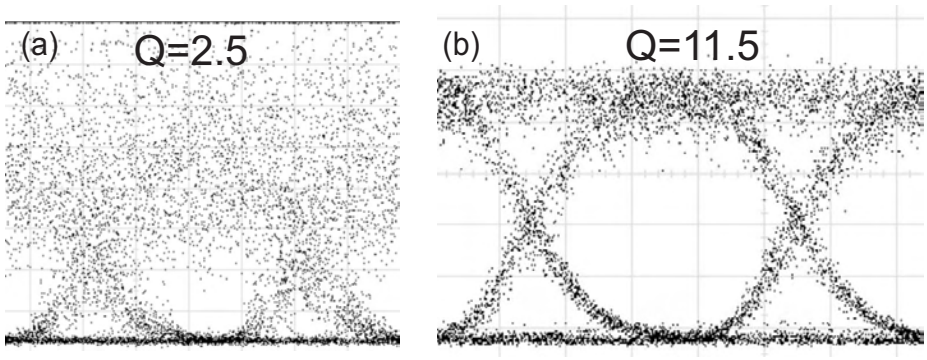

Figure 4.2: Eye quality (a) before and (b) after SOA-based noise reduction for a 0.24nm input spectrum-slice at a bit rate of 2.5 Gb/s.

WDM demultiplexer) results in increased intensity noise, thus reducing the noise suppression benefit and degrading the received signal quality [29]. This effect is more pronounced for narrow, steep input spectrum-slices, where the nonlinearities of the SOA cause significant spectral distortion and broadening. In this chapter I focus on some of the system implications of incorporating a saturated SOA at the transmitter, with specific application to spectrum-sliced WDM systems.

4.2 System Implications

The spectral broadening observed at the SOA output and the deleterious effects of onward filtering give rise to a tradeoff between intensity noise and crosstalk in a high channel density spectrum-sliced system. Steeper filtering at the receiver is required to minimise crosstalk, which in turn leads to a degradation in signal quality. An optimum receiver bandwidth is therefore required to maximise system performance.

I investigated this tradeoff in a 3 x 2.5 Gb/s spectrum-sliced system [46]. In a multi-channel configuration, both the crosstalk and the intensity noise are influenced by the receiver/demultiplexer filter bandwidth, although with good receiver filter extinction, the crosstalk will be dominated by the two adjacent channels. For this study I have assumed that the three channel performance is sufficient to represent a higher channel count WDM system.

4.2.1 Spectral Filtering Effects vs. Channel Crosstalk

The experimental setup for the three channel system is shown in Figure 4.3. The ASE from an EDFA is polarised and spectrally sliced into three channels using 0.24 nm FBGs.

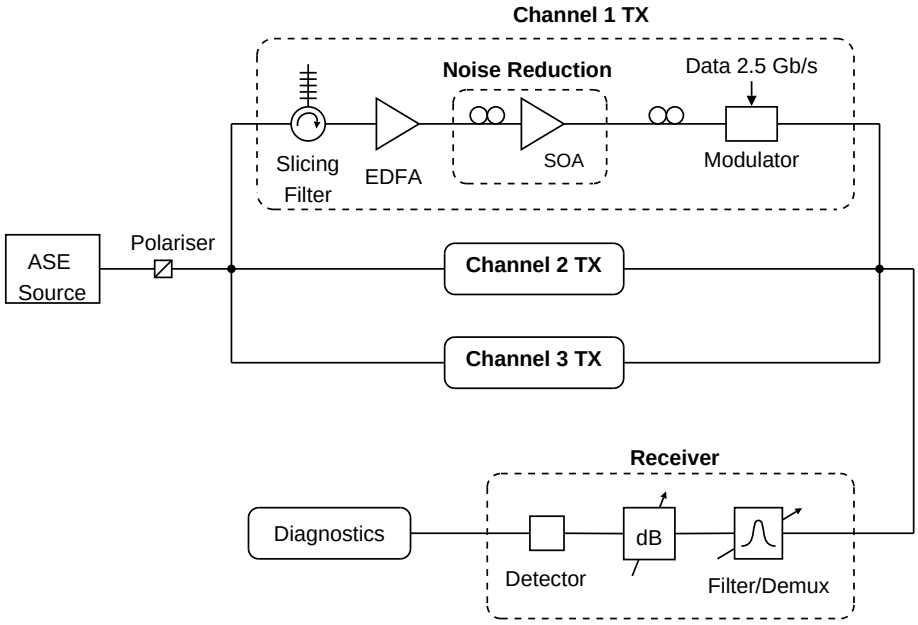

Figure 4.3: Three channel spectrum-sliced WDM system incorporating saturated SOAs for intensity noise reduction. The receiver filter is tuned to channel 1.

The centre wavelength of the subject channel (channel 1) was fixed at 1551.3 nm while the crosstalk channels (channels 2 and 3) were tuned to different wavelengths in order to achieve the desired channel spacings. An EDFA is used after each slicing filter in order to ensure sufficient input power to saturate the SOA. The three channels are then individually modulated with NRZ data at 2.5 Gb/s using $LiNbO_3$ modulators. At the receiver, channel 1 is demultiplexed using a bandwidth-tunable FBG (except for the narrowest receiver width of 0.24 nm, which was obtained by replacing the tunable FBG with a low dispersion grating identical to the input spectral-slice). The dispersion introduced by the receiver filter was verified to have a negligible impact on system performance at 2.5 Gb/s. A high-speed sampling oscilloscope is used to detect the filtered signal and measure the system Q as a function of receiver filter bandwidth. (Recall that Q relates to the total signal RIN across the receiver bandwidth. Q measurements can also be related to BER using the relationship BER=$\frac{1}{2}erfc(\frac{Q}{\sqrt{2}})$,

where *erfc* is the complimentary error function [1].)

Prior to the three channel system measurements, the effects of receiver filtering were characterised for a single channel only scenario (i.e. with channels 2 and 3 disabled). These single channel measurements demonstrate the impact of filtering on source intensity noise in the absence of crosstalk. The Q measurements as a function of the receiver filter bandwidths are shown in Figure 4.4, while the eye diagrams given in Figure 4.5 clearly illustrate the signal degradation caused by post-SOA filtering.

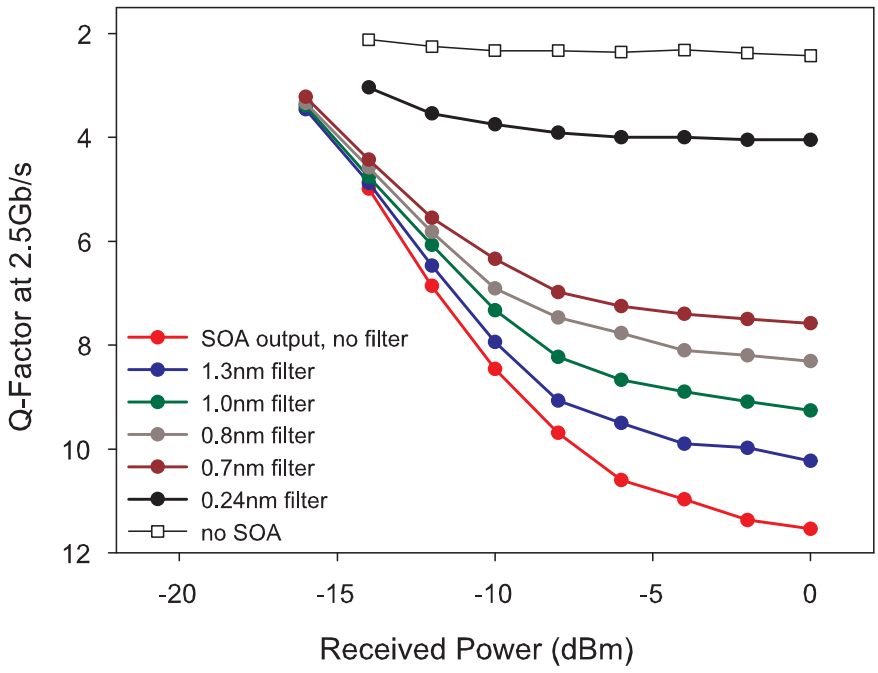

Figure 4.4: Single channel Q measurements as a function of power and receiver filtering. Q decreases with decreasing filter bandwidth.

The corresponding system output spectra are given in Figure 4.6, where the inset shows the receiver filter spectral profiles. For receiver filter widths greater than ∼1.3 nm the system is detector noise limited at power levels $\lesssim$-2 dBm while for narrower receiver bandwidths this limit shifts to lower powers due to the increase in intensity noise. The intensity noise floor of the unfiltered SOA output occurs at Q≈11.5 (BER $\approx 10^{-30}$). However, using a steep 1.3 nm receiver filter increased this noise floor to Q≈10.2 (BER $\approx 10^{-24}$). Although the signal degradation is noticeable here, the absolute measurement is low enough to be unnoticed in a routine BER measurement.

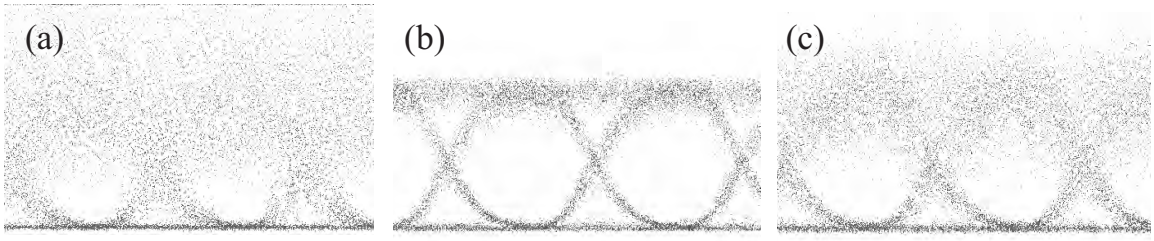

Figure 4.5: Eye diagrams at system output for the following scenarios: (a) no SOA (b) directly at the SOA output (c) SOA followed by 0.24 nm filter.

However, the narrower receiver filters (0.7 nm and 0.24 nm) introduce significant system penalty. Note from Figure 4.6 that due to the flat filter passband, the 3 dB bandwidth of the system output spectrum does not change appreciably as the receiver filter bandwidth is varied. As expected, these system results closely follow the trend observed in the post-SOA RIN measurements presented in Section 3.4 (Figure 3.12).

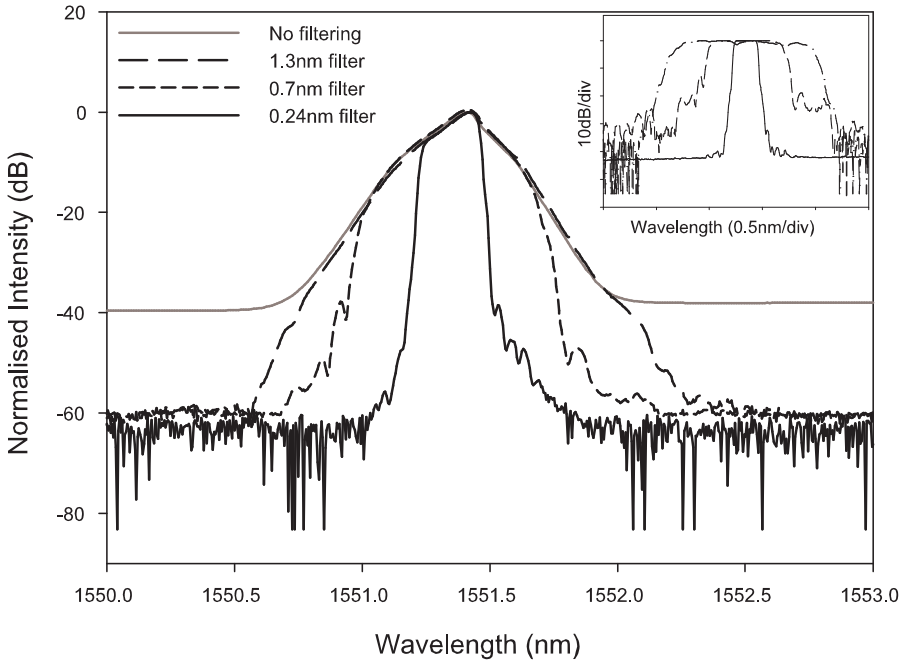

Figure 4.6: Detector input spectrum (system output) for single channel only. Inset shows receiver filter transfer functions.

Having examined the effects of receiver filtering on the intensity noise alone, I next characterised the tradeoff between crosstalk and intensity noise for the three-channel

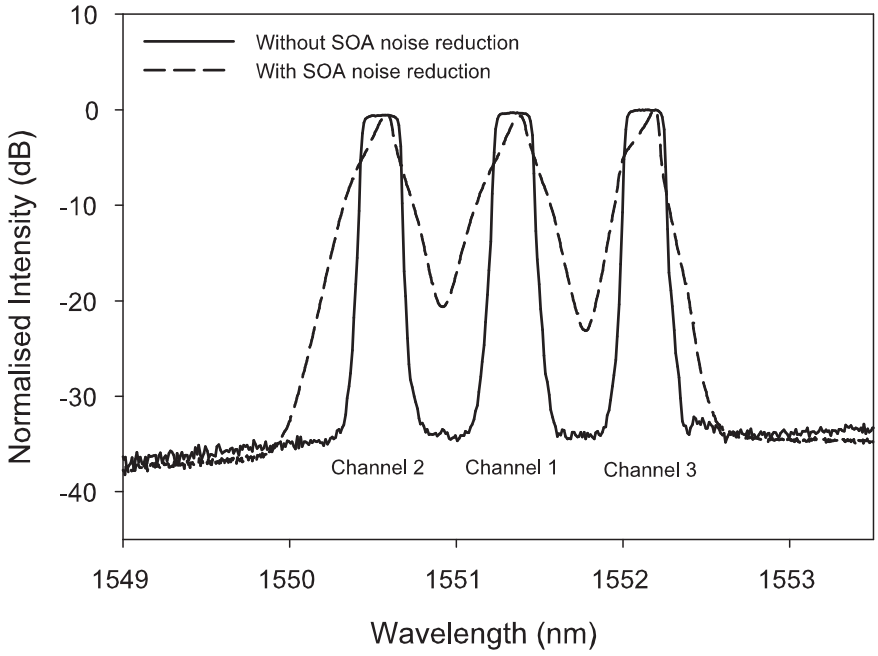

Figure 4.7: Receiver input spectra with and without SOA-based noise reduction.

system. Q measurements as a function of receiver filter bandwidth were performed for three different channel spacings of 0.6, 0.8 and 1.0 nm. Figure 4.7 shows the receiver input spectrum for the 0.8 nm (100 GHz) channel spacing configuration, with and without SOA-based noise reduction. It is clear that the presence of the saturated SOAs gives rise to noticeable overlap between adjacent channels. I also show the three channel spectra after receiver filtering (Figure 4.8) for a few selected optical filter bandwidths.

The measured system performance for all three channel spacings is given in Figure 4.9. Note that the receiver filter used in this experiment had good out-of-band extinction (typically > 30 dB, as visible in Figure 4.8), thus minimising the crosstalk from outside of the receiver filter passband. As is expected, the broader receiver filters allow more crosstalk from the adjacent channels. The dashed baseline also shown in the graph is the corresponding Q measurement for the single channel scenario, which represents the intensity noise limit for the system.

From Figure 4.9, the optimum channel bandwidth for the 0.6, 0.8 and 1.0 nm channel spacings are 0.7, 1.0 and 1.4 nm respectively. The system is intensity noise

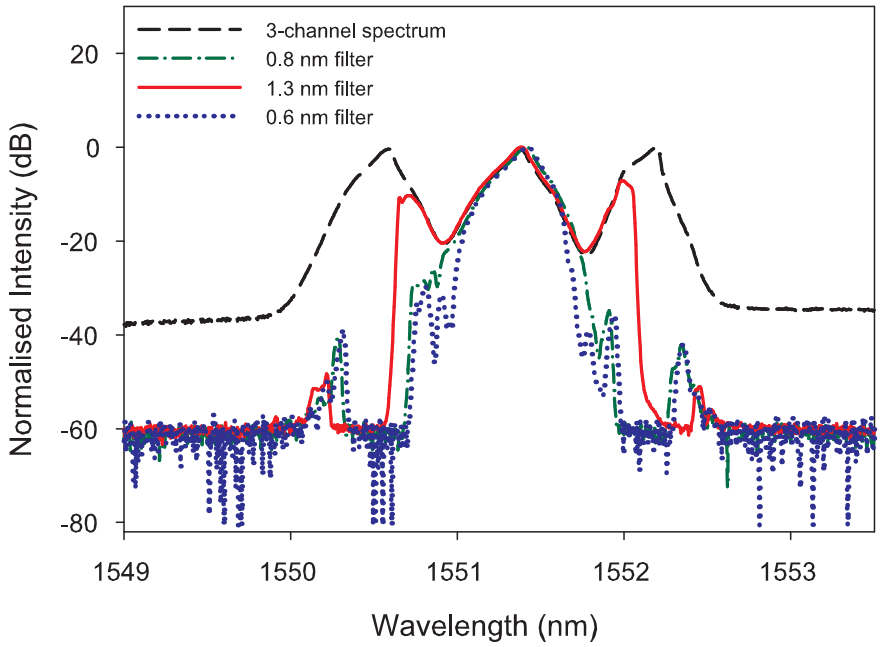

Figure 4.8: Three channel system output spectra for the 0.8 nm channel spacing scenario.

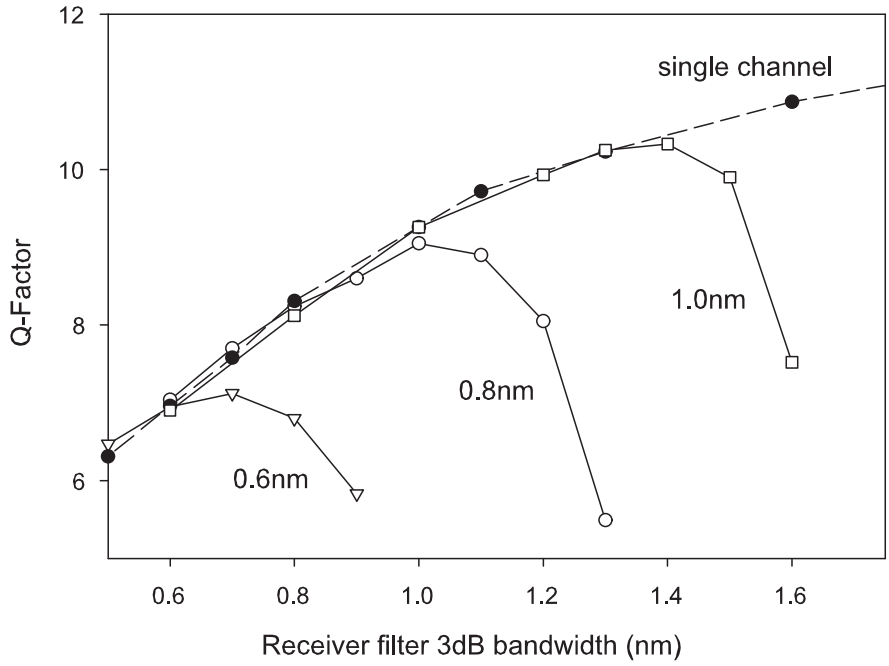

Figure 4.9: Three channel system Q measurement at 2.5 Gb/s and 0 dBm for varying filter widths and channel spacings of 0.6, 0.8, and 1.0 nm. Single channel measurements are shown as a baseline for the intensity noise limit of the system.

limited for bandwidths less than the optimum value, after which it becomes crosstalk limited. In each case, we find that the optimum receiver/demux filter bandwidth is greater than the channel spacing, which is in contrast to the system without SOA noise reduction, where the optimal receiver filter bandwidth is approximately half the channel spacing [47]. In systems using SOA-based noise suppression, receiver filtering results in a more dramatic increase in intensity noise in comparison with the thermal light case. This results in the optimum receiver bandwidth being shifted toward a higher level of adjacent channel overlap.

I would like to point out that the experimental setup was not optimised for low-cost, as my main objective was to investigate the filtering effects on the noise suppression of the SOA. A more cost effective system configuration is proposed in [10] which uses a monolithically integrated SOA array, followed by an arrayed waveguide grating.

4.2.2 Spectral Efficiency

The natural extension of the preceding study is to establish the optimum spectral efficiency (bits per second per unit bandwidth) that could be achieved for the 3-channel system discussed above, in view of the tradeoff between intensity noise and crosstalk effects. To this end, Q measurements were carried out for three other bit rates of 2.2 Gb/s, 622 Mb/s and 155 Mb/s. A similar trend to that seen in Figure 4.9 at 2.5 Gb/s was observed in these measurements. Optimum Q values are then extracted from these results, and are shown in Figure 4.10 as a function of bit rate and channel spacing. This can then be used to calculate the spectral efficiency of the system given the channel spacing and required system performance (Q in this case).

The results are given in Figure 4.11, for six different Q values of 7, 8, 9, 10, 12 and 15. A peak is observed in the spectral efficiency at a channel spacing of 0.7 nm, although the relative magnitude of this peak decreases for larger values of Q. This is attributed to the relationship between Q and useable bit rate where the maximum bit rate decreases as the required error probability decreases (i.e. as Q increases). As Q is increased, the maximum spectral efficiency converges for the different channel

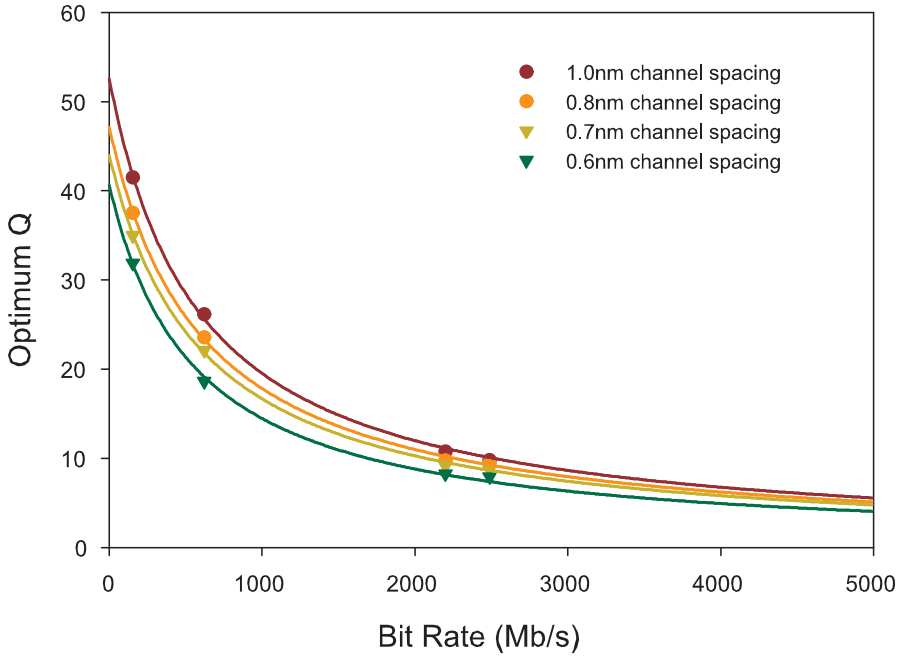

Figure 4.10: Optimum Q as a function of bit rate (2.5 Gb/s, 2.2 Gb/s, 622 Mb/s, 155 Mb/s) and channel spacing. Curve fitting uses the form $y = a/(b + x)$.

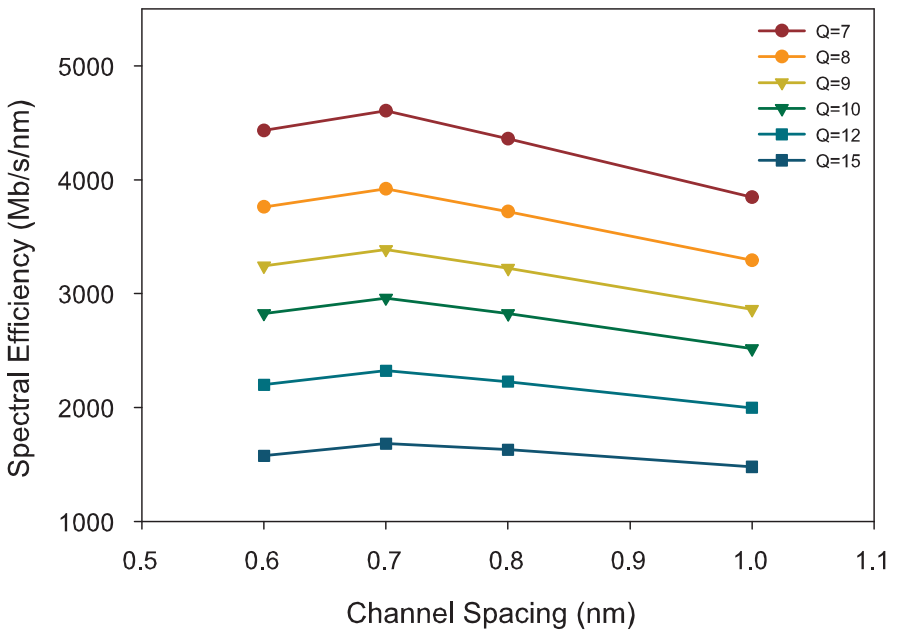

Figure 4.11: Spectral efficiency of the three-channel system for different values of Q.

spacings, resulting in a less significant peak. At Q=7 (BER $\approx 10^{-12}$) the peak spectral efficiency is ∼4.6 Gb/s/nm. Note that the number of channel spacings and usable bit rates for this experiment were limited by the tuning range of the gratings and the available optical receivers.

It would also be interesting to repeat this experiment for different input slice widths. Limitations in available filters did not allow for further characterisations at the time of this study. However, it is to be appreciated that the parameter space to determine an *optimum* slice width for *optimum* spectral efficiency is large, and that numerical simulations would be the more appropriate form of analysis. Also, as the slice width decreases, the intensity noise increases accordingly, resulting in larger phase noise and related spectral broadening at the SOA output. However, additional beat terms due to FWM will be reduced, as will be the impact of dispersion. Apart from the slice width/shape of the input filter, an optimum spectral efficiency analysis will also require that the bit-rate, channel spacing and optical receiver bandwidth be varied. It is also important to consider system limitations on the available power per channel. For the above experiment I used a power level of +5 dBm into each individual SOA, although for narrower slices this level of power would require a higher power narrow-band source. The implementation details and practicality of the system should therefore be considered in this analysis. Difference in SOA input power and therefore operating point, will also need to be factored into any simulations.

4.3 SOA for Noise Suppression and Modulation

One of the benefits of using an SOA in a spectrum-sliced system is that it can be used as both an amplifier and modulator, resulting in cost savings for access applications. Previous studies [10] have demonstrated the feasibility of this approach by using a saturated SOA to modulate a 0.6 nm spectrum-slice at 600 Mb/s, yielding a lower error floor than an electro-optic modulator (EOM) without noise suppression. However, to my knowledge, the noise suppression offered by a modulated SOA has not been previously compared with the noise performance in CW operation.

I have characterised the received signal quality when the SOA is used for simul-

taneous modulation and noise reduction. This is compared with the performance of the SOA/EOM combination, in order to assess the penalty, if any, imposed on the noise suppression performance by modulating the SOA.

4.3.1 Direct Modulation of the SOA

A commercial diode driver, Hytek model 6410, was used to modulate the drive current of the SOA (JDS model CQF872). The 6410 is an ECL coupled diode driver and allows the driving of a laser diode through a 50 Ω transmission line, without the need for matched impedance, using a patented back-matching technique [48]. The experimental setup is shown in Figure 4.12. In order to perform a fair comparison between operating the SOA in CW and pulsed mode, it was important to characterise the current through the SOA under different driver settings. The driver has two variable current sources which allow the bias and modulation currents through the device to be varied. The *bias* controls the RF output of the driver when the input logic level to the driver is a *zero*, while the *modulation* controls the RF output of the driver when the input logic level is a *one*. For a logic input level of one, the SOA should be driven as hard as possible, saturating it, in order to provide optimum noise reduction. The power to the driver, and the tunability of the bias and modulation settings are controlled using the circuit shown in Figure 4.13.

With the driver bias and modulation controls at their limit, and the pattern generator set to an all ones pattern, ∼1.55 V is measured across the diode. When the SOA is directly biased (i.e. without the driver), the power supply measures 380 mA for the same voltage across the diode. The SOA output spectrum for both scenarios (i.e. with and without driver) are given in Figure 4.14. The spectra match closely, indicating that for the highest settings of the bias and modulation controls, the driver provides a current of 380 mA into the SOA, for a logical input of 'one'. Also note that the voltage across the diode, and therefore the saturation level of the SOA, did not depend on the exact ECL level settings of the pattern generator (i.e. as long as the levels were in the ECL range, the diode voltage remained constant).

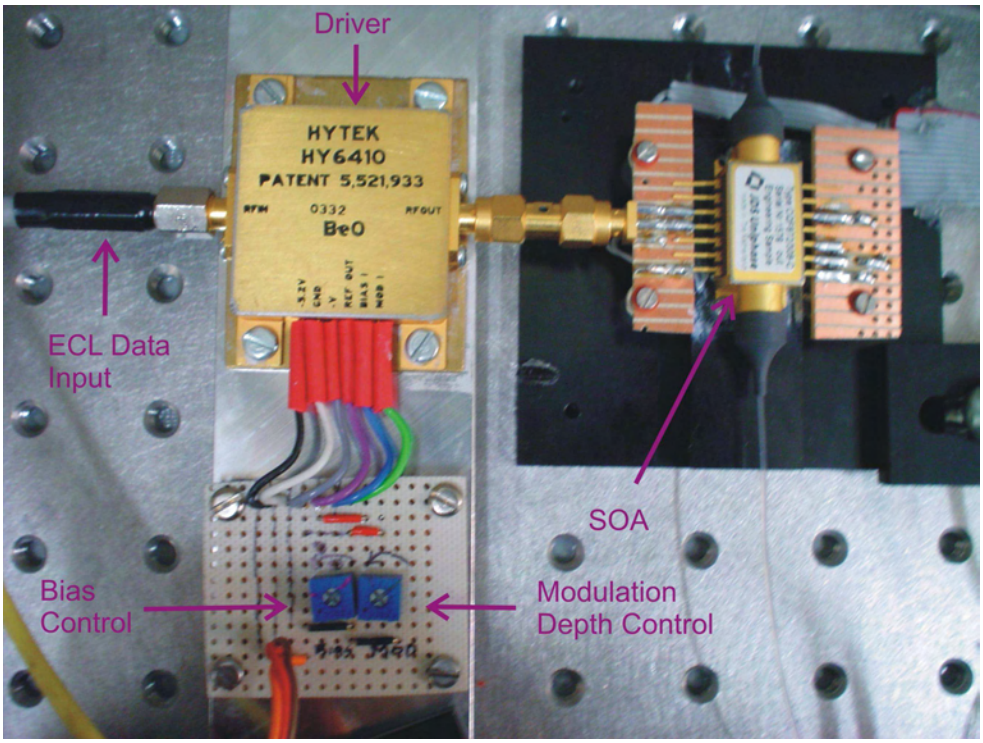

Figure 4.12: Driver and SOA

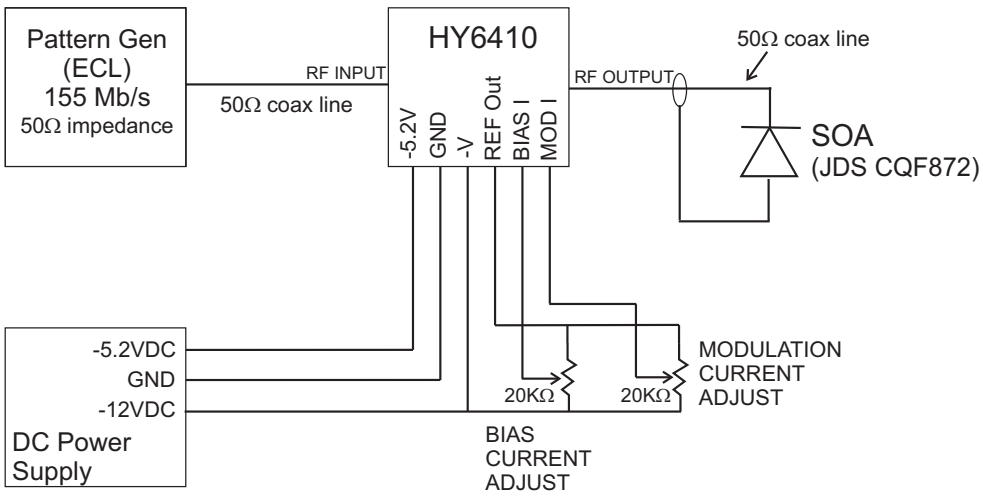

Figure 4.13: Hytek diode driver and JDS SOA electrical connections.

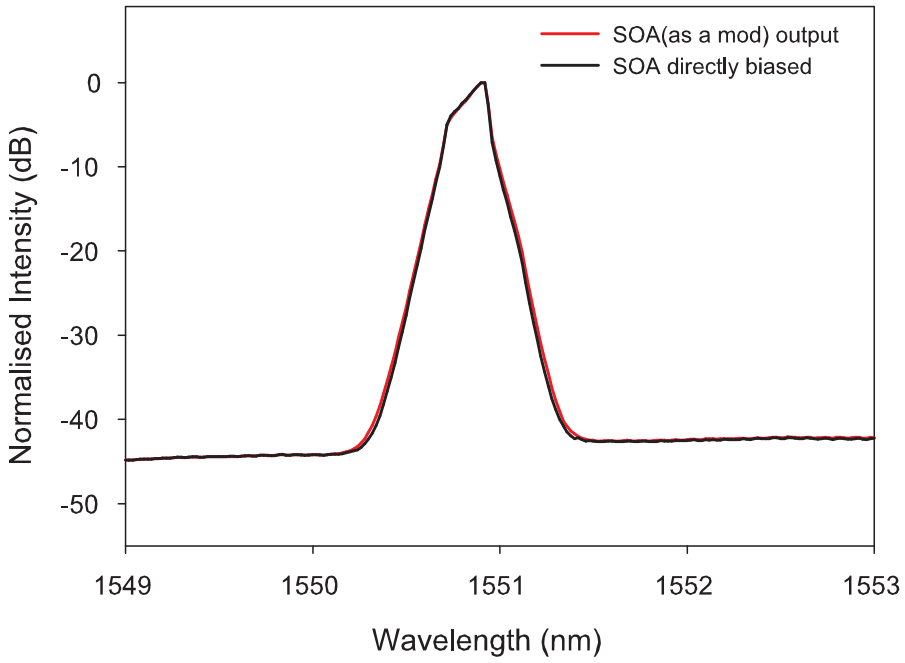

Figure 4.14: Optical spectra when using the SOA with the diode driver and when directly biasing the device at 380 mA. Input spectrum-slice is 0.24 nm.

4.3.2 System performance

Figures 4.15 and 4.16 show the experimental setups used to evaluate the system performance of the saturated SOA with and without direct modulation. The JDS SOA used in this characterisation did not include integrated isolators; thus an isolator was used at the input to the SOA to avoid lasing action due to any undesired reflections. Q measurements were performed at 155 Mb/s using a sampling oscilloscope and a 2.85 GHz receiver module. Direct modulation greater than 155 Mb/s was not possible due to the limited bandwidth of the diode driver.

The results of the two approaches are given in Figure 4.17. It was repeatedly observed that the modulated SOA performed slightly better than the SOA/EOM combination. By comparison, the Q for the system with no SOA is ~2.5, which clearly shows that both in CW and pulsed mode operation, the SOA provides substantial noise mitigation. The noise floor at the receiver is given in Figure 4.18, which displays a similar trend to the Q plots. It is to be appreciated, however, that a direct comparison between the noise floor measurements is difficult from these results

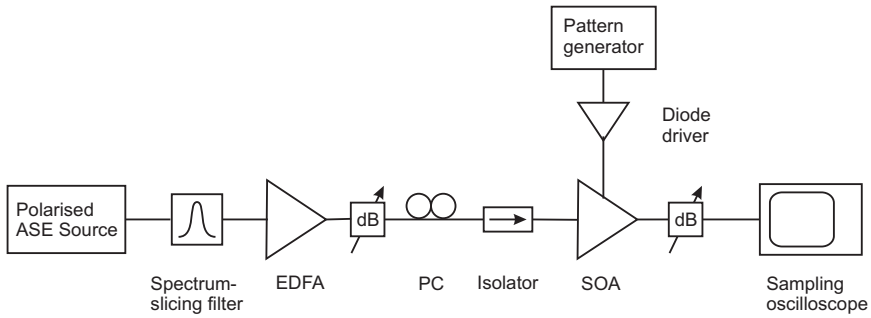

Figure 4.15: Experimental setup using the saturated SOA for simultaneous noise suppression and modulation.

.

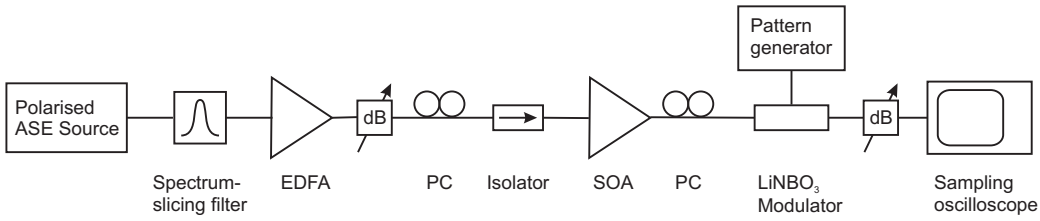

Figure 4.16: Experimental setup using the saturated SOA for noise suppression and a separate EOM for modulation.

alone. For an accurate comparison, the extinction of the modulators would need to be considered; the noise spectra were measured at the same average power, which is non-ideal when comparing different modulation methods. Note that this is in contrast to noise measurements presented in previous chapters that were performed on the CW signal. It is clear however that significant noise suppression is achieved when using the saturated SOA modulator.

The slight noise disadvantage of the EOM is attributed to the polarisation sensitivity of the external modulator, which degrades the noise suppression of the SOA by blocking the orthogonally polarised components of the ASE. This effect is visible in Figure 4.19, where the ASE level of the EOM output is ∼3 dB lower than that of the SOA output. The modification of the SOA output spectrum would of course result in an increase in intensity noise, as discussed previously. I also measured the degree of polarisation (DOP) at the modulator outputs using the Agilent 8509B lightwave polarisation analyser. A DOP of ∼80% was measured at the SOA modulator output, while this value rose to ∼92% when using the EOM. This higher degree of polarisation at the EOM output reinforces the supposition that the observed slight degradation

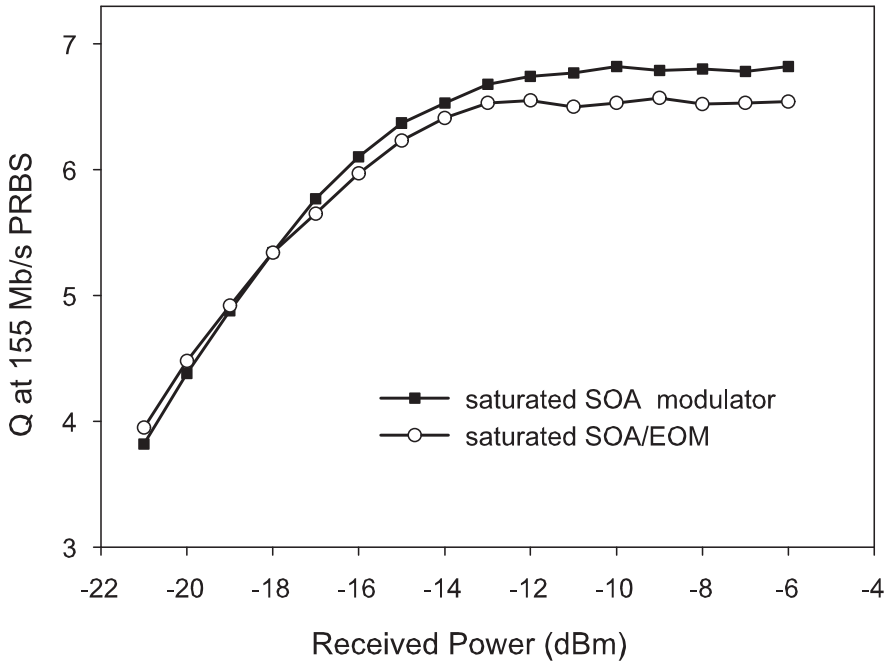

Figure 4.17: Q measurements at 155 Mb/s for the saturated SOA as a modulator and the saturated SOA with the EOM. Q for the SOA input was ∼2.5.

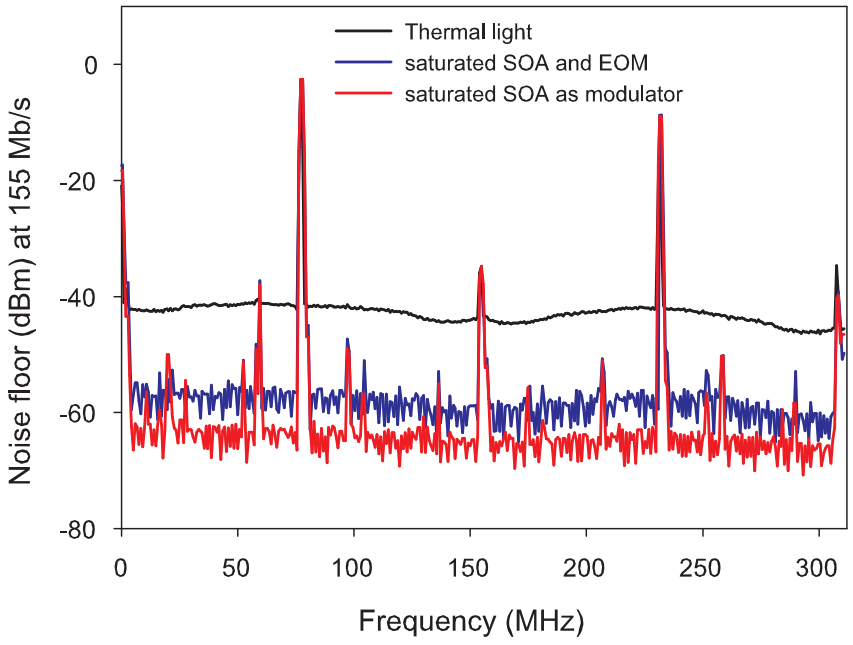

Figure 4.18: Noise floor at 155 Mb/s. The noise marker was placed at 110 MHz on the floor of the electrical spectrum, between data harmonics, for a repeating 2 bit data pattern, 1,0 at 155 Mb/s.

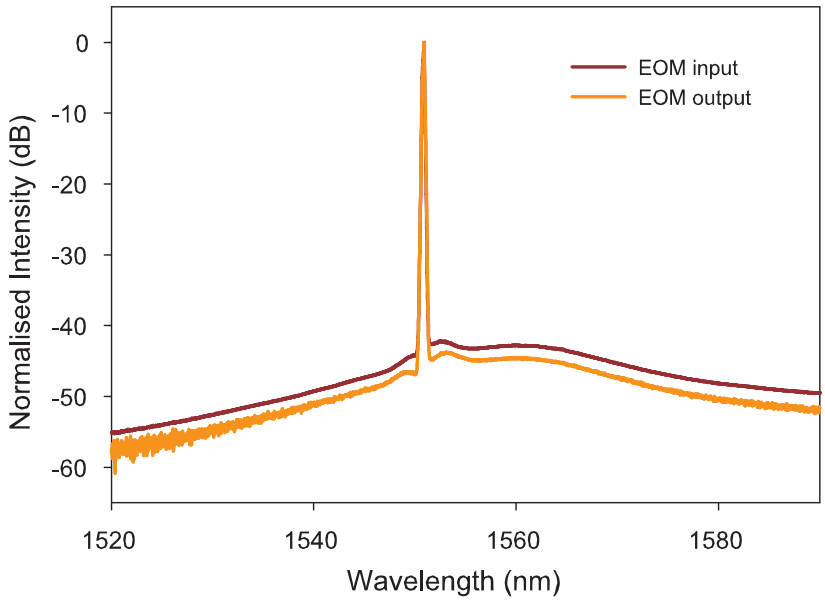

Figure 4.19: EOM input and output optical spectra.

in signal quality is due to the cross-polarised ASE filtering effects. However, using an optimised receiver with added electrical filtering will improve the received signal quality giving advantage to the higher extinction ratio of the EOM (The extinction ratio of the EOM used in this experiment is ∼3dB greater than that of the SOA; the EOM recorded an extinction of ∼16 dB). The $LiNbO_3$ modulator is also expected to provide better performance than the SOA at bit rates exceeding several GHz, due to the limited switching time of the amplifier. Nevertheless in cost-sensitive lower bit rate applications such as access networks, the saturated SOA modulator is an attractive choice.

I also measured the system Q with unpolarised light into the SOA modulator, and found that it resulted in the best overall performance, with a peak Q of ∼8.5. Due to the polarisation sensitivity of the EOM and, in fact, the SOA, the characterisations presented thus far in this thesis have been performed with polarised thermal light. For unpolarised light the intensity noise input to the SOA is 3 dB less than for the equivalent case of polarised light. As a consequence, the nonlinear processing that occurs within the saturated SOA should also be different. An obvious extension of my work is thus to better understand the reasons for the noted performance increase when using an unpolarised input to the SOA. In addition to eliminating the source

polariser, the observed benefit in performance is a distinct advantage of using the SOA modulator for metro/access network applications.

4.4 Comparative Study

4.4.1 Introducing the SOA at the Receiver

While the main focus of this thesis has been on using the SOA to reduce the noise of the CW signal before modulation, similar techniques have been proposed using the saturated amplifier at the receiver to suppress the noise of the modulated signal. Incorporating SOA-based noise suppression at the receiver is an attractive alternative that avoids the negative effects of post-SOA filtering. The SOA can also act as a preamplifier, increasing the overall sensitivity of the receiver unit. However, when used to amplify a modulated bit stream, the saturated SOA introduces *patterning*, which distorts the input signal and degrades the overall system performance [1].

Patterning is the result of the non-ideal gain dynamics of the saturated amplifier, and manifests itself most notably when a random sequence of 1 and 0 bits are launched into the device. Ideally, when the input is '1', the gain is low, while the gain recovers to its unsaturated value, for an input level of '0'. However if the gain compression and recovery are non-instantaneous, the initial gain experienced by each pulse is dependent on the preceding bit [1], and distortion occurs as illustrated in the eye diagram below. Although the patterning effects can be reduced by operating the amplifier at a lower saturation level, this also diminishes the effectiveness of the noise suppression process.

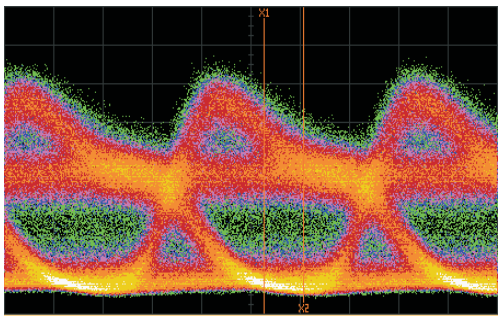

Figure 4.20: Illustration of patterning effects in a deeply saturated SOA at a bit rate of 2.5 Gb/s. Input to the SOA is 0.24 nm spectrum-sliced light.

In [49], Kim et al. show that optically pumping the SOA by injecting broadband incoherent light reduces eye distortion due to patterning while retaining good noise suppression. Using this technique a 0.5 nm bandwidth spectrum-slice was transmitted at 2.5 Gb/s over 20 km of SMF, showing significant improvement over the standard spectrum-slicing approach with no SOA preamplifier. However, the inclusion of an optical pump source, albeit low cost, does add to the complexity of the receiver.

Another technique, proposed by Yamatoya [50], uses the gain modulation of a saturated SOA to transfer the modulated data from the input spectrum slice to the backward-propagating ASE, thus avoiding the patterning effects which occur in the amplified forward-propagating signal. In addition to suppressing intensity noise, the SOA acts as an inverting preamplifier, thus increasing the overall receiver sensitivity. Using this approach, intensity noise reduction and receiver sensitivity improvements were demonstrated at 1 Gb/s with a slice width of 0.6 nm. It is also to be appreciated that a single-port amplifier is sufficient for this application, thus simplifying device packaging, and providing a clear economic advantage in metro/access applications.

Cross gain modulation (XGM) within the SOA can also be used to transfer the data to a *coherent* carrier signal. Using this approach, a 1.2 nm spectrum slice was coupled to a counter-propagating beam from a DFB laser diode, achieving error free transmission at 2.5 Gb/s [51]. Although this technique suffers from the added cost of a laser source at the receiver, it provides the additional capability to implement wavelength-routing, for interconnection with WDM-based trunk networks.

4.4.2 Performance Comparison

In this section I compare the noise suppression performance of the two incoherent approaches discussed above, by Yamatoya et al. and Kim et al. with that provided by using the SOA at the transmitter, before modulation. To my knowledge, this is the first reported performance comparison of the different SOA-based noise suppression techniques.

The experimental setup used for the ASE injection technique is given in Figure 4.21. In order to determine the SOA operating point for best noise suppression and system performance, the eye quality was characterised (in terms of Q) as a func-

tion of SOA drive current, input power, and ASE injection power. Based on these measurements, an average input power of ∼0 dBm, a drive current of 200 mA and an ASE injection power of ∼-2 dBm were chosen as the optimum operating point. Note that the polarisation into the SOA was optimised for each measurement.

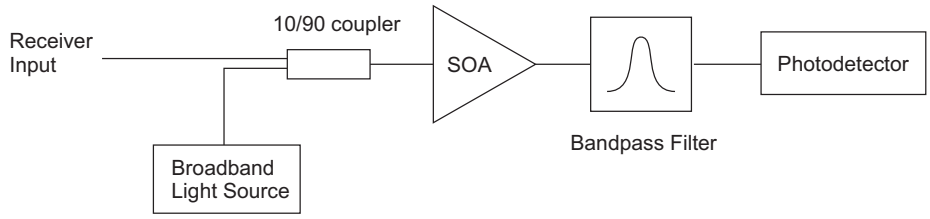

Figure 4.21: Receiver incorporating SOA and broadband light injection.

The ASE modulation technique was characterised using the experimental setup shown in Figure 4.22, and the optimum operating point was determined to be ∼0 dBm input power, with a drive current of 200 mA. In this configuration, the system performance was seen to be unaffected by changes in the polarisation state of the input spectrum slice.

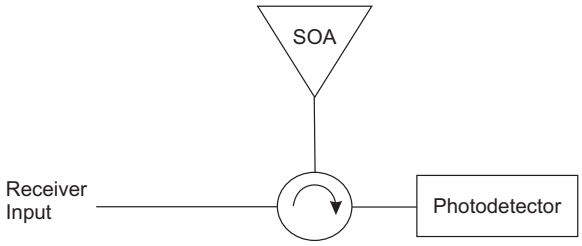

Figure 4.22: Receiver incorporating inverted ASE of SOA

System Q measurements for the three noise suppression techniques are shown in Figure 4.23. For comparison purposes, Q measurements with no SOA are also presented. All measurements were made at 2.5 Gb/s, using a 0.24 nm spectrum slice as the input to the SOA. Representative eye diagrams are given in Figure 4.24.

In the back-to-back configuration, the SOA at the transmitter clearly provides the best noise suppression, followed by the ASE modulation and ASE injection techniques respectively. However, it is important to point out that back-to-back measurements are not representative of real system performance when the SOA is used at the transmitter, as they ignore the effects of dispersion and post-SOA filtering. For example,

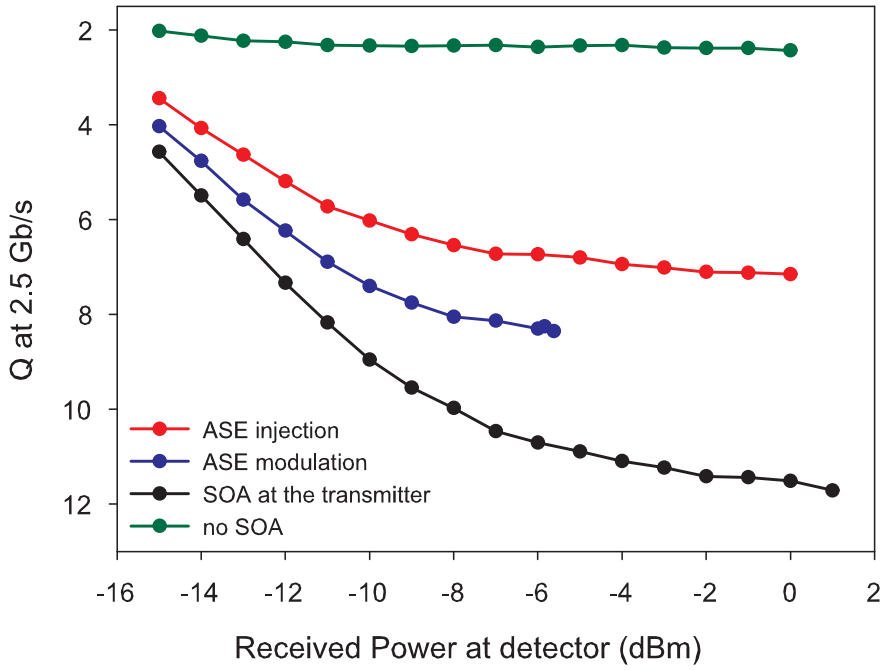

Figure 4.23: Q measurements for different SOA based noise reduction techniques.

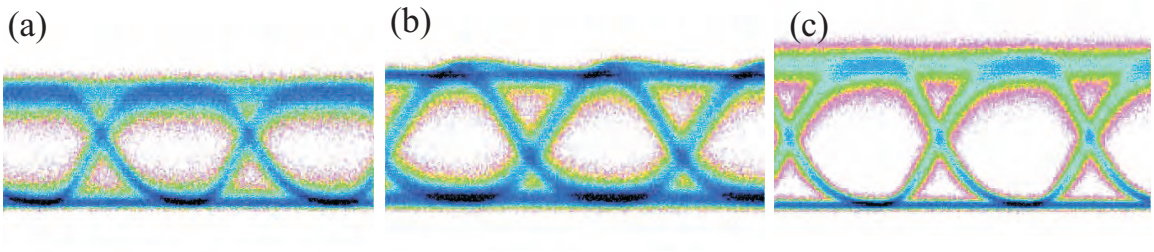

Figure 4.24: Eye diagrams for (a) ASE injection (b) ASE modulation (c) SOA at the transmitter.

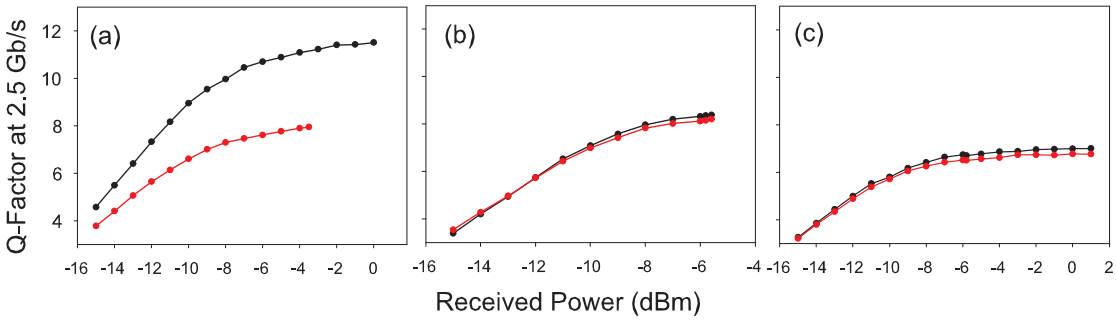

Figure 4.25: Back-to-back and dispersion measurement comparison for (a) SOA at the transmitter technique (b) ASE modulation (c) ASE injection. Black: back-to-back, Red: with 15 km of fibre.

recall that using a 0.8 nm optical receiver filter degrades the system Q to approximately ∼8.2 (Section 4.2), making it comparable to the performance of the ASE modulation technique. As discussed in Section 3.4.3, dispersion introduced after the SOA also causes an increase in the signal noise. Thus, unlike the ASE injection and ASE modulation techniques, the system using the SOA at the transmitter experiences a dispersion penalty beyond that resulting from pulse broadening.

In order to illustrate the effects of dispersion, the system Q measurements were repeated with 15 km of standard SMF (Corning SMF-28) inserted after the modulator. The results are summarised in Figure 4.25. For a length of 15 km, the group delay experienced by a slice of width 0.24 nm is ∼61 ps, resulting in a pulse broadening of ∼15% for a 400 ps (bit period at 2.5 Gb/s) data bit. Thus, as we would expect, the system configurations with the SOA at the receiver are nearly unaffected by dispersion, due to the very limited pulse broadening. On the other hand, the SOA at the transmitter suffers a distinct performance penalty as a result of the signal degradation due to the non-thermal aspects of post-SOA light. The ASE modulation technique is perhaps more suitable where relative immunity to spectral filtering and dispersion effects outweigh the comparative disadvantage in total noise suppression. A summary of the different techniques is given in Table 4.1.

Despite the drawbacks associated with using the SOA at the transmitter, as demonstrated in Section 3.4.3, dispersion compensation can be used to overcome the increased noise penalty. Additionally as discussed in Section 3.6.2, post-SOA spectral

Table 4.1: Summary of SOA-based noise suppression techniques

Technique	Benefits	Drawbacks
SOA at the transmitter	Superior noise suppression, simultaneous noise suppression/ modulation/amplification. Monolithic integration of source and SOA array onto single chip for use at head-end.	Signal degradation caused by post-SOA filtering effects and dispersion.
ASE injection	Good noise suppression, Increased sensitivity at receiver due to SOA preamplifier, Monolithic integration of SOA and receiver for use at subscriber nodes.	Cannot use SOA as a modulator, Additional source and filter required at receiver.
ASE modulation	Excellent noise suppression, Increased sensitivity at receiver due to SOA preamplifier, Monolithic integration of SOA and receiver for use at subscriber nodes. Reduced packaging cost for discrete SOA due to single port operation.	Cannot use SOA as a modulator.

filtering effects can also be considerably reduced by optimised device design, giving advantage to the superior noise suppression benefit of the approach. An optimised SOA structure, together with its advantage as a modulator and booster amplifier, has potential in delivering superior performance at reasonable cost for applications in metro and access networks.

4.5 Summary and Discussion

I have experimentally characterised the spectral filtering effects on the system performance in a spectrum-sliced WDM system using SOA-based noise reduction. Spectral broadening produced by the saturated SOA is prominent with steep, narrow input spectral slices and filtering of this broadened output degrades the signal quality, reducing the noise suppression benefits of the SOA. However, optical filtering is required at the receiver to minimise channel crosstalk, thus imposing a tradeoff between crosstalk and intensity noise. I have experimentally determined the optimal receiver bandwidth in a three channel spectrum-sliced system for three different channel spacing configurations. It was found that the optimum receiver bandwidth was wider than the chosen channel spacings due to the substantial signal degradation caused by spectral filtering of the saturated SOA output. This study clearly demonstrates the need to consider the effects of channel and receiver filter shape/width in the design of high channel count spectrum-sliced systems employing SOA-based noise reduction. I further quantified the spectral efficiency of the system for different channel spacings and observed a peak in the spectral efficiency at $\sim$4.6 Gb/s/nm for a channel spacing of 0.7 nm.

I have also experimentally assessed the potential of the saturated SOA for simultaneous noise suppression and modulation. My measurements showed no penalty in the noise suppression performance when operating the amplifier in pulsed mode. In fact, a slight benefit in signal quality was observed over the SOA/external modulator scenario, and is attributed to the polarisation sensitivity of the EOM.

A comparative study was also performed to assess the advantages and disadvantages of the different SOA-based noise reduction configurations, identified in this chapter as *SOA at the transmitter*, *ASE injection* and *ASE modulation*. The highest back-to-back system performance was achieved when using the SOA at the transmitter, although post-SOA spectral filtering and dispersion pose challenges to the practical implementation of the approach. However as I have discussed, it is possible to overcome these challenges using dispersion compensation schemes and optimised SOA designs. The simplicity and effectiveness of using the SOA for simultaneous noise suppression, modulation and amplification, renders it an attractive choice for

cost-sensitive spectrum-slicing applications.

Chapter 5

OCDMA Applications

Overview: In this chapter I introduce spectral amplitude coded OCDMA techniques and examine the effectiveness of SOA-based noise reduction in such systems. Experimental results are presented for three different two-channel system configurations, using custom FBGs to perform the encoding and decoding functions. These results demonstrate the effects of post-SOA filtering, and motivated the detailed investigations presented in Chapters 3 and 4. System and grating design optimisations were investigated to minimise the adverse effects of spectral decoding. I conclude by discussing the feasibility of this technique for low-cost applications.

5.1 Background

OCDMA is based on *spread-spectrum*; a technique that has found widespread use in digital cellular communications [52]. As its name implies, spread spectrum is a method of transmitting data over a much larger bandwidth than required by the message signal. This concept is illustrated graphically in Figure 5.1. The spreading is accomplished by combining the user data with a pseudorandom spreading signal or *code*. At the receiver, this spread signal is correlated with a synchronised copy of the code used in transmission, which results in despreading, or recovering of the original information signal [53].

This approach can be extended to create a multi-user environment, known as code division multiple access (CDMA) [54], by using a unique spreading code for each

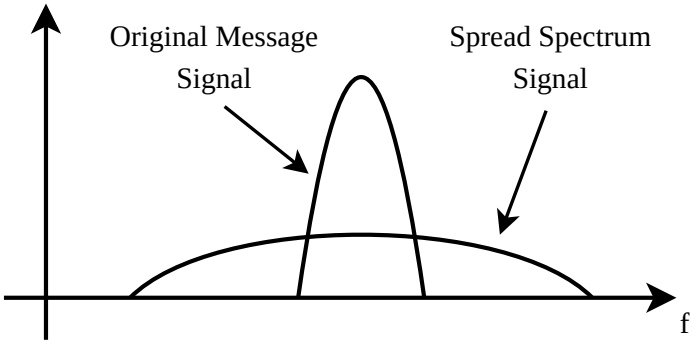

Figure 5.1: Spread spectrum principle

channel. Each spreading code is designed to produce a distinct autocorrelation signal while minimising the cross-correlation with the other channel codes. All channels share the same frequency bandwidth but can be distinguished by their individual spreading codes. The CDMA receiver calculates the correlation between the received signal and the desired channel code. Since the autocorrelation is much higher than the cross-correlation, the desired signal can be reconstructed, while any signal that does not match the desired code will appear as low level background noise.

The techniques used in radio frequency (RF) CDMA can be categorised as direct sequence CDMA (DS-CDMA), frequency hopping CDMA (FH-CDMA), or time hopping CDMA (TH-CDMA), according to the method of imprinting the code sequence onto the transmitted data. In DS-CDMA, the data modulated carrier signal is subjected to pseudorandom phase jumps, as specified by the user code sequence. The code phase transitions are applied at a much higher rate than the data, resulting in multiple phase transitions in each bit period. The interval between the phase jumps (within a bit period) is referred to as a chip. FH-CDMA is similar except that the code sequence specifies transitions in carrier frequency, rather than phase. Thus each chip is transmitted on a different carrier frequency. In TH-CDMA, a time interval (much larger than the bit period) is divided into multiple chips, where each chip is smaller than a bit period. The chips representing each bit are transmitted in bursts according to the user code sequence. One can think of it as a generalised form of time division multiple access (TDMA) where the assignment of time slots to users is determined by the code sequence. Various hybrids of these CDMA techniques have also been developed [54].

As mentioned above, the autocorrelation and crosscorrelation properties are key attributes of the CDMA code. The crosscorrelation of two sequences, $X = \{x_1, x_2, ..., x_N\}$ and $Y = \{y_1, y_2, ..., y_N\}$, can be given as $\Theta_{XY}(k) = \sum_{i=1}^{N} x_i y_{i+k}$. When $X = Y$, we have $\Theta_{XX}(k) = \Theta_X(k) = \sum_{i=1}^{N} x_i x_{i+k}$ which is the autocorrelation of sequence X [55]. Ideal characteristics of code sequences for use in CDMA can be defined in terms of their autocorrelation and crosscorrelation functions. For each user code X, the peak of the autocorrelation function, $\Theta_X(0)$, should be maximised and the side lobes, $\Theta_X(k), k \neq 0$, should be minimised. Additionally, the crosscorrelation $\Theta_{XY}(k)$ for all pairs of code sequences should be minimised for all values of k [56]. Some of the coding schemes that are currently in use in RF-CDMA are m-sequences and combinations of m-sequences such as Gold codes, Kassami codes and Walsh-Hadamard codes [57].

Spreading the message signal over a large bandwidth makes spread spectrum communications relatively immune to interference (including intentional jamming) and also protects the signal from potential eavesdroppers [58]. This security and resistance to interference, together with its inherent spectral efficiency has made RF-CDMA a popular choice for satellite and cellular communications. These advantages and successes have aroused interest in applying the same techniques to fibre optic communications. However, fundamental differences between the two media prevent the direct application of RF-CDMA techniques in fibre [59].

One of the primary differences between optical and RF/microwave communications is the manner in which the received signal is detected. Photoreceivers, which are optical-to-electrical (O/E) converters, detect the power (intensity) of the incoming signal as opposed to the amplitude of the electric field as do antennas in RF communications. In a typical optical CDMA receiver, the incoming optical signal maybe subjected to either coherent or incoherent processing. This processing which occurs before the O/E conversion depends on the encoding mechanism used. Coherent detection OCDMA techniques are based on using interference of the incoming optical signals to convert electric field values into intensity variations that can then be detected by the photoreceivers [60]. Thus it enables cancellation of undesired user channels through destructive interference. Coherent detection allows bipolar codes

($-1/1$ code sequences) used in RF-CDMA to be used, but optical implementations have required either expensive or complicated systems [61].

In contrast, incoherent detection OCDMA systems detect the signal directly without using interference, and thus the detected signal is simply the sum of the incoming signal intensities. As optical intensity is a non-negative value, coding is limited to unipolar schemes ($0/1$ code sequences), which do not support perfect cancellation between interfering channels. However, schemes using balanced detection have been proposed to overcome this limitation [62]. The incoherent nature of the processing also enables the use of inexpensive broadband sources such as LEDs or ASE sources, which is an attractive option for metropolitan/access networks. OCDMA systems based on incoherent broadband light sources have the potential to provide the required network management flexibility and channel count for metro/access applications while reducing overall system cost. Incoherent sources also provide reduced sensitivity to both environmental changes and polarisation.

Nonetheless, excess photon noise arising from the incoherent nature of the source remains to date, a major limiting factor in OCDMA applications employing incoherent sources. As we have seen in the preceding chapter, in the area of WDM spectral-slicing, a number of schemes have been investigated in order to suppress this noise. It is of interest to extend these noise reduction schemes to the OCDMA arena, as they could potentially result in significant performance improvements in current techniques.

Since the initial proposals in the late 1970s [63], numerous variations of OCDMA have been proposed and investigated. Categorising the various OCDMA techniques can be complicated due to the many different criteria that can be used as a basis of organisation. Some examples are coherent vs. incoherent processing, coherent vs. incoherent sources, encoding/spreading technology, and code sequence. A possible categorisation of the numerous techniques is given in Figure 5.2. The focus for my work has been spectral amplitude coding (SAC) using incoherent light, and in the following section I give an overview of this approach, in order to set the context for this study.

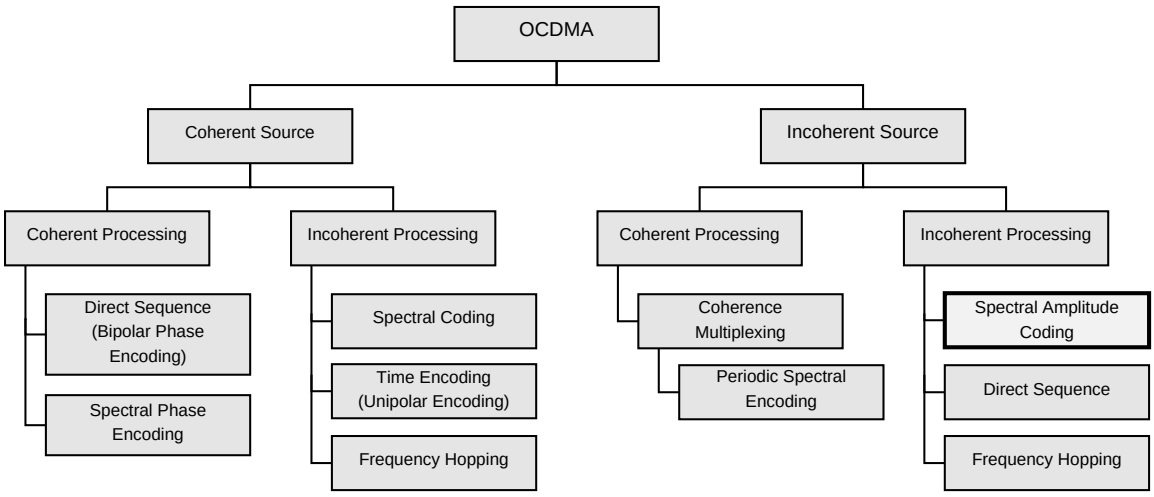

Figure 5.2: The different OCDMA techniques based on the type of source and the type of processing used.

5.2 Spectral Amplitude Coding

5.2.1 Overview

In spectral amplitude coding (also known as frequency-encoded CDMA) the available optical source spectrum is divided into multiple spectral-slices (chips) that are then used to form a given user code spectrum $A(\nu)$. As shown in Figure 5.3, various codes will be formed spectrally by the presence (on) or absence (off) of a spectral-slice.

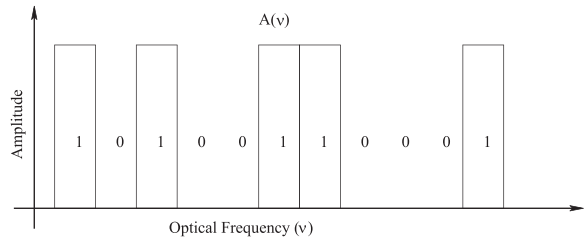

Figure 5.3: Example of a spectral code sequence

In this technique, the data is modulated onto the broadband optical carrier signal which is then encoded using a filter frequency response such as that given above, and transmitted along with other encoded data signals. All channels occupy the same spectral bandwidth. A filter with a matched code is used at each receiver to recover the original message. At the receiver, the input signal is split in two paths; one path is correlated with the matched code X, while the other path is correlated with the

complementary code $\bar{X}$. The signals after correlation are then sent into a balanced differential receiver, which outputs the difference between the two signals. When the received signal is that of the desired channel, the differential receiver output will be high, while when the received signal is that of an undesired channel, the output will be zero. Figure 5.4 shows a conceptual block diagram of a SAC receiver.

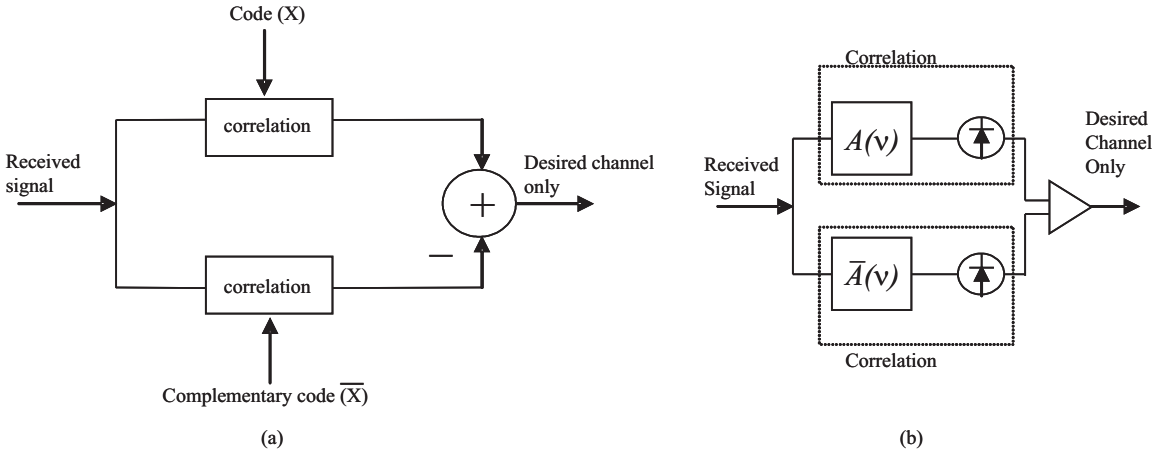

Figure 5.4: (a) Conceptual block diagram of receiver for spectral amplitude coding OCDMA (b) Actual implementation of receiver

A unipolar $(0, 1)$ code sequence that permits complete cancellation of multiple user interference can be specified as follows [64]:

i. For every pair of code words $X = \{x_1, x_2, ..., x_N\}$ and $Y = \{y_1, y_2, ..., y_N\}$, we have the crosscorrelation $\Theta_{XY}(k) = \sum_{i=1}^{N} x_i y_{i+k}$.
ii. Define the complement of X by $\bar{X} = 1 - \{x_1, x_2, ..., x_N\}$. For code words $\bar{X}$ and Y we have the crosscorrelation $\Theta_{\bar{X}Y}(k) = \sum_{i=1}^{N} \bar{x}_i y_{i+k}$.
iii. Choose code sequences that satisfy $\Theta_{XY}(k) = \Theta_{\bar{X}Y}(k)$.
iv. A receiver that computes $\Theta_{XY}(k) - \Theta_{\bar{X}Y}(k)$ will reject interference from user Y.

A more general case for choosing appropriate code schemes is given in [65]. As is apparent from the above analysis, in the ideal case, spectral amplitude coding avoids the limitations of unipolar coding while maintaining a lower level of complexity than analogous systems using coherent detection [66].

5.2.2 Implementation and Literature Review

Initial attempts to implement this method used a diffraction grating based filter for spectral encoding of the optical source bandwidth [62, 64]. The grating based filter apparatus was originally developed for short pulse shaping [60] and is shown in Figure 5.5.

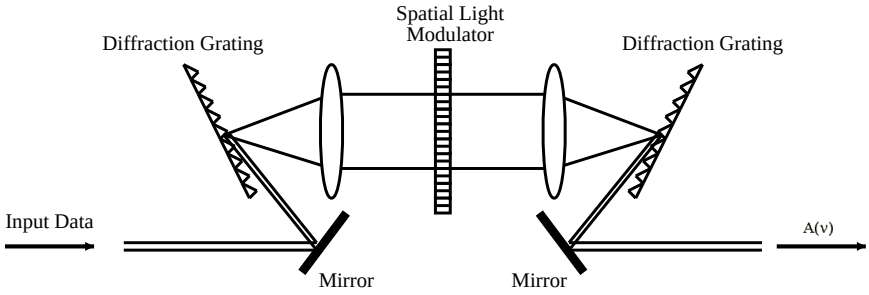

Figure 5.5: Temporally non-dispersive lens and grating apparatus

The input signal is reflected from the first grating where the different wavelengths are spatially dispersed and focused onto the spatial light amplitude modulator. The spatial light modulator imprints the desired code sequence on the input spectrum, by turning *on* and *off* different spectrum slices. A second lens and grating are used to recombine the spatially dispersed light signal and refocus a single optical beam back into the fibre. The proposed OCDMA system using this filter [62] is shown in Figure 5.6.

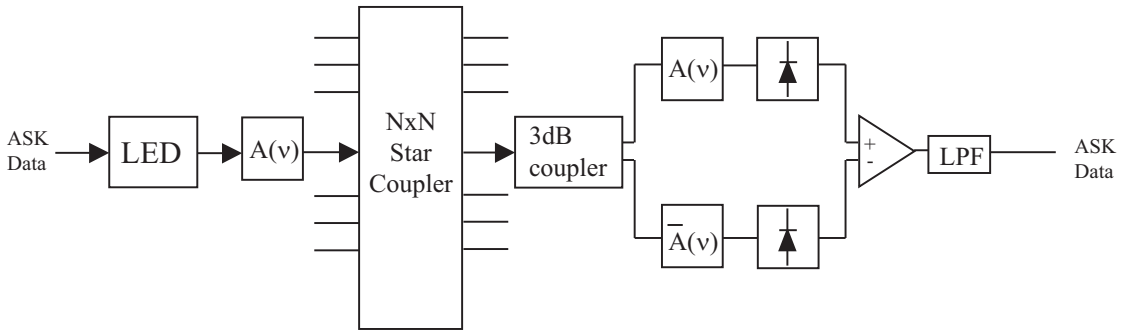

Figure 5.6: Proposed OCDMA system by Zaccarin and Kavehrad.

Unipolar m-sequences were used by Zaccarin and Kavehrad and were theoretically found to give good BER results for a system with ∼100 users, a code length of 511 and a bit rate of 500 Mb/s per user. The number of 'non-overlapping' slices/chips

that can be imprinted on to the given source spectrum dictates the length of the code sequence and thus in turn the total number of system users. Note that the desired signal is detected only in the $A(\nu)$ arm of the receiver, resulting in an inherent 3 dB splitting loss. This can be avoided by replacing amplitude shift keying (ASK) with orthogonal signaling, where each *1* bit is encoded with $A(\nu)$, while each *0* bit is encoded using $\bar{A}(\nu)$. Hadamard codes can be used in the orthogonal case, as, in addition to the correlation properties mentioned earlier, these codes have the added property of $\Theta_{XY}(k) = \Theta_{\bar{X}Y}(k)$.

This approach has also been extended to a more general class of code sequences [65]. In the general case, in place of the requirement $\Theta_{XY}(k) = \Theta_{\bar{X}Y}(k)$, the less restrictive condition $\Theta_{XY}(k) = \alpha\Theta_{\bar{X}Y}(k)$ is introduced. Here, α is a parameter that relates the individual code weight w (i.e. the number of 1's in the sequence) to the crosscorrelation, C, between each pair of code words. Note that all the code words should have the same weight w and that the crosscorrelation C is a system constant.

More recently, in an attempt to reduce the complexity of the encoding/decoding structures, spectral amplitude coding systems based on FBGs have been proposed [67, 68]. The FBG based encoder structure is shown in Figure 5.7.

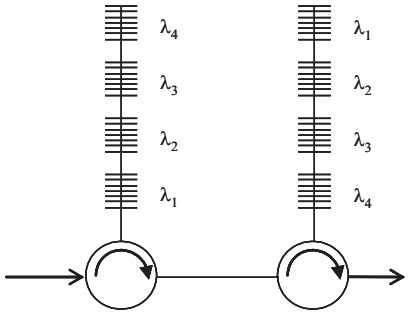

Figure 5.7: Encoder using fibre Bragg gratings for use in spectral amplitude coded OCDMA

The initial Bragg grating array is used as a reflection filter with a frequency response $A(\nu)$, and is used to encode the sequence X onto the modulated input optical source spectrum. Due to the cascaded nature of the gratings in the array, an incoming input pulse will experience different delays for the different frequency chips in the grating array thus leading to temporal dispersion of the input data pulse. The second Bragg grating array in the encoder is the spatially reversed copy of the first

grating structure, and equalises the total round trip time seen by the spread pulse, thus removing the dispersion introduced by the first FBG. The decoder structure used in this proposed system is shown in Figure 5.8.

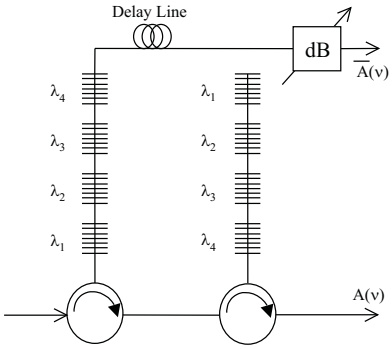

Figure 5.8: Decoder structure for use with spectral amplitude coding

As in the case of the encoding filter, the reflected output from the second Bragg grating of the decoder gives $A(\nu)$. The transmission spectrum of an FBG is the complement of its reflection spectrum, and thus the transmission output of the first grating will have a spectrum of $\bar{A}(\nu)$. Using the transmitted output of the FBG in this way also eliminates the 3 dB coupling loss that is present in the previous implementation (see Figure 5.6). The delay line balances the path length of the two branches of the receiver. The attenuator is used to compensate for the difference α, between $\Theta_{XY}(k)$ and $\Theta_{\bar{X}Y}(k)$ (recall that $\Theta_{XY}(k) = \alpha\Theta_{\bar{X}Y}(k)$), as well as the insertion loss of the second Bragg grating.

An experimental demonstration of a SAC system based on incoherent sources and cascaded discrete FBGs has been presented by Magel et al. [69]. In this experiment, the FBG arrays were used in transmission mode, thus avoiding the circulator loss at the encoder. The various user spectral codes were generated using Walsh-Hadamard code sequences while forward error correction (FEC) was used to enhance system performance. The performance of 15-channel and 8-channel systems operating at 155 Mb/s and 622 Mb/s respectively is reported with BER less than 10^{-12}.

5.3 Employing SOA-Based Noise Suppression

In the following sections I present the results of my work on the use of a gain-saturated SOA to enhance the performance of SAC systems, which is to my knowledge the first reported study in this area. Beat noise suppression is a significant advantage in OCDMA systems, allowing for larger numbers of allocated user codes.

This research formed the basis of my initial Ph.D. project work, and also resulted in my first encounters with the unusual post-SOA filtering effects introduced in Chapter 3. It is clear from prior chapters that despite the significant noise reduction benefit of the SOA, the technique has limitations due to the increase in intensity noise caused by spectral filtering at the receiver. Spectral decoding is, however, an unavoidable part of SAC, and thus imposes clear challenges to the incorporation of SOA-based noise reduction in OCDMA applications. This chapter addresses the performance limits of the approach, while investigating potential methods of minimising system penalty. It is to be appreciated however, that the following sections document the chronological progress of my initial research, the bulk of which was performed without the understanding, gained in hind-sight, of the properties of intensity smoothed SOA output light.

5.3.1 SOA Per Channel

The initial system configuration employed for this work was based on [62, 64] and employs FBGs to perform the encoding and decoding operations as proposed in [67]. However unlike in [62], the encoding is performed prior to data modulation, avoiding the dispersive effects of the cascaded grating array and eliminating the requirement for a second FBG at the transmitter. However, two FBGs are required at the decoder and are used in conjunction to eliminate the undesired pulse broadening. An 800 MHz New Focus balanced differential receiver is used to cancel multi-user interference, as discussed in the preceding section.

5.3.1.1 RZ Coding

The codes used in this study are based on cyclic shifts of a single 7-chip m-sequence, $\{0, 1, 0, 0, 1, 1, 1\}$ as proposed in [64], and have the requisite correlation properties for perfect channel orthogonality when used in conjunction with balanced detection. Customised FBGs were designed and fabricated to perform the encoding and decoding operations.

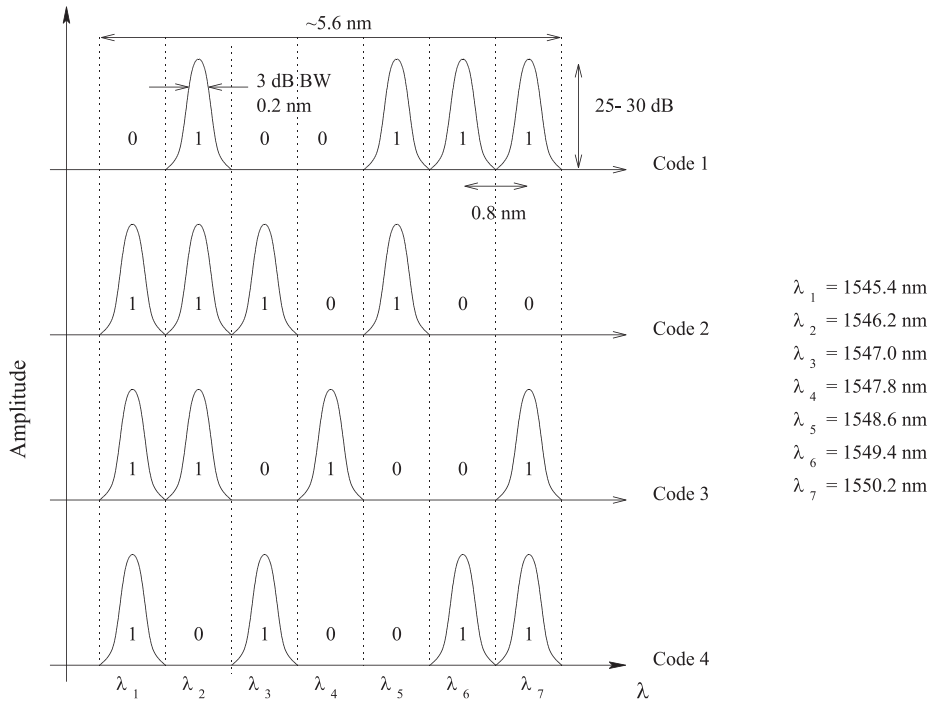

Figure 5.9: Original design for RZ-type coding gratings.

The code gratings were specified with a 0.2 nm (25 GHz) spectral occupancy per chip and a chip separation of 0.8 nm (100 GHz), as shown in Figure 5.9. Each code has 4-*on* chips and 3-*off* chips, with two chips overlapping. The coding scheme employed in this initial experiment is referred to herewith as *RZ-coding*[1] where an *on* slice occupies only half its spectral slot.

[1]The terms *RZ* (return-to-zero) and *NRZ* (nonreturn-to-zero) coding are used throughout this chapter and refer to the spectral occupancy of the individual chips relative to the chip width. In RZ coding, the spectral occupancy of the chip is much smaller than the chip width, while in NRZ coding, the chip spectrum occupies the entire chip width. This particular nomenclature was chosen due to its similarity to the RZ and NRZ temporal modulation formats.

The customised FBGs specified above were fabricated by Dr. Morten Ibsen using our in-house continuous grating writing facility [70]. Code gratings were fabricated as a cascaded four-grating array, each with a length of ∼10 mm, where the distance between two consecutive gratings was ∼1 mm. However, due to errors that occurred during the fabrication process, the chip separation and spectral occupancy of the original design changed to ∼2.0 nm and 0.24 nm respectively. The gratings were placed in tunable mounts (see Figure 5.10) which enabled strain tuning of each individual array, facilitating wavelength alignment between the encoder and decoder gratings. However, note that this tunable mount does not permit strain tuning of individual chips in the code.

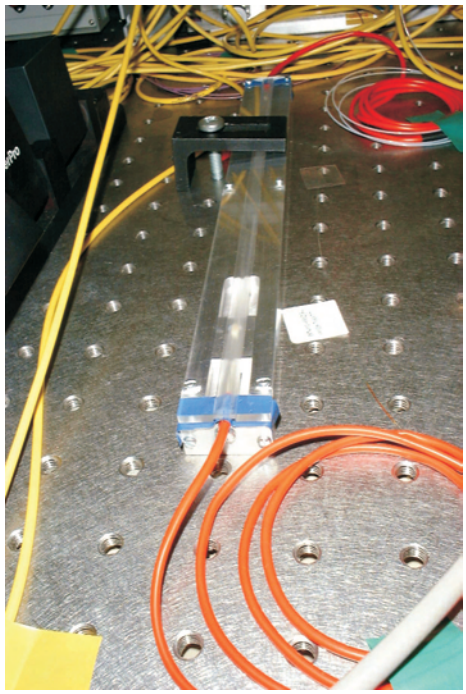

Figure 5.10: Tunable mount for code gratings.

The experimental setup is given in Figure 5.11. Data modulation is performed using $LiNbO_3$ EOMs at a bit rate of 622 Mb/s (pattern length of $2^7 - 1$). Note that as a single pattern generator was used in this experiment, special care was taken to ensure that the path lengths of the two channels after data modulation differed by more than a bit length, to avoid correlation between the two data channels. The decoder reflection and transmission path lengths were matched using a variable delay

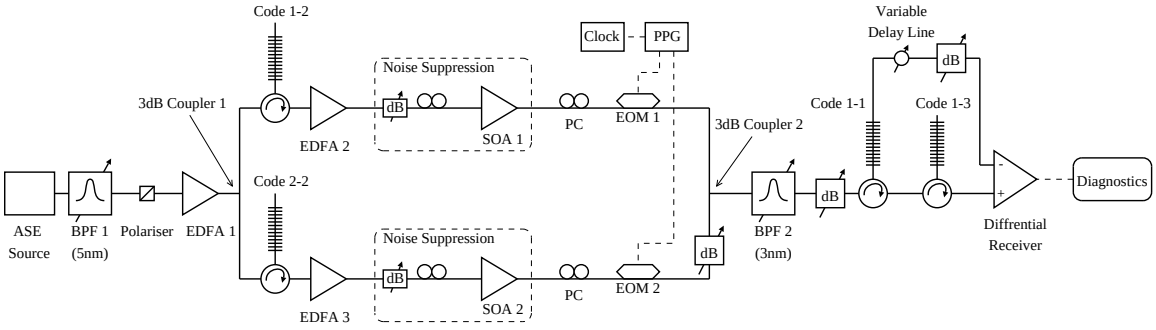

Figure 5.11: 2-channel spectral amplitude coding OCDMA system diagram using an SOA per code.

line, in order to ensure exact alignment of the arrival times of incoming bits at the differential receiver inputs. The powers of the two channels are balanced at the output of 3 dB coupler #2 and passed through to the second bandpass filter, which removes the out-of-band ASE introduced by the SOA. As in previous measurements, the polarisation and power at the input to the SOAs (Alcatel model 1901 and JDS CQF874) are optimised to obtain the best performance.

Two-channel system performance was assessed using a sampling oscilloscope with 622 Mb/s optimised receiver module. Preliminary Q measurements performed with these code gratings[2] proved to be unsatisfactory, and revealed that the individual chips were too far apart for effective differential decoding. The poor performance was partially caused by the low extinction (3-8 dB) of the decoder grating in transmission (see Figure 5.12). Additionally, due to the excess power in the *zero chips* resulting from the modulation of the in-band SOA ASE, a satisfactory eye opening could not be achieved. Recall that ideally, when receiving the *matched channel* (channel matched to the decoder gratings), there is minimal power through the transmission path, while maximum optical power is transferred through the reflection path. However, in this case, the modulated power of the *zero* chips was far greater than that of the *one* chips (i.e. far greater power on the transmission path), resulting in a poor eye at the decoder output.

Although the initial encoder/decoder gratings were not suited for cancellation of

[2]The nomenclature used for the code gratings is as follows: Code 1-1 refers to code 1, grating number 1, Code 2-2 refers to code 2, grating number 2 etc.

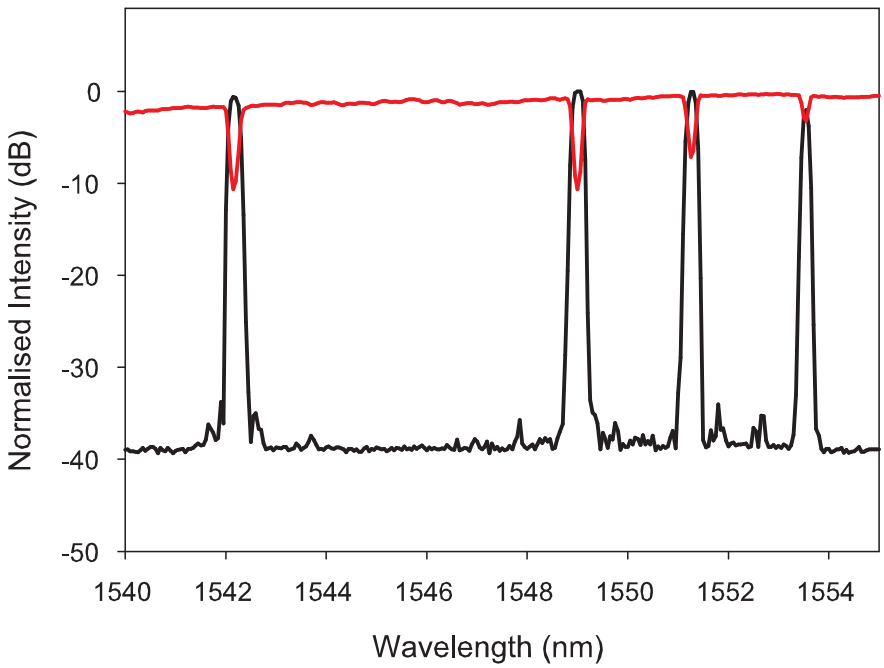

Figure 5.12: Representative reflection (black) and transmission spectra (red) of RZ coding gratings.

multi-user interference via balanced detection, I present here preliminary measurements performed using these gratings, with a single channel using a single-ended receiver. The decoder arrangement is depicted in Figure 5.13. Single ended BER measurements were performed on the matched channel at both 622 Mb/s and 2.5 Gb/s using commercial receivers (Agilent 83446 B/A respectively) and are given in Figure 5.14.

As expected, the use of the saturated SOA provides a noticeable performance improvement relative to the standard approach with no noise mitigation. At higher bit rates, the intensity noise creates a significant system penalty which in turn allows the SOA to provide greater benefit to the system performance. Although these single-ended measurements illustrate the potential of SOA-based noise reduction, new gratings are required in order to accurately determine the benefits of the technique in differential SAC systems.

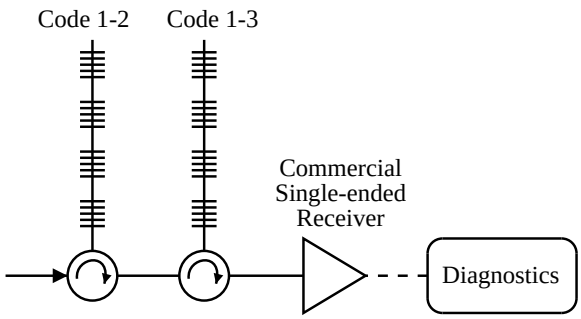

Figure 5.13: Single-ended receiver used for RZ-type coding system experiment.

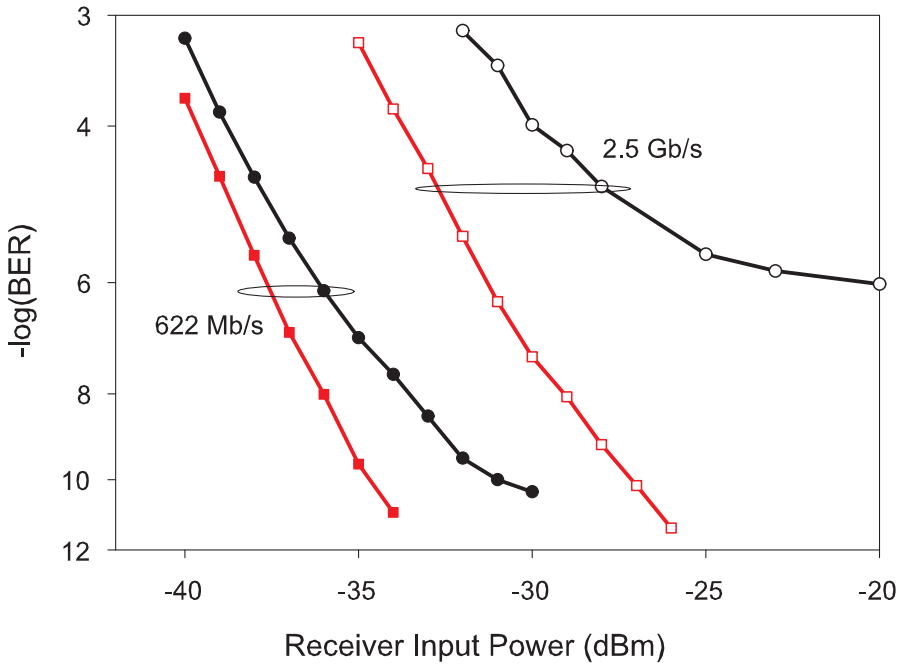

Figure 5.14: BER for RZ-type coding OCDMA system configuration. Measurements shown are for a single matched channel only. Measurements at 622 Mb/s with and without SOA are shown with solid squares and circles respectively. Measurements at 2.5 Gb/s with and without SOA are shown with hollow squares and circles respectively.

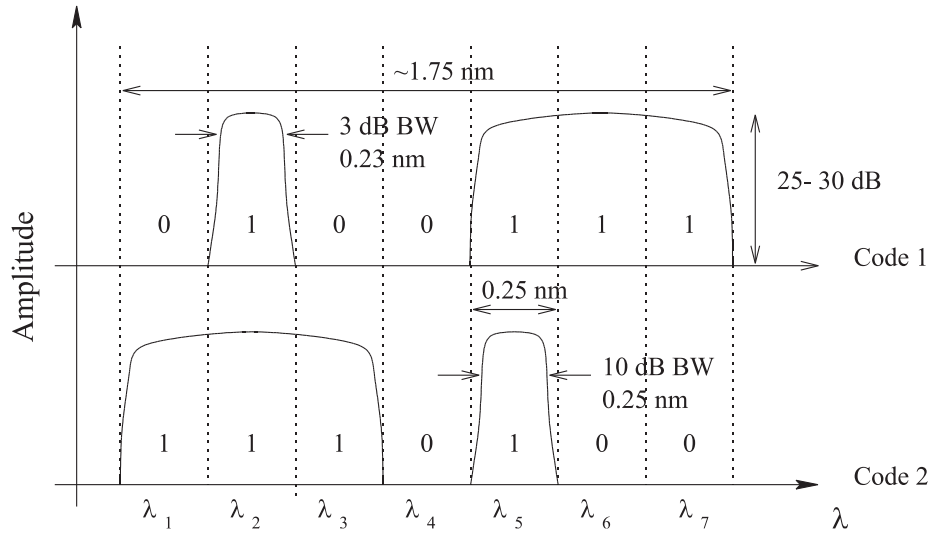

Figure 5.15: Original design for NRZ-type coding gratings.

5.3.1.2 NRZ Coding

To overcome the limitations posed by RZ coded gratings, a new scheme was proposed in which the spectral occupancy of each chip fills the entire designated chip slot. The code uses a chip spacing of 0.25 nm, with nominal 3 dB and 10 dB bandwidths of 0.23 nm and 0.25 nm respectively, as steep filter roll-off is required to obtain a nearly rectangular spectral profile. The new *NRZ gratings* were designed as cascaded two-grating arrays, following the specification given in Figure 5.15. As before, the grating length and separation distance were 10 mm and 1 mm respectively.

Measured reflection spectra of the fabricated code gratings 1 and 2 are shown in Figure 5.16, together with the transmission profile of Code 1. Code 1 was used for the subject channel while Code 2 formed the interfering channel; also referred to here as the *matched* and *unmatched* channels respectively. The experimental procedure is the same as discussed for the preceding experiment and follows Figure 5.11. Eye diagrams are given in Figure 5.17.

For the single matched channel system, a peak Q of 7.2 (BER $\approx 3 \times 10^{-13}$) and 5.5 (BER $\approx 10^{-8}$) was achieved with and without noise reduction respectively. However the eye quality degrades noticeably for the 2-channel system, and the achievable Q approaches ~3.7 (BER $\approx 10^{-4}$) in both scenarios. Decoder input and output spectra with and without SOA-based noise reduction are given in Figure 5.18. Attention is

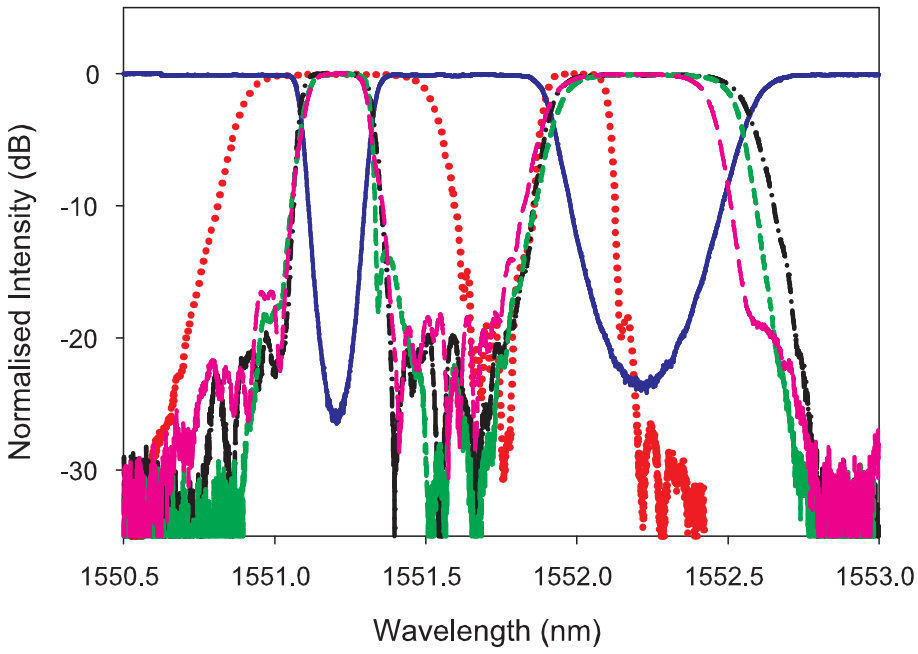

Figure 5.16: Code spectra for matched and unmatched codes. Matched code (Code 1): black dash-dots represents Code 1-1, green short dashes represents code 1-2 and the pink medium dashes represents Code 1-3. The position of these gratings within the experimental setup are shown in Figure 5.11. The solid blue line gives the transmission frequency response of Code 1-1. The red dotted line gives Code 2-2, which is used for the unmatched channel.

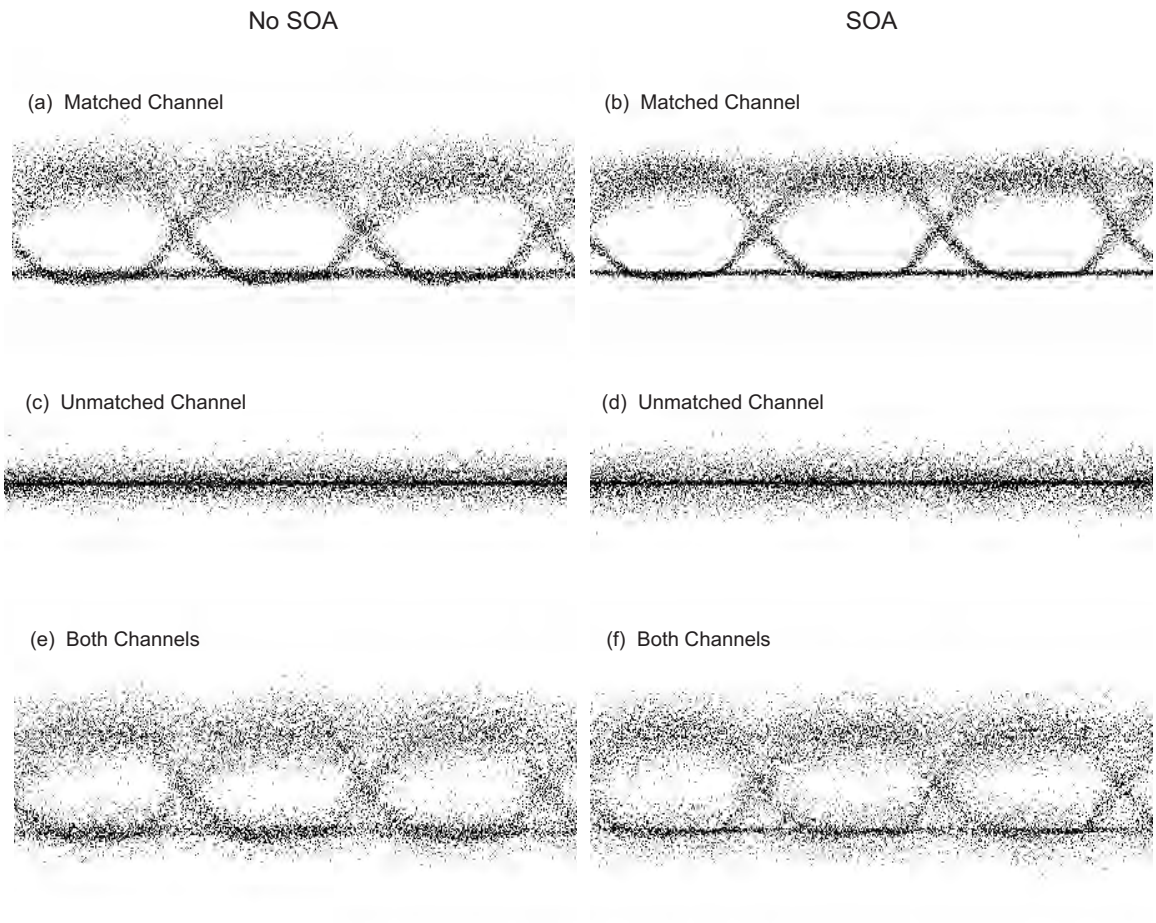

Figure 5.17: SOA per channel results. Eye diagrams are shown for (a) before and (b) after noise suppression for a single matched channel, (c) before and (d) after noise suppression for a single unmatched channel and (e) before and (f) after noise suppression for the 2-channel system. For the matched channel the SOA improves the Q from 5.5 to 7.2, while no change is observed for the 2-channel system.

drawn to the significant spectral distortion caused by the SOA. Although some spectral broadening was expected [30], what was not fully appreciated was the extent of the resulting distortion that would occur for steep input spectral-slices. Furthermore, as is clear from Figure 5.18, substantial spectral filtering of this broadened output occurs at the decoder, causing the observed degradation in signal quality as discussed in prior chapters.

When receiving the matched channel, maximum power transfer occurs through the reflection path of the decoder, while the transmission path, (i.e. the complement of the matched code), blocks most of the light according to the transmission extinction of the decoder grating (Code 1-1 in this case has a transmission extinction of about 20 dB). The matched channel power at the output of Code 1-1 was 8 dB less than the

decoder reflection path, providing good eye quality at the receiver. When receiving the unmatched channel, two chips are filtered in both the reflection and transmission paths, giving approximately equal power at the input to the balanced detector. The decoder and detector arrangement works well in this experiment as is clear from Figure 5.17(c) and (d) where complete eye closure is achieved. However, the SOA does not make an appreciable difference in the noise level of the 2-channel system. The unmatched channel experiences considerable spectral alteration as half of the encoded spectrum is filtered out in each arm of the differential detector.

The decoder gratings are however non-ideal in that they are narrower then the encoder gratings (see Figure 5.16) causing excess optical filtering at the receiver. Noticeable improvements in signal quality are expected with a better spectrally matched decoder arrangement, especially in the case of the single matched channel. However, the signal quality improvement possible for the unmatched channels is eventually limited by the effects of post-SOA filtering.

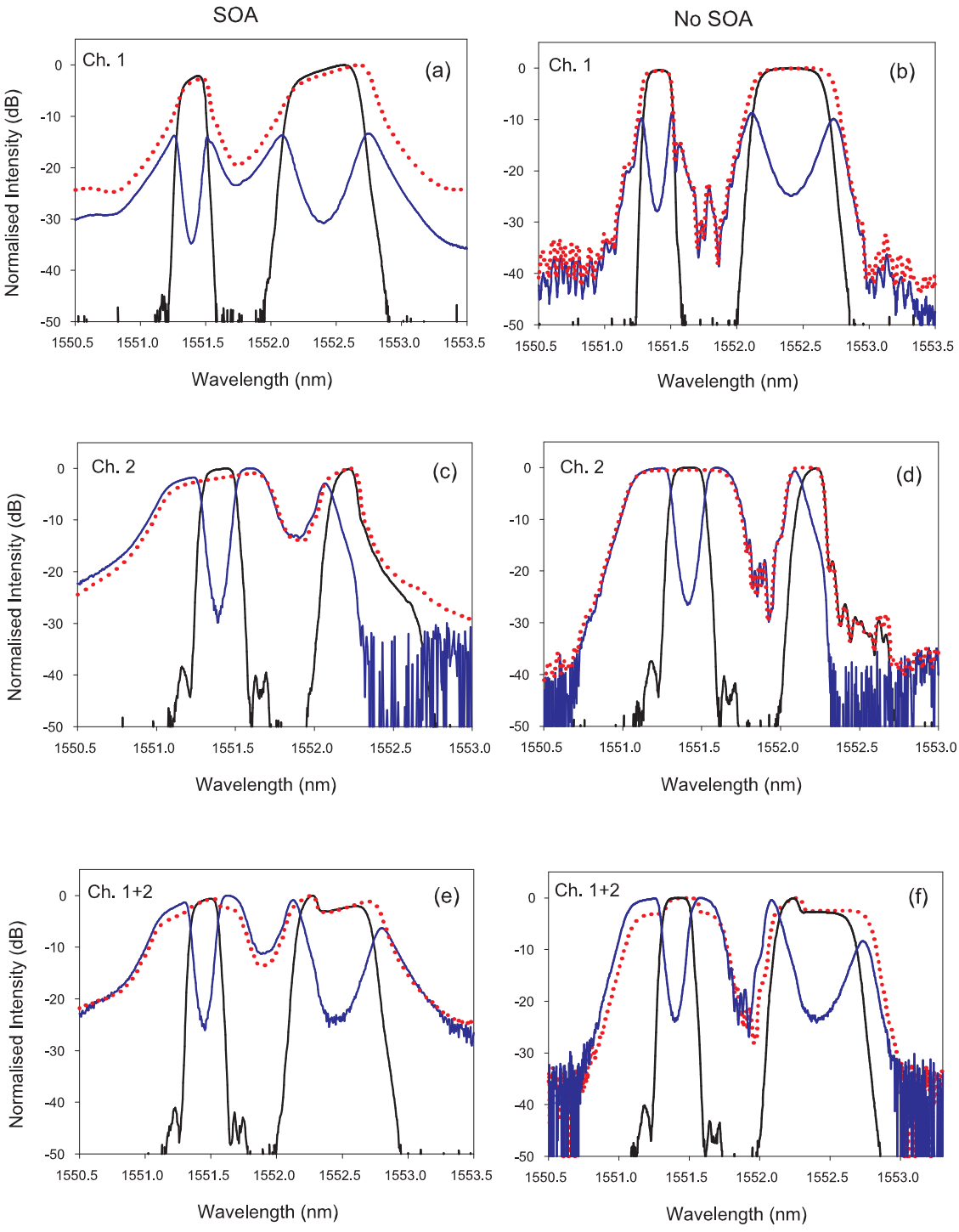

Figure 5.18: Spectra at the decoder input (red dots), decoder reflection path (black) and transmission path (blue) for (a) matched channel only with SOA (b) matched channel only without SOA (c) unmatched channel only with SOA (d) unmatched channel only without SOA (e) both channels with SOA (f) both channels without SOA.

5.3.2 SOA Per Chip

It is clear from the previous section that spectral filtering of the SOA output must be greatly reduced to make SOA-based noise suppression a viable option for SAC OCDMA applications. One system design approach towards reducing these filtering effects is to use an individual SOA for each spectral chip, as in this case, the intensity smoothing is performed on a per chip basis. In the 2-channel system under consideration, this requires six SOAs, as there are six *on* chips (see Figure 5.15). Apart from obvious implementation issues, it was not clear at the time of this study how much system performance improvement would be possible using this method. This section documents my attempts to understand the achievable performance limits of SAC OCDMA when incorporating SOA-based noise reduction.

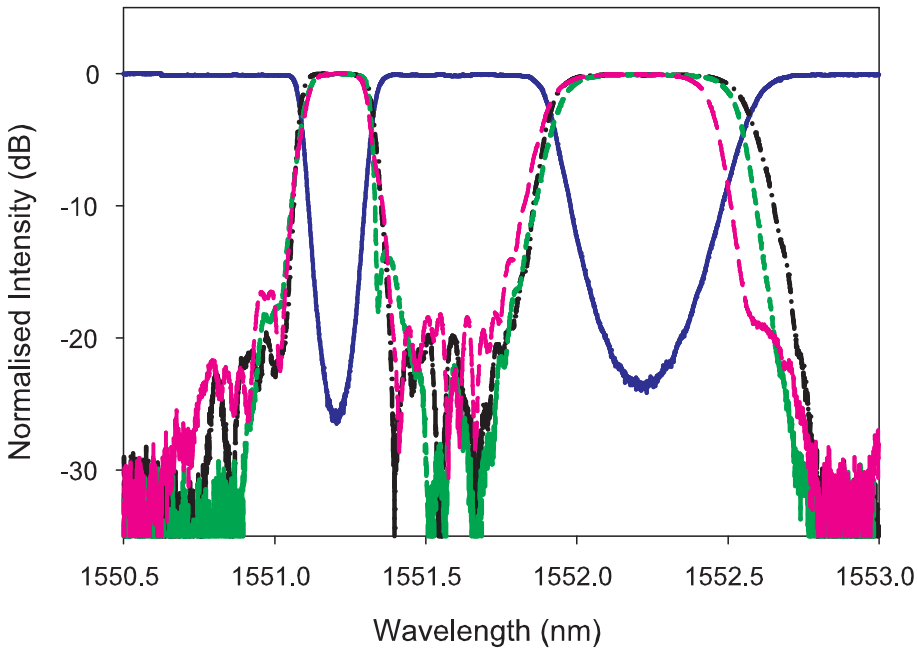

Figure 5.19: Decoder gratings for individual chip cleaning OCDMA system experiment. The solid line (blue) is the transmission response of Code 1-1, the dash-dot line (black) is the reflection response of Code 1-1 the short dashed line (green) is the reflection response of Code 1-2, and the medium dashed line (pink) is the reflection response of Code 1-3.

The NRZ-coded gratings used in the preceding subsection were used once more at the decoder (presented again in Figure 5.19 for convenience), while new single

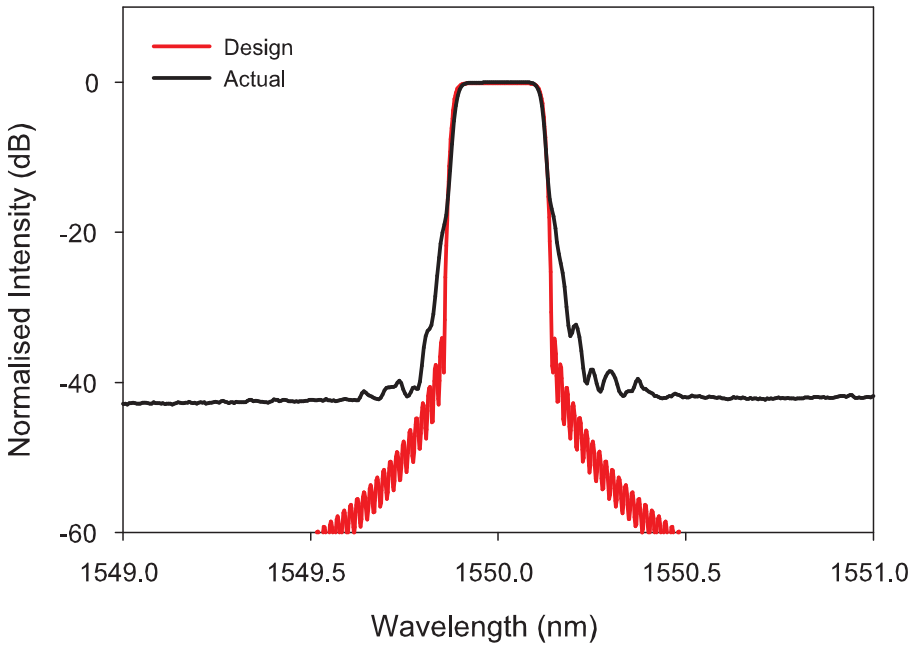

Figure 5.20: Individual chip grating designed (red) and measured (black) reflection spectrum.

chip gratings were employed at the encoder. These encoder gratings, purchased from SPI Inc., were specified with 3 dB and 10 dB bandwidths of 0.24 nm and 0.26 nm respectively. They were fabricated as low-dispersion, single grating structures and have a representative spectral response as shown in Figure 5.20.

Note that in this new scheme, the unmatched channel is not subjected to the drastic spectral filtering as in the previous experiment. Thus system performance benefits are expected for both the matched and unmatched channels. The new 2-channel system schematic is given in Figure 5.21(a). A few photographs of the laboratory setup for the single chip SAC system are also shown in Figure 5.22.

After intensity smoothing by the individual SOAs, the encoder chips (0.25 nm apart as before) are combined to form the two separate codes using a cascaded arrangement of 3 dB couplers as shown in Figure 5.21(b). The two channels are then modulated at 622 Mb/s as previously described. The receiver/decoder arrangement is identical to that in the previous experiments and as before, the powers are balanced at the output of the second 3 dB coupler. Attention is drawn to the fact that in this experiment it was not only important to optimise the polarisation of the light into

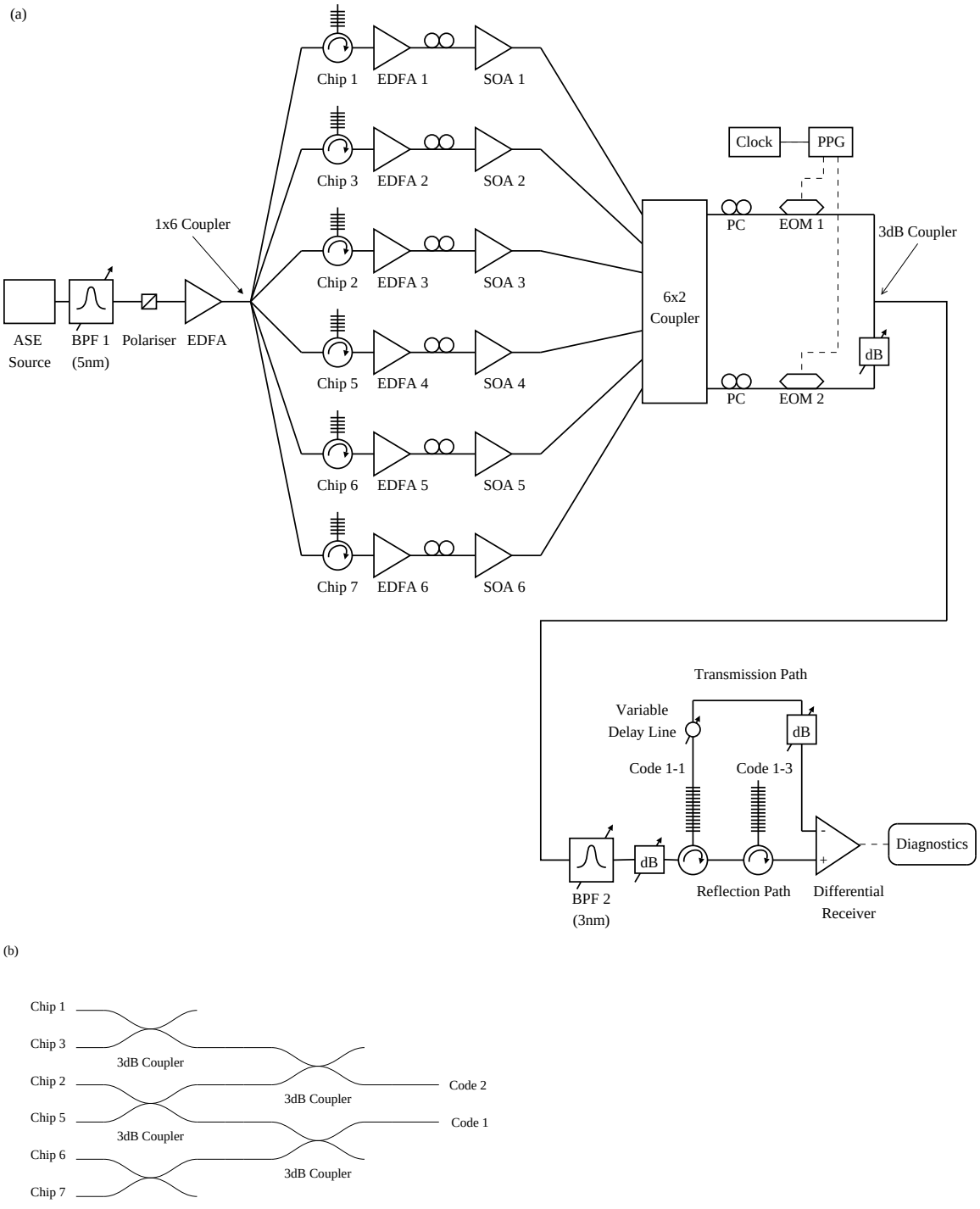

Figure 5.21: (a) 2-channel SAC OCDMA system using an SOA per chip encoding arrangement. (b) 6x2 coupler: combining the chips to form the 2 codes using fused tapered couplers. Chips are numbered as illustrated in Figure 5.15.

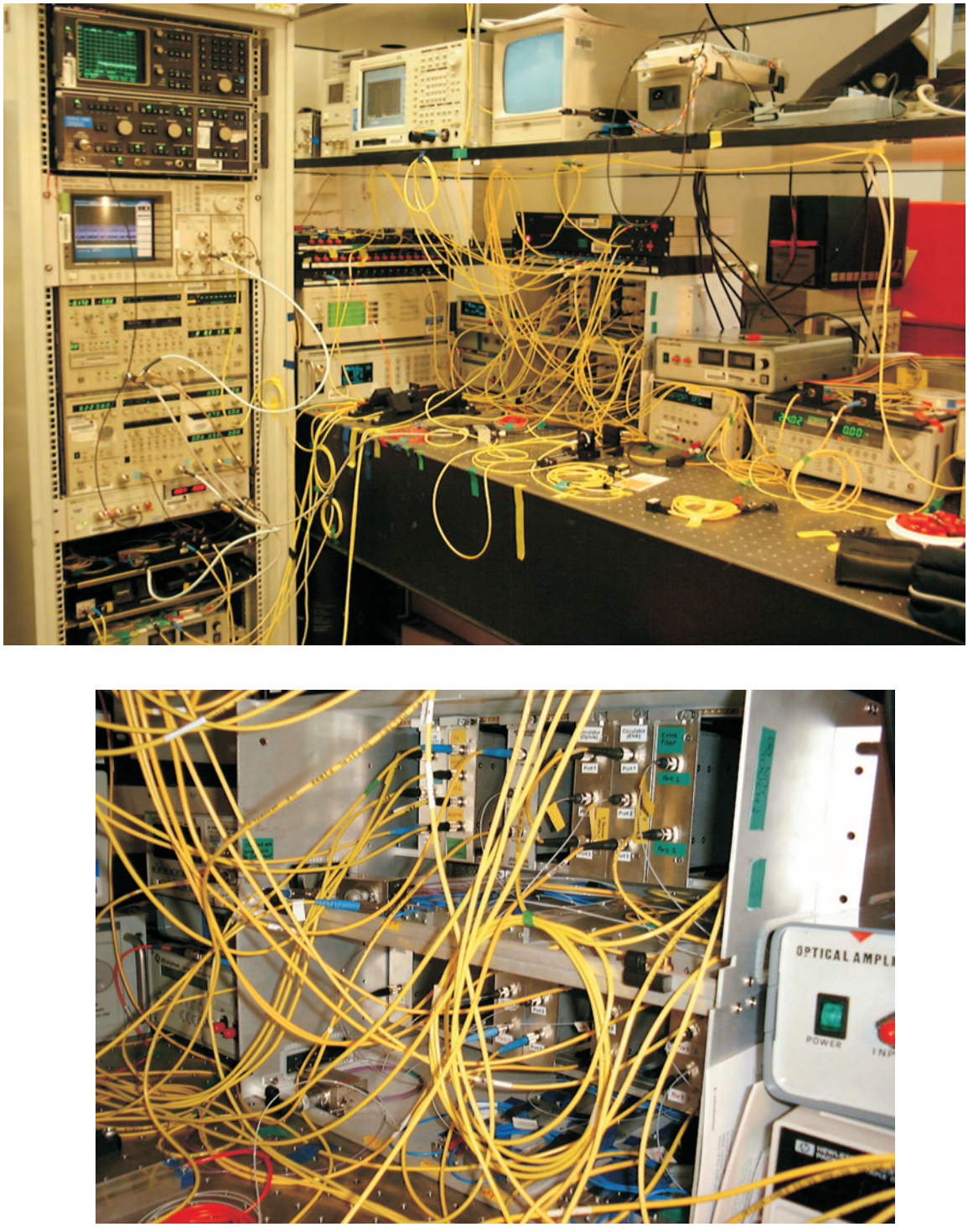

Figure 5.22: (Top) Complete experimental setup. (Bottom) Tunable encoder grating tunable mounts are shown with their corresponding circulators. Tunable mounts are placed directly beneath the corresponding circulators which are mounted in a modular fashion.

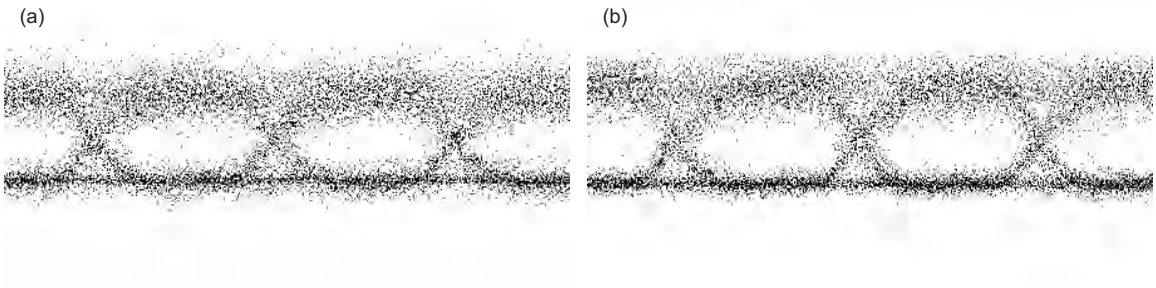

Figure 5.23: Eye diagram results (a) without SOAs and (b) with SOAs for the SOA per chip experiment.

each SOA, but it was also critical to balance the power and modulation depth across all chips, for a fair comparison of 2-channel performance.

The differential receiver 2-channel eye diagrams with and without the SOAs are shown in Figure 5.23. We see that the Q improves from ∼3.7 (BER ≈ 10^{-4}) to ∼5 (BER ≈ 10^{-7}) when incorporating the SOAs. The performance improvement is still limited however, due to the excess spectral filtering at the receiver caused by the narrower, mismatched decoder gratings (see Figure 5.24). Also note that despite the code gratings being tunable, the passbands of the decoder gratings are not individually tunable, thus reducing the possible alignment flexibility with the encoder gratings. System performance can be improved further by shifting the decoder gratings to align with the red-shifted peaks of the spectrally broadened SOA outputs. However, since the performance was highly limited by the still pronounced post-SOA filtering, this effort was not pursued further.

5.3.2.1 Optimised Decoder Grating

As discussed in Chapter 4, reducing optical filtering at the receiver results in significant performance benefits. It becomes clear therefore, that in order to obtain the best system performance, the decoder gratings must be designed to minimise the extent of post-SOA filtering per chip. This involves increasing the chip spacing to reduce the overlap between consecutive chips, increasing the passband of the decoder gratings, and aligning the decoder to the red-shifted SOA output spectrum. The optimum decoder grating must also maintain strong reflectivity, in order to provide good extinction of the undesired chips in both reflection and transmission.

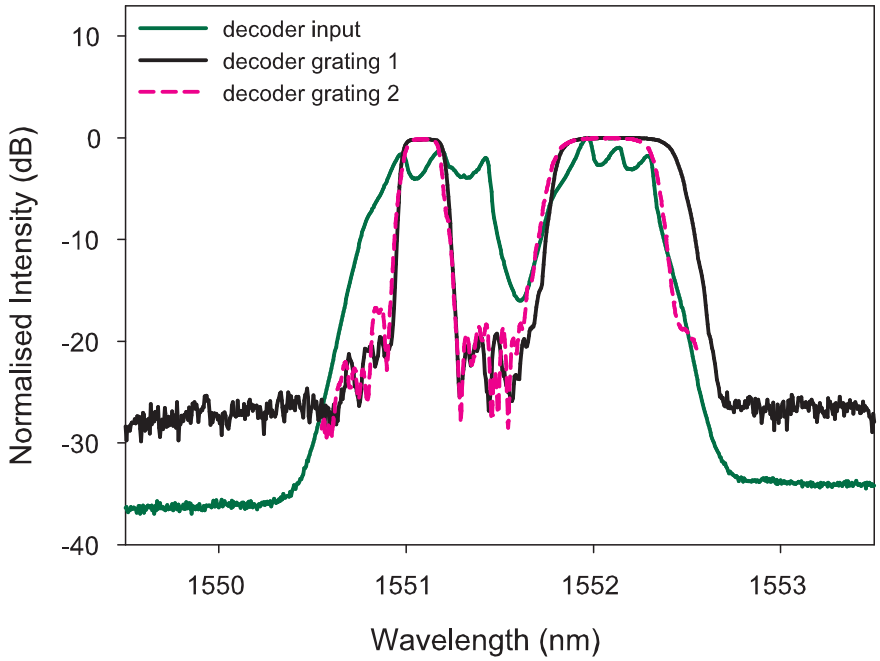

Figure 5.24: Decoder input and decoder grating spectra for SOA per chip experiment.

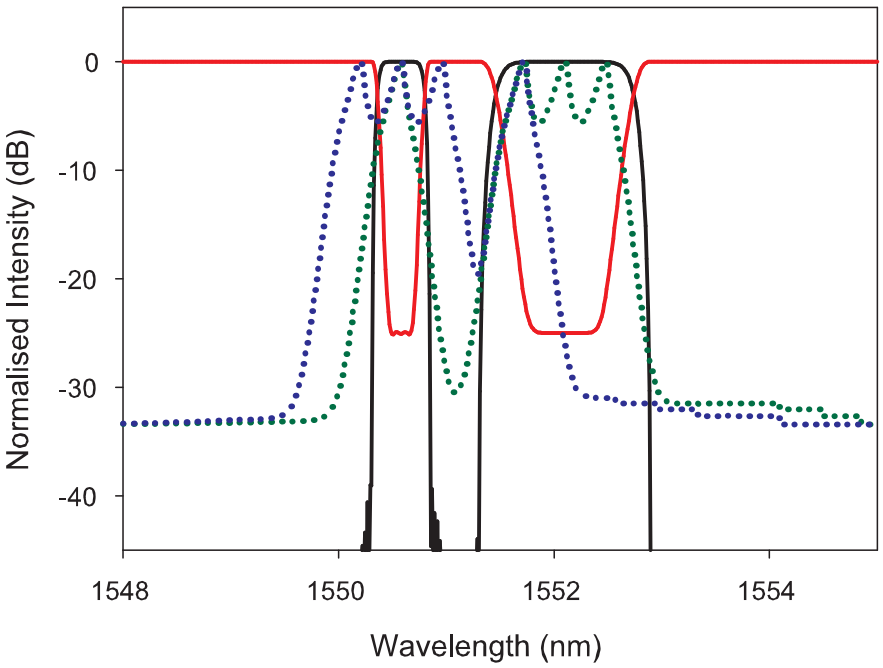

Figure 5.25: 2-channel decoder input spectrum and new decoder grating reflection (black) and transmission spectra (red). The matched (green) and unmatched (blue) decoder input spectra are also shown.

To this end, a superstructured FBG [70] was designed to satisfy the requirements outlined above. The grating was specified with a transmission extinction of 25 dB to ensure proper cancellation of the undesired chips at the output of the decoder transmission path, which requires a strong grating reflectivity of 99.7%. The required grating response is shown in Figure 5.25, together with the encoded spectra for Codes 1 and 2 used in preceding experiments. Note that the chip spacing changed from 0.25 nm to 0.38 nm, in order to allow for the broadening that occurs at the amplifier outputs. The achievable chip spacing is limited by the tuning range of the encoder gratings. The grating was also specified to have zero dispersion in reflection, in order to achieve minimal pulse-spreading of an incoming bit. The design work for the superstructure FBG was performed using commercial grating software, from Attolight Inc. [71], which implements a full time domain layer-peeling algorithm. Figure 5.26 shows the physical design of the grating, in terms of the coupling coefficient, κ, which is directly related to the index modulation profile imprinted onto the fibre. The maximum design value for $|\kappa|$ is $\sim$2.9 mm^{-1}, which is within the capabilities of our in-house grating writing facility.

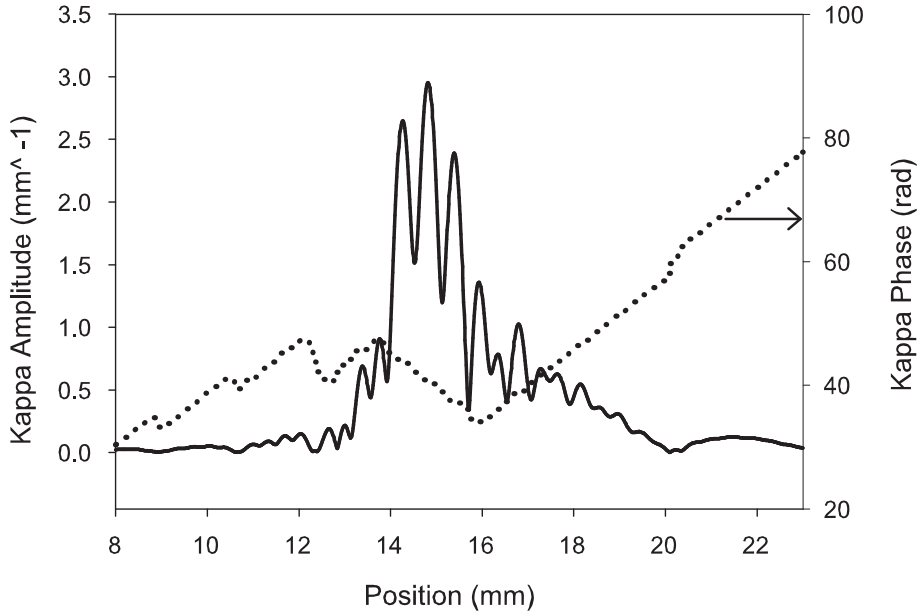

Figure 5.26: Spatial design of the superstructure grating. Kappa amplitude is given by the solid line, and kappa phase is given by the dotted line.

At the time of this writing, the grating had not yet been fabricated, and thus the

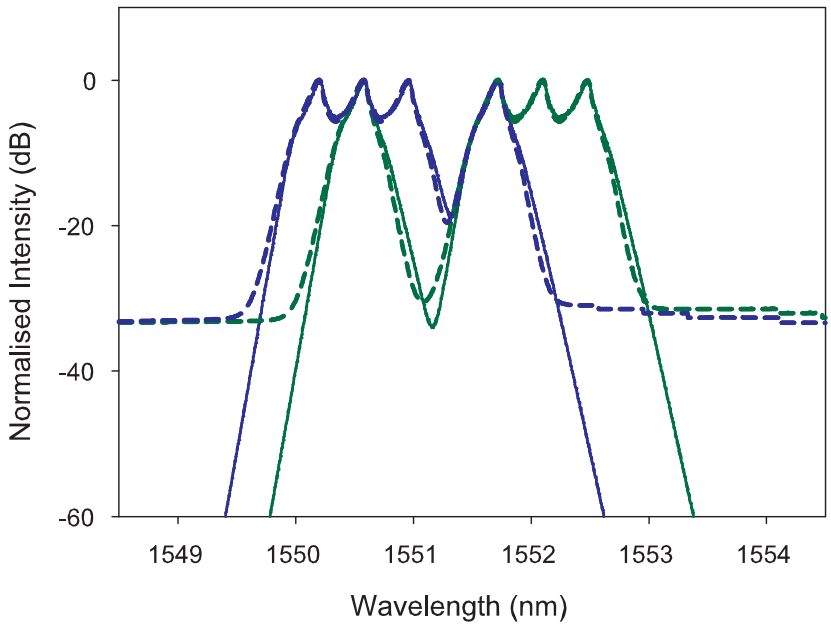

Figure 5.27: Decoder input spectrum. Simulation results for the matched (solid green) and unmatched (solid blue) channels are given. Experimental results (dashed) are also shown for comparison.

system performance improvement has not been experimentally characterised. However, simulations performed using the SOA model (detailed in Chapter 3) follow the trends we expect, showing significant signal quality enhancement over the SOA per channel experiments. These RIN values together with experimental and simulation results from the previous SOA per channel scenario are summarised in Table 5.1. Single channel RIN improvements of $\gtrsim 8$ dB are observed; in linear units this is greater than a factor of 6. We also see excellent agreement between measured and simulated decoder input spectra (Figure 5.27) giving confidence to our predictions. The optimised decoder structure is also expected to provide noticeable eye quality improvement over the preceding SOA per chip experiments.

Although a noise analysis on the multi-channel system performance has not been completed to date, the simulation results presented above, together with the discussions in Chapter 4 regarding performance improvements due to reduced filtering, show the potential to significantly enhance signal quality using the optimised decoder grating. As a measure of expected system performance, a Q of ~ 11.7 at 622 Mb/s (i.e. corresponding to a CW RIN of -123.8 dB/Hz) is estimated for the single matched

Table 5.1: RIN at decoder outputs for SOA per channel and SOA per chip CW experiments.

Path	SOA per channel		SOA per chip
	Experiment	Simulation	(Simulation only)
RX path Ch. 1	-115.177	-115.54	-123.8
RX path Ch. 2	-109.9	–	-119.08
TX path Ch. 2	-112.5	–	-119.31

Note: RX and TX denote reflection and transmission respectively.

channel based on previous experimental RIN vs. Q characterisations. The system performance of the 2-channel system is expected to degrade slightly from this value, due to the additional multi-channel beat noise terms introduced at the detector. We believe that employing the optimised decoder grating represents the best achievable system performance in SAC OCDMA applications incorporating SOA-based noise reduction.

5.3.3 SOA at the Receiver

The primary focus of the work documented thus far has been on using the SOA at the transmitter, for which the nature of spectral amplitude coding creates clear challenges, due to the undesirable effects of post-SOA filtering. In spectrum-slicing this can be overcome by employing the SOA in a preamplifier configuration, after the demultiplexing/spectral decoding process, as discussed in Section 4.4. Here, I present an investigation into extending these techniques to SAC OCDMA in order to understand the system benefits and drawbacks of employing SOAs at the decoder.

The preamplifier approaches have shown varying potential to improve received signal quality, while in all cases they avoid both post-SOA filtering, and eye distortion due to *patterning*. In this study I use the approach of *ASE modulation* as it gave the best performance of the techniques investigated in Section 4.4.

As illustrated in Figure 5.28, the system design largely follows that of the SOA per channel experimental setup, the main difference being the addition of an SOA preamplifier in each arm of the decoder (instead of at the transmitter). An EDFA

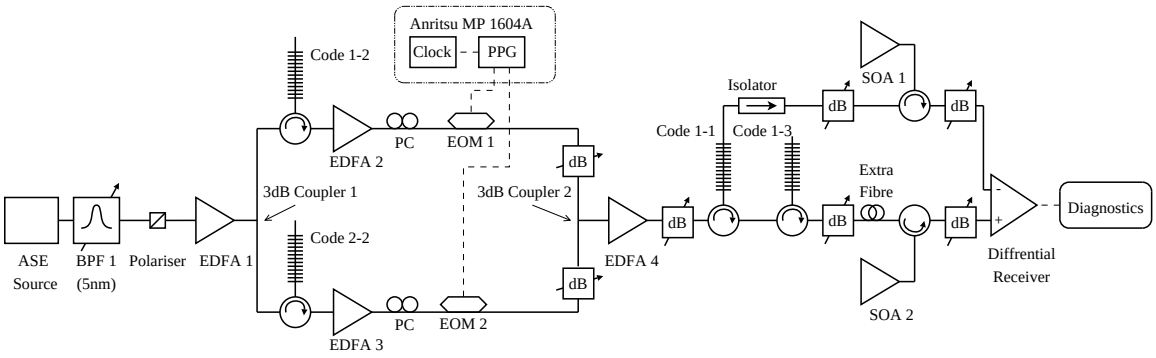

Figure 5.28: Experimental setup for SAC OCDMA using two SOAs as preamplifiers at the decoder. The modulated ASE in response to the input data is received at the detector. PC: polarisation controller

(EDFA 4 in the diagram) was also added after the second 3 dB coupler to ensure sufficient input power to saturate the SOAs. The operating point of each amplifier was optimised to achieve the highest Q, following the approach outlined in Section 4.4.1.

Eye diagrams at the differential detector output for the matched and unmatched channels and the 2-channel system are shown in Figure 5.29. A clean and open eye is obtained for the single matched channel, while the eye-closure for the unmatched channel also shows good noise suppression relative to that with no SOA. However, problems arise during the simultaneous transmission of both channels, when the changing SOA input power levels vary the saturation level of the SOA. Thus, the gain and output power of the SOA become data dependent, yielding a power imbalance between the two arms of the decoder.

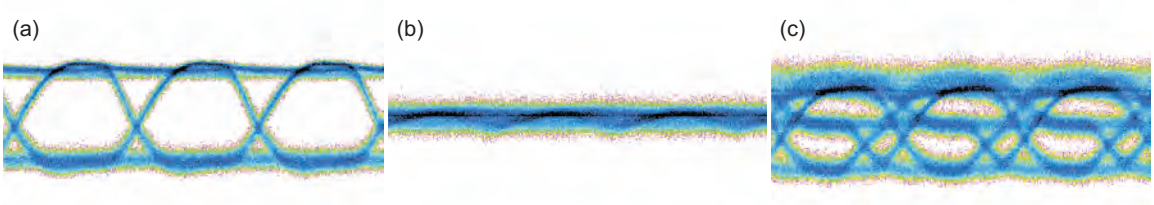

Figure 5.29: Eye diagrams at 622Mb/s (pattern length of 2^7 - 1) for (a) matched channel only (b) unmatched channel only (c) 2-channels SAC OCDMA system using SOA preamplifier technique.

For the 2-channel scenario examined here, at the reflection path output there exist four different power levels corresponding to the following data bit combinations:

i. A *zero* in both matched and unmatched channels.

ii. A *one* in the unmatched channel, *zero* in the matched channel. (Note that in this case, the power level of a one bit, is half that of the matched channel, since there are two common chips in the matched and unmatched codes.)

iii. A *one* in the matched channel, *zero* in the unmatched channel.

iv. A *one* in both the matched and unmatched channels.

On the other hand, only two different power levels are seen at the output of the transmission path (since the matched channel power levels are insignificant in this case) and are the result of:

i. A *zero* in the unmatched channel.

ii. A *one* in the unmatched channel.

Note that for the 2-channel system, both SOAs are optimised for the best overall eye, and not for the best performance for each individual channel. Since the output power of the SOAs will depend on the incoming bit, cancellation of the two unmatched channel powers will not be as effective as that with no noise suppression.

Thus, fundamental limitations prevent the extension of preamplifier techniques to SAC OCDMA applications. Also, note that the example considered in this discussion is that of the simplest 2-channel scenario. However as the number of channels increase, the number of input levels to the SOA increases accordingly, making the SOA preamplifier approach infeasible for SAC OCDMA applications.

5.4 Summary and Discussion

This chapter documents the chronological progression of my initial Ph.D. work into the feasibility of incorporating SOA-based noise reduction in SAC OCDMA applications. It is to be appreciated that the bulk of the work presented here was performed without the understanding gained in hind-sight of the post-SOA spectral filtering effects discussed in previous chapters.

Customised FBGs were employed in all SAC experiments, where both RZ and NRZ type coding schemes were investigated. NRZ coded gratings were found to give better system performance and avoid the drawbacks of RZ coding. Note that the severe limitations of the RZ coding scheme were primarily due to errors in the fabrication process, which resulted in an inter-chip spacing far greater than specified in the original design. The NRZ type gratings were well suited to the differential detection process where eye cancellation was satisfactorily achieved. However employing an SOA per channel produced unsatisfactory results due to considerable decoder filtering of the intensity smoothed light. Employing an *SOA per chip* was therefore proposed to minimise these effects and reduce the signal degradation resulting from decoder filtering. Using this technique, preliminary results showed potential for noticeable improvement in signal quality. The final phase of this work involved the designing of a superstructured FBG for optimum system performance which we believe, when used with the SOA per chip approach, will result in the best system performance of the methods investigated.

However, the system complexity of employing an SOA per chip, gives rise to obvious questions regarding the practicality of the technique. The fact that the systems investigated here used an additional EDFA *per SOA*, provides fuel to the above argument. In terms of achievable noise suppression, the SOA can certainly be driven at a lower operating point, therefore avoiding the need for the additional EDFAs. However, as discussed in Section 3.3.1, this will result in lower suppression benefit. By employing a single high power ASE source, this suppression penalty could be reduced while maintaining lower system costs. The system presented here is also merely a proof of concept, while a deployable system would look substantially different in terms of the number and nature of the constituent components. For example,

instead of employing fibre based sources, a more cost effective approach would use LEDs and arrayed waveguide gratings (AWGs) or dielectric thin film filters integrated monolithically onto a single chip, together with the SOAs. Using polarisation insensitive SOAs with lower saturation powers would further reduce the number of required components. In the proposed 2-channel SOA-per-chip system, six *on* chips were used, requiring six SOAs. Although this appears impractical, it is interesting to observe that, as the channel count increases, the total number of SOAs required for the *per channel* system approaches that of the *per chip* scenario. It is also to be appreciated that the cost of a single SOA is ultimately a question of market demand and that the device has the potential to become low cost, as with any mass-produced semiconductor component. The SOA design optimisations to reduce the linewidth enhancement factor α, as discussed in Section 3.6.2 will also result in significant advantages in SOA per chip SAC applications. However, despite the benefit that reduced α designs offer, the SOA per channel schemes will still provide limited performance.

It is clear from my results that post-SOA filtering effects form the fundamental limitation of SAC OCDMA systems incorporating SOA-based noise reduction. The benefits of employing a saturated SOA in spectrum-slicing do not extend to SAC OCDMA applications due to the unavoidable nature of the spectral decoding process. The conclusion of this study is therefore that SOA-based noise reduction is not a feasible and practical engineering solution for spectral amplitude coded OCDMA systems.

Chapter 6

Relaxation Oscillation Noise Reduction in a Fibre DFB Laser

Overview: This chapter records our work on using the saturated SOA to reduce the RIN peak in a fibre distributed feedback (DFB) laser, for use in low frequency sensor applications. It is shown that the gain dynamics of the amplifier allows a reduction of 30 dB in the relaxation oscillation (RO) noise component of the fibre laser.

6.1 Background

Thus far, I have examined the saturated SOA as a means of reducing the excess intensity noise of thermal-like incoherent sources, for use within telecommunication systems. However, it should be appreciated that the saturated SOA is a powerful and versatile tool that can be extended to a variety of different applications. In this chapter, I present a preliminary investigation into using the nonlinear properties of the amplifier to reduce the RIN peak of a highly coherent fibre DFB laser.

The fibre DFB laser is an attractive alternative to semiconductor diode lasers, due to its fibre compatibility, narrow linewidth, and low intensity noise. However, the characteristic RO peak in the laser noise spectrum, caused by coupling between the population inversion and the photon density in the gain medium [72], can limit sensitivity in low frequency applications such as sensing and metrology.

Previously, an optoelectronic feedback method has been used to produce a RIN

peak reduction of 30 dB in a fibre laser by modulating the pump drive current out-of-phase with the laser intensity fluctuations [73]. However, this approach requires careful characterisation of the laser response to pump current fluctuations. A simpler, all-optical approach towards reducing the RO noise peak is to use the gain dynamics of a saturated SOA. A similar technique has been used to suppress beat frequencies in a ring laser by introducing an SOA into the cavity [74]. In this chapter we present the first reported characterisation of the use of an external SOA for RO peak reduction in a fibre DFB laser [75].

6.2 SOA for RIN Peak Reduction

The work presented in this chapter was performed in collaboration with Dr. Libin Fu. The C-band fibre laser, with operating wavelength 1552.1 nm, was fabricated by Dr. Morten Ibsen.

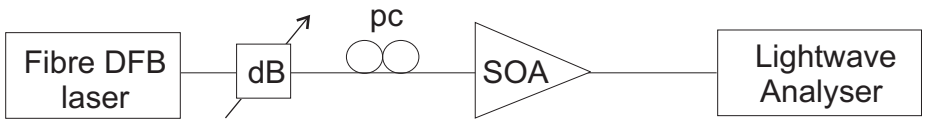

Figure 6.1: Basic experimental setup of RIN peak reduction experiment.

The basic experimental setup is given in Figure 6.1. The laser, a single polarisation Er-Yb codoped fibre DFB with cavity length of 5 cm, was pumped at 980 nm in a counter propagating configuration. Further details of the laser design can be found in reference [76]. The output power of the laser was set to 10 dBm, yielding an RO frequency of ∼930 kHz. The output of the laser was then attenuated to ∼5 dBm before being launched into the SOA, while the amplifier drive current was set to 200 mA. This combination of drive current and optical input power ensured that the SOA (Alcatel model 1901) was operated in the gain saturated regime as determined by the amplifier gain characteristics (see Figure 6.2). The signal polarisation was also adjusted to maximise noise suppression.

As in previous chapters, we measured the noise PSD before and after the SOA using an Agilent lightwave analyser (Figure 6.3(a)). Note that the apparent increase in RIN visible at frequencies lower than ∼600 kHz is caused by the noise floor of the

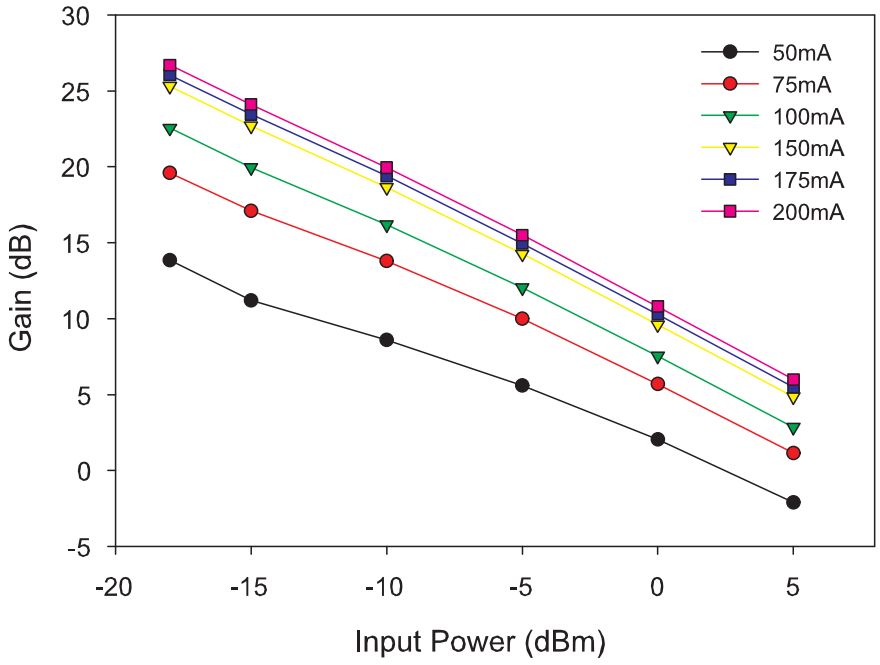

Figure 6.2: Gain curves as a function of drive current and coherent input power for the Alcatel model 1901 SOA.

lightwave analyser. Thus in order to better examine the low frequency response, the noise PSD was further characterised across a frequency range of 30-700 kHz using an electrical spectrum analyser and a 125 MHz bandwidth high sensitivity photodetector (Figure 6.3(b)).

By using the SOA, we are able to reduce the RIN peak from -110 dB/Hz to less than -140 dB/Hz, thereby achieving a RIN improvement of 30 dB. Although Figure 6.3(b) shows intensity noise suppression at frequencies as low as 30 kHz, the true extent of the noise suppression is obscured by the thermal noise floor of the photodetector. However, from the theoretical analysis presented in Chapter 3, noise suppression is expected to extend down to DC. At frequencies greater than the noise suppression bandwidth of the SOA ($\sim$4 GHz), a slow increase is observed in the RIN spectrum, which is attributed to the unsuppressed beat noise introduced by the amplifier ASE. At 10 GHz the RIN value with the DFB alone is -163 dB/Hz, while the saturated SOA increases this to -150 dB/Hz.

The optical spectrum of the laser before and after the SOA is shown in Figure 6.4(a). Although the amplified spontaneous emissions from the SOA reduce

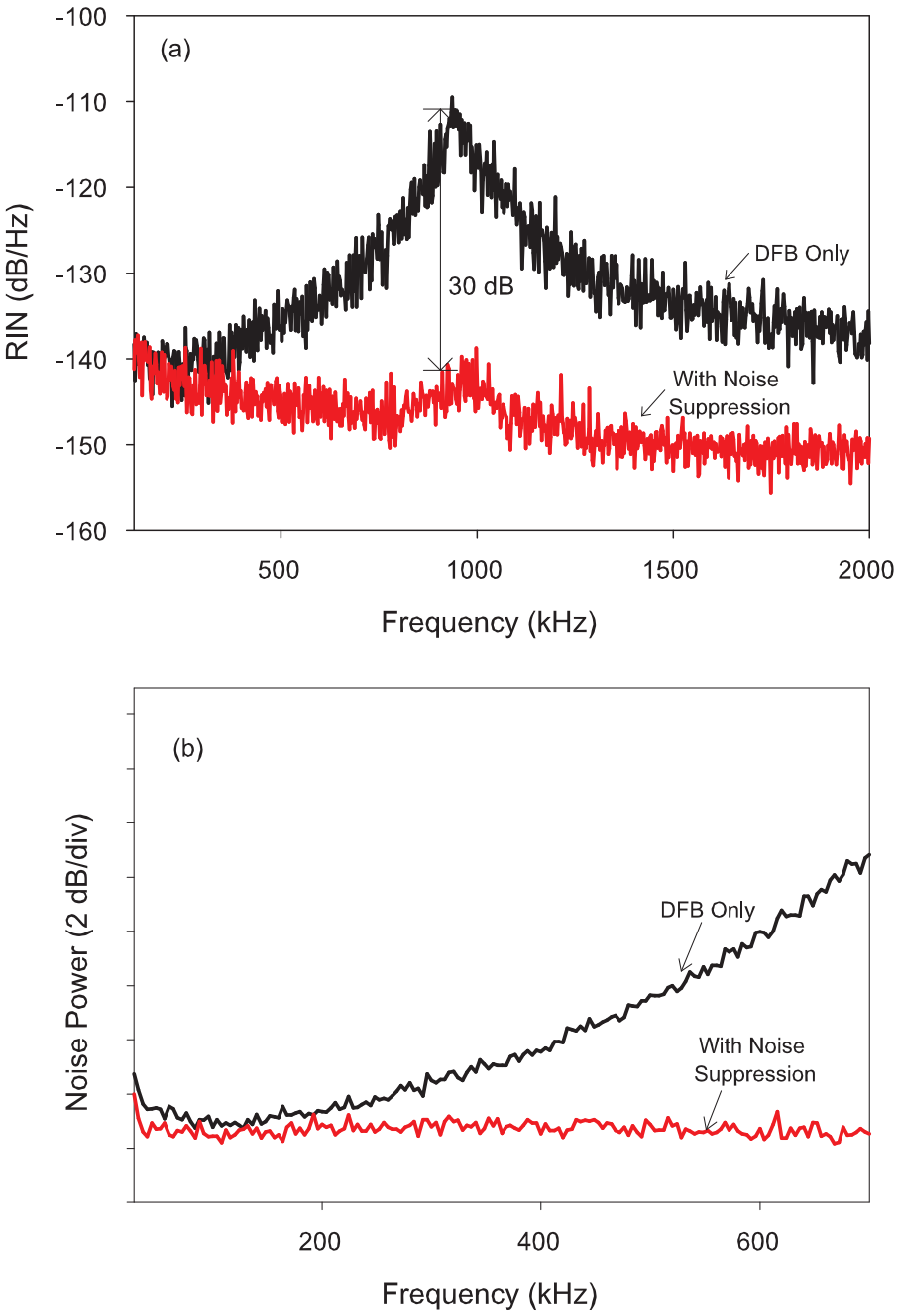

Figure 6.3: (a) RIN measurements before and after noise suppression using a lightwave analyser. The apparent increase in RIN visible at frequencies lower than 600 kHz is caused by the noise floor of the analyser. (b) Low frequency noise power spectrum (30-700 kHz) using an electrical spectrum analyser and a 125 MHz high sensitivity photodetector

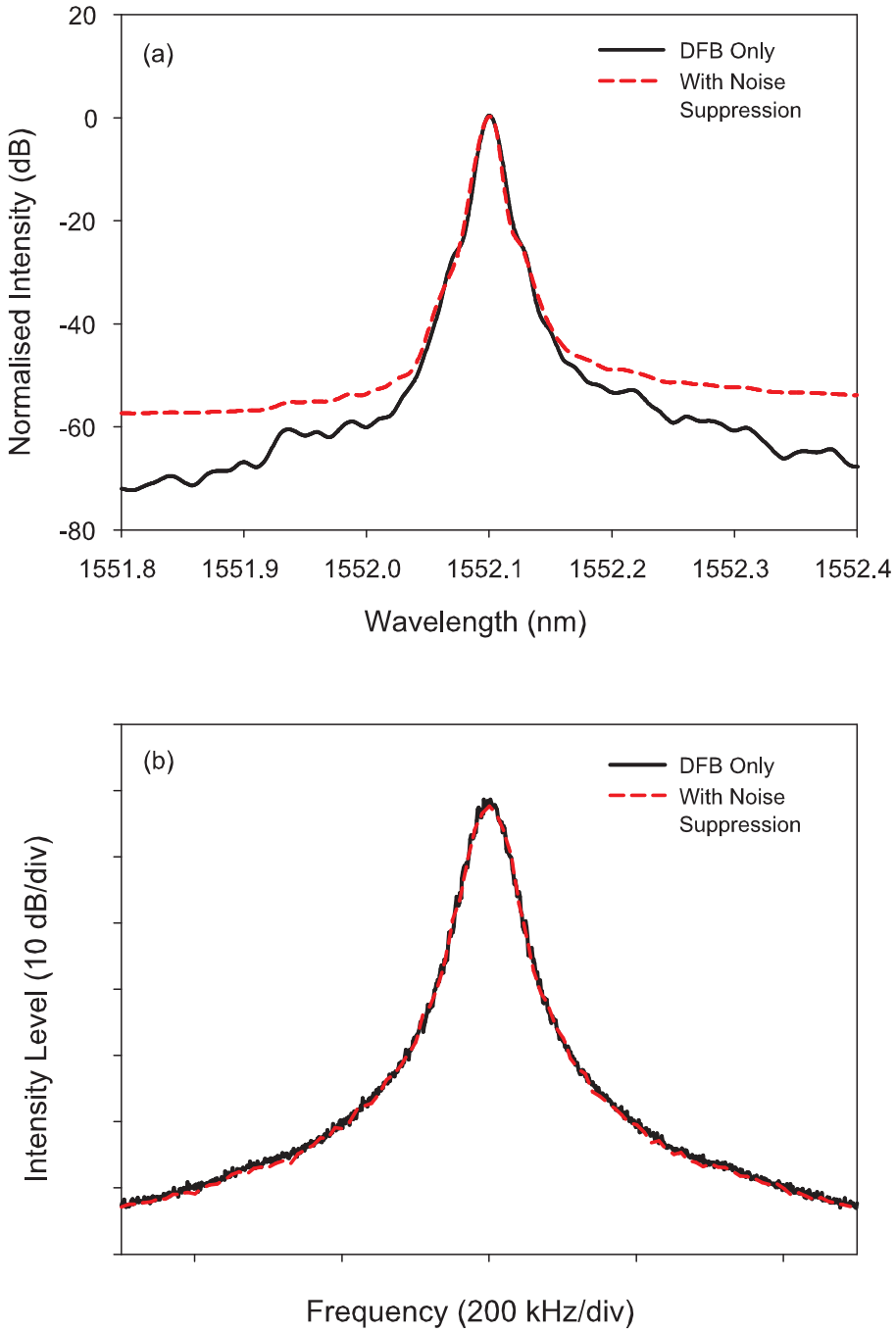

Figure 6.4: (a) Optical spectra from optical spectrum analyser with a 0.01 nm resolution bandwidth. (b) Laser linewidth measurements before and after the SOA using the delayed self-heterodyne technique with resolution 3.5 kHz.

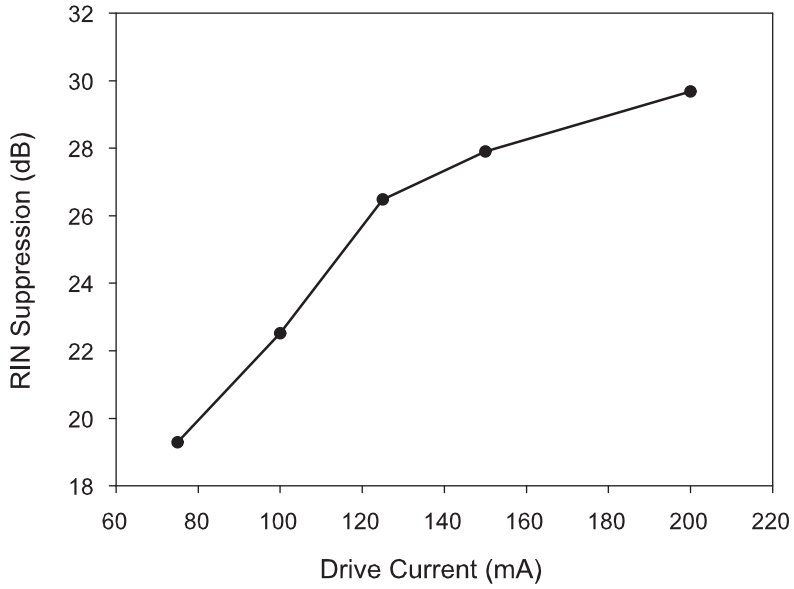

Figure 6.5: RIN suppression as a function of SOA drive current, at a constant input power of 5 dBm.

the optical signal-to-noise ratio (OSNR), the OSNR of the SOA output signal is still greater than 55 dB. Unlike the incoherent spectrum-slices discussed in previous chapters, the laser spectrum does not exhibit any noticeable red-shift or distortion. This was further confirmed by laser linewidth measurements using the delayed self-heterodyne technique (3.5 kHz resolution) as discussed in [15]. The 3 dB linewidth was measured to be ∼14 kHz, and no noticeable difference in the laser linewidth was observed before and after noise suppression (Figure 6.4(b)). The spectral distortion effects examined in Chapter 3, arise from the amplitude-to-phase coupling within the SOA, and are a function of the intensity noise level launched into the device; thus their absence here is attributed to the high intensity stability of the fibre DFB laser.

For high input powers, significant RIN suppression is achieved even at relatively low levels of SOA drive current. This is clear from Figure 6.5, where the RIN peak suppression is characterised as a function of amplifier drive current, for a constant input power of ∼5 dBm. The observed suppression benefits are attributed to the still pronounced amplifier gain compression present at these current levels.

As discussed in detail in Chapter 3, the noise suppression achieved by the SOA is a result of the inverse relationship between the light intensity and the gain of the

saturated amplifier. Thus any small signal modulation present on a high intensity CW carrier will be suppressed as it travels through the SOA. As illustrated in Section 3.3.1, the frequency range over which this suppression occurs is determined by the carrier lifetime of the device and is on the order of a few GHz. These properties make this technique well suited for applications requiring narrow linewidth, high sensitivity and intensity stability at low frequencies, and has the added benefit that the SOA can also be used as a modulator in techniques such as time-gating based sensor multiplexing [77].

6.3 Summary and Discussion

To summarise, the gain saturated SOA provides a simple and effective method for reducing the RO peak and low frequency intensity noise in a fibre DFB laser. Using this technique, the RIN peak was reduced to less than -140 dB/Hz, achieving a noise reduction of ∼30 dB. Significant suppression in a 0-4 GHz frequency range is achieved.

The preliminary investigation presented herein was limited to a single RO frequency. However, as the magnitude and frequency of the RO peak depend on the laser pump power [78], it would be valuable to characterise the RIN reduction across the entire noise suppression bandwidth of the SOA to determine the minimum achievable RIN. However, a very low noise detector will be required for these experiments, in order to fully appreciate the benefit of the saturated SOA. In accordance with previous analysis [27], greater than 30 dB RIN reduction is expected at lower RO frequencies.

In comparison with semiconductor DFBs, fibre DFB lasers have generally superior noise characteristics across a wide frequency range. However, in terms of its use for sensing and metrology, fibre lasers have the disadvantage that the RO peak occurs at very low frequencies (i.e. less than a few megahertz), in comparison with the gigahertz RO frequencies of laser diodes [52]. As a result, RO suppression gives fibre lasers a distinct advantage over semiconductor lasers, thereby enhancing the potential of fibre DFB technology for low frequency sensor and metrology applications.

Chapter 7

Conclusions and Future Work

This thesis documents my work into the feasibility of employing SOA-based noise reduction in low-cost communication systems. Incoherent light sources have the potential to significantly reduce system costs for 'close to end user' network applications, but suffer from excess photon noise which imposes limits on achievable SNR. Thus, research efforts have focused on techniques to reduce this intensity noise, and enhance received signal quality. The gain dynamics of a saturated SOA provide a simple and elegant solution to reducing the excess noise of these sources, allowing significant improvements in system performance.

However, I have shown that optically filtering the intensity-smoothed SOA output light can result in increased intensity noise, thus reducing the added benefit of this noise suppression technique. This phenomenon originates from the loss of intensity correlation between spectral components of the SOA output when the signal spectrum is altered. Any other occurrences that affect these correlations, such as dispersion or polarisation, can also lead to signal degradation. Nevertheless, these adverse effects can be significantly reduced by system and device optimisations. In particular, calculations show that substantial signal quality improvement can be obtained by decreasing the device linewidth enhancement factor, α, while maintaining a high level of gain compression.

As a consequence of the post-SOA filtering effects, a design tradeoff is introduced between intensity noise and crosstalk in high-channel density spectrum-sliced systems. In order to maximise system performance, this leads to an optimal bandwidth of the

demultiplexer filter. This filter width was shown to be wider than the given channel spacing, in contrast to traditional spectrum-slicing without noise reduction. The need to consider the effects of channel and receiver filter shape/width in the design of high channel count systems employing SOA-based noise reduction was clearly demonstrated in this study.

Despite these challenges, I believe that the saturated SOA provides an effective and viable solution for spectrum-slicing applications, offering excellent value for low-cost markets. However, as I have demonstrated in Chapter 5, the same cannot be said for SOA per code SAC OCDMA techniques, where the spectral filtering at the receiver cannot be reduced due to the inherent spectral decoding process. This imposes substantial limitations to the practical applicability of SOA-based noise reduction in SAC applications.

Brief investigations into the use of a saturated SOA to reduce the RO noise peak in a fibre DFB laser were also presented. Despite the low frequency RIN peak, its generally superior noise characteristics, combined with narrow linewidth and fibre compatibility, make the fibre DFB an attractive alternative to its semiconductor counterpart. The simplicity and effectiveness of our proposed technique enhances the potential of fibre DFB technology for low frequency sensor and metrology applications.

Future Work

Optimum Slice Width for Spectrum-Slicing

In Section 4.2.2, I presented experimental results of the estimated spectral efficiency for a multi-channel system with channel/slice width of 0.24 nm. However, as previously posed, an interesting follow-on study to this work would be to find an optimum input slice width that would maximise the spectral-efficiency, given commercially available SOA device parameters. A numerical study would be the most promising approach, as it gives greater flexibility to study the effects of multiple design parameters than corresponding experimental methods. Additionally, the performance of the overall network/system could be assessed using commercial design tools such as

VPI Transmission Maker [79]. This would be an important benchmark for system designers for comparison with other potential metro/access solutions, and enable final conclusions to be drawn regarding the commercial viability of SOA-based noise reduction for spectrum-slicing.

OCDMA System Performance with Optimised Decoder FBG

In Chapter 5 I presented the design of an optimised superstructure grating, expected to greatly minimise the post-SOA filtering effects at the decoder. However, the grating was not available at the time of this writing. Despite the practical limitations and questionable economic viability of employing an SOA per chip, simulations suggest significant performance improvements possible for the two-channel system. It would be beneficial therefore to experimentally characterise the two-channel system with the optimised decoder and verify the expected improvement in system performance.

Noise Suppression of Optimised Structures

Recent advances in the development of quantum dot (QD) SOAs have shown great potential in the use of these devices as nonlinear elements for all optical signal processing [80, 81]. As discussed in Chapter 3, studies have shown a marked reduction in the α parameter of optimised QD and quantum well (QW) devices, in comparison with standard heterostructures. In view of the results reported in this thesis, it would be exciting to characterise these structures in order to experimentally verify the signal quality improvement possible with current device technology. This work would however require collaboration with semiconductor groups. Such optimisations in device structure could lead to significant overall system improvements in spectrum-sliced systems employing SOA-based noise reduction, while market demand and economy of scale would ensure excellent value for metropolitan and access markets.

Noise Characteristics of Intensity Smoothed Coherent Light

In view of the significant RIN peak suppression (of a fibre DFB laser) offered by the saturated SOA, further evaluations are needed to establish the viability of the tech-

nique for low frequency sensing applications. Interferometer based sensor systems require a highly coherent, stable, low-noise carrier signal, and as such it is important to evaluate these properties before and after noise suppression. The absence of laser linewidth broadening at the SOA output indicated low phase noise, however, it would be valuable to quantify the coherence length and phase noise of the light before and after intensity smoothing. It would also be interesting to combine current optoelectronic noise compensation schemes with the proposed SOA-based noise reduction. In addition to providing further noise reduction, these schemes could help in reducing higher frequency beat noise caused by amplifier ASE. Note that amplifier ASE can also be reduced by optical filtering the nonlinearly amplified laser signal. However, the impact of spectral filtering on the low frequency noise needs to be carefully assessed in view of the post-SOA filtering signal degradation observed in thermal light systems.

Appendices

Appendix A

Calculating RIN for Thermal Light

This appendix contains a few further details on the thermal light RIN calculations presented in Chapter 2. The program was written in MATLAB and calculates the noise PSD, $S(f)$, described by,

$$S(f) = \alpha^2 I_o^2 R_L \int_{-\infty}^{\infty} \psi(\nu + \frac{f}{2})\psi(\nu - \frac{f}{2})d\nu \tag{A.1}$$

The integral is implemented in the model as a summation:

$$S_{num}(f) = \alpha^2 I_o^2 R_L \sum_{\Delta\nu} \psi(\nu)\psi(\nu - f)\Delta f \tag{A.2}$$

which is used to calculate the RIN at the desired electrical frequency, f, of interest. Recall that RIN is the ratio of the noise PSD to the average power, and is thus independent of optical intensity. As described previously, α is the optical power to current conversion factor, I_o is the intensity of the optical source, and R_L is the load resistance of the photodetector. $\psi(\nu)$ is the spectral envelope function of the optical PSD, normalised to unit power and shifted to a centre frequency of zero. The following parameters are used in the program:

Parameter	Value
α	608 A/W
R_L	50 Ω
I_0	-20 dBm

Appendix B

Travelling-Wave SOA Model

This appendix provides additional implementation details of the travelling-wave SOA model, further to that described in Section 3.3.

The Alcatel model 1901 SOA device parameters shown in Table 3.1 were obtained through two main sources. As efforts to directly obtain device parameters from the manufactures proved unsuccessful, we directed our attention on finding 'typical' values reported in literature [31,82]; device length (L), area (A), and the confinement factor (Γ) were such parameters. On the other hand, α_{int}, N_o and τ were determined by the best fit to the experimental steady state gain curve (the input to the SOA was a 30 GHz slice bandwidth), while α was determined by the best fit to the optical PSD. Once these values were determined for the single input slice, they were seen to show good agreement with the wide range of input bandwidths considered throughout this thesis, thus inspiring confidence in our chosen parameters.

A flow chart of the program algorithm is shown on the following page.

Numerical Model Algorithm by Peter Horak

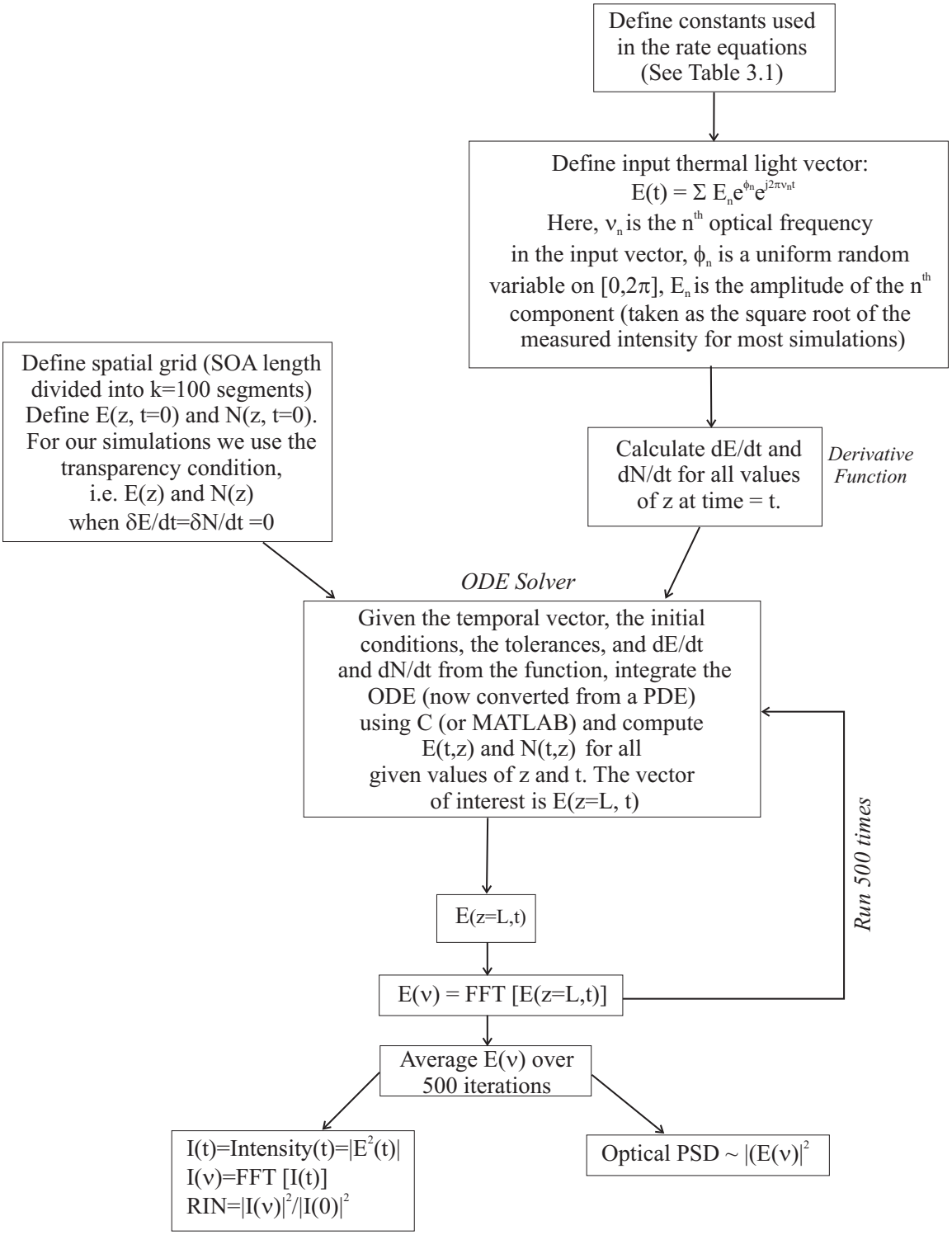

Appendix C

Shaping the Coherence Properties of Incoherent Light

Overview and Background

As a precursor to the OCDMA system experiments described in Chapter 5, my earliest laboratory work focused on characterising the general properties of incoherent broadband light. These efforts are partially documented in Chapter 2. In this appendix, I record my investigations into the temporal coherence properties of filtered thermal light, specifically focusing on how these properties are affected by using filters to slice and shape the available optical bandwidth. Temporal coherence (or longitudinal spatial coherence) is defined as the time over which a constant phase relationship is maintained by an optical signal, and is directly related to the finite bandwidth and spectral shape of the source in consideration [11, 83]. I show here, how customised complex FBG designs can be used to shape the temporal coherence properties of thermal light.

The temporal coherence of a source can be characterised by the interference pattern at the output of an interferometer as the path length difference is varied. This interference pattern is known as the interferogram. It is well known that the *interference fringe visibility*, or the envelope of an interferogram, is equal to the autocorrelation of the input light field. Also, according to the Wiener-Khinchin theorem, the autocorrelation function of an optical disturbance, is the Fourier transform of its

power spectral density. Therefore, light launched into an interferometer will produce a visibility pattern that can be given by the Fourier transform of its power spectral density. When using an incoherent source, this allows a convenient method of creating any desired interference pattern, merely by shaping the spectral properties of the input light. Passive optical filters such as FBGs are particularly well suited for this purpose since they can be used to form a wide range of spectral shapes, allowing the creation of complex time domain visibility patterns. The interferogram pattern at the output of the interferometer (i.e. input to detector), $I_D(\tau)$, is described by Equation C.1 [11].

$$I_D(\tau) = 2K^2 I_0[1 + |\gamma(\tau)|cos(2\pi\bar{\nu} - \alpha(\tau))] \tag{C.1}$$

The complex degree of coherence $\gamma(\tau)$ is given by $\gamma(\tau) = \frac{\Gamma(\tau)}{\Gamma(0)}$, where $\Gamma(\tau)$, the self-coherence function, is defined as the autocorrelation of the input signal. $\alpha(\tau)$ is given by $arg[\gamma(\tau)] + 2\pi t$, while K and $\overline{\nu}$ represents the loss in each path of the interferometer, and the centre frequency of the input spectrum, respectively. Note that the input intensity I_0 equals $\Gamma(0)$. As is clear from Equation C.1, $|\gamma(\tau)|$ gives the envelope of the interferogram pattern which describes the depth of the interference fringes. This envelope can be measured in terms of the fringe visibility, $V(\tau) = |\gamma(\tau)|$, where,

$$V(\tau) = \frac{I_{max} - I_{min}}{I_{max} + I_{min}} \tag{C.2}$$

Here, I_{max} and I_{min} refer to the maximum and minimum of the detected intensity at the output of the interferometer. Therefore, by measuring the fringe visibility, we obtain the envelope of the interferogram, which in turn represents the normalised self-coherence function of the input optical signal. Using the experiment outlined below, I illustrate some of the intricate visibility patterns that can be created using custom FBGs to shape the coherence properties of narrowband thermal light.

Experiment and Results

For this all fibre experiment, I used the output of an EDFA as the ASE source, followed by various FBGs which were used to spectrally carve the broadband spectrum.

The experimental setup is shown in Figure C.1. In order to trace the interferogram envelope, a variable delay line was used to change the relative time delay of the signals in the two different arms of the interferometer. The piezo-electric device shown in the figure was used as a full-wavelength phase-shifter to ensure accurate capture of the minimum and maximum intensity of the interferogram pattern, reducing the impact of temperature fluctuations on the visibility measurement. A high extinction polariser was used at the input to the MZI, in order to minimise errors caused by the intrinsic birefringence of the fibre, while the polarisation controllers assisted in minimising polarisation-induced errors. The variable optical attenuator was used to match the powers in both arms of the interferometer. The output of the MZI was then detected using a 125 MHz low noise receiver and measured using a digital oscilloscope.

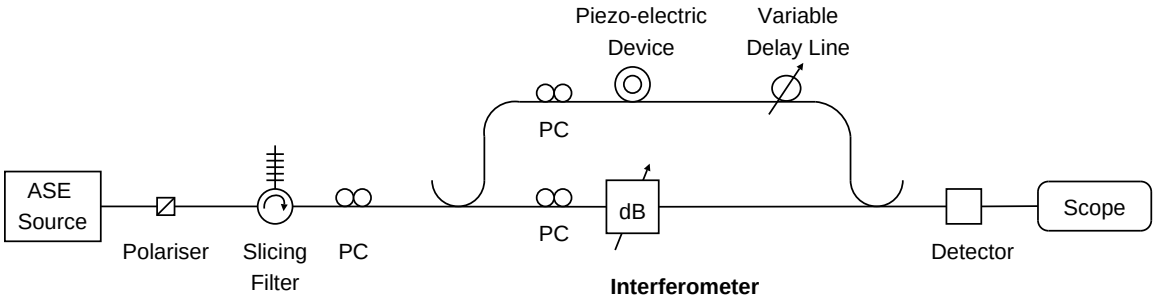

Figure C.1: Laboratory setup to measure the visibility of narrowband thermal light.

The time domain visibility patterns for four different lineshaping FBGs are presented in Figure C.2, alongside the corresponding grating reflection spectra. As expected, the experimental and predicted results are seen to be in excellent agreement with each other. Note that the full visibility pattern was not recorded for grating (c), due to the limited length of the variable delay line. Also, the slight misalignment observed in the fringe envelope for grating (b) is attributed to the limited resolution of the measurement apparatus.

As mentioned previously, the measured visibility can be used to calculate the

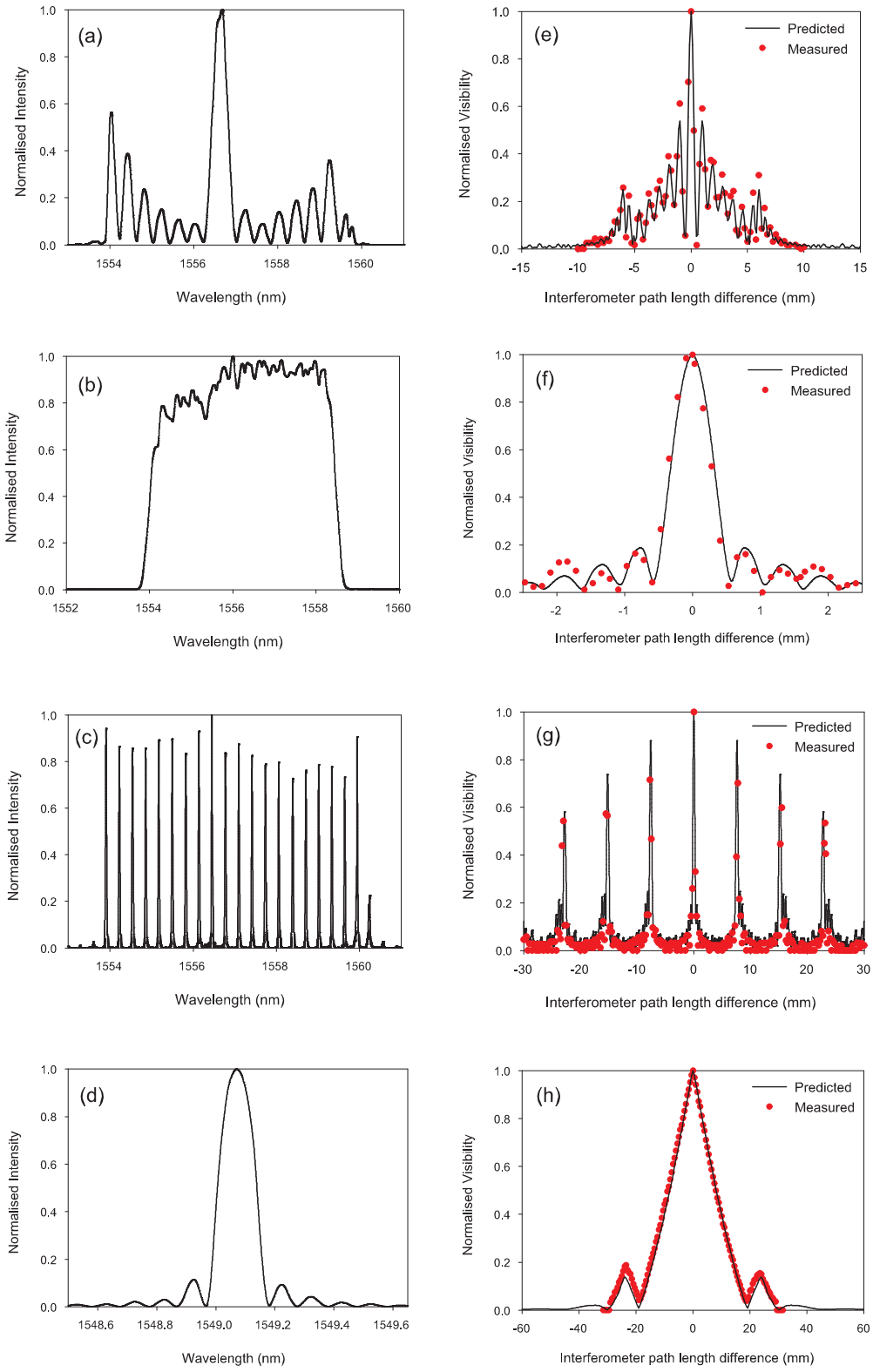

Figure C.2: Spectral traces and time domain visibility patterns for three different gratings. (a), (b), (c) and (d) show the optical spectrum analyser traces of three different gratings, and (e), (f), (g) and (h) show the corresponding time domain visibility patterns.

coherence time, τ_c, for the narrowband light launched into the interferometer [11]:

$$\tau_c = \int_{-\infty}^{\infty} |\gamma(\tau)|^2 d\tau \tag{C.3}$$

(Note that several alternative definitions are also available in the literature). Here, $|\gamma(\tau)|$ is the measured visibility pattern. Equation C.3 takes into account both the bandwidth and shape of the filtered spectra, and requires the full visibility pattern of the interferogram in order to obtain an accurate value for the coherence time. Using the above definition, the coherence time and length were calculated for the different fringe patterns (see Table C.1). Grating (c) was not included in this comparison as sufficient data points were not available due to the limitation of the measurement apparatus. It is clear from these results that the temporal coherence of a filtered thermal source is related to the spectral width and shape of the optical filter, with increasing linewidth giving rise to decreased coherence time. This study illustrates the ability to shape the coherence properties of incoherent light using complex FBGs and could have potential application in areas such as optical coherence tomography which require low-coherence interferometric techniques.

Table C.1: Coherence length comparison

Grating	Bandwidth (3 dB)	Time (ps)	Length (mm)
d	0.1	38	11.3
a	0.4	3.9	1.2
b	4.5	1.77	0.53

Appendix D

SOA Specifications

This appendix contains the data sheets of the three SOAs (Alcatel 1901A, JDS Uniphase CQF874-308C and the JDS Uniphase CQF872-308C) used in this thesis. More details on the JDS Uniphase CQF series SOAs are available at www.jdsu.com. Note that all SOA models used herein, have since been discontinued.

ALCATEL
OPTRONICS

MAIN CHARACTERISTICS OF SOA AMPLIFIER MODULE

Typical performance specifications

- Fibre to fibre gain	:	≥ 20 dB
- TE/TM differential gain	:	≤ 1,5 dB
- "Ripple"	:	≤ 0,5 dB
- Saturation power Psat	:	≥ 7 dBm at 200 mA
- Optical bandwidth	:	30 nm
- Peak gain	:	1530 - 1550 nm
- Maximum forward current	:	250 mA
- On/off switch time	:	≤ 1 ns

Peltier cooler characteristics

- Maximum cooler voltage	:	4 V
- Maximum cooler current	:	1,5 A
- Thermistor resistance	:	10 kΩ at 25 °C

Fiber pigtails :

- Length : 1,50 m
- Mode filed diameter : 10 µm
- Cladding diameter : 125 µm

Figure D.1: Alcatel model 1901A

Specifications

Limiting Values						
Parameter	**Symbol**	**Conditions**	**Min**		**Max**	**Unit**
Optical Amplifier Diode						
Reverse voltage	V_R	-	-		2	V
Forward current	I_F	**CQF874/208**	-		450	mA
		CQF874/308	-		600	mA
Module						
Case operating temperature range	T_{op}	T_{case} = 25 °C, I_{op} = 300 mA	-5		70	°C
Storage temperature range	T_{stg}	-	-40		85	°C
Fiber Pigtail						
Bending radius	R	-	35		-	mm
Tensile strength fiber to case	F	-	-		5	N
Additional Characteristics (R_{ss} = 10 kΩ unless otherwise specified)						
Parameter	**Symbol**	**Conditions**	**Min**	**Typ**	**Max**	**Unit**
Optical Amplifier Diode						
Gain bandwidth	BW	**CQF874/208,** 3 dB bandwidth	50	80	-	nm
		CQF874/308, 3 dB bandwidth	50	70	-	nm
Fiber-to-fiber gain	G_{ff}	**CQF874/208,** 1525 nm - 1565 nm	15	17	-	dB
		CQF874/308, 1525 nm - 1565 nm	20	22	-	dB
Operating current	I_{op}	**CQF874/208**	-	250	-	mA
		CQF874/308	-	300	-	mA
3 dB saturation output power (CW)	P_{3dB}	1545 nm	9	10	-	dBm
Gain ripple	ΔG_{ff}	1525 nm - 1565 nm	-	< 0.5	1.0	dB
Gain peak wavelength	λ_{gain}	-	-	1530	-	nm
Optical noise figure	NF	Fiber-to-fiber (P_{in} = -25 dBm)	-	8	9	dB
Polarisation dependent gain	PDG	1525 nm - 1565 nm	-	< 1.0	1.5	dB
Forward voltage	V_F	-	-	-	2.25	V
Thermistor						
Resistance	R_{th}	T_{th} = 25 °C	9.5	10	10.5	kΩ
Thermistor constant	B	-	3800	-	4100	K
Thermoelectric Cooler (ΔT = 45 °C)						
Cooler current	I_{cool}	-	-	1.1	1.3	A
Cooler voltage	V_{cool}	-	-	2.5	3.0	V
Optical Isolator						
Isolation	ISO	1525 nm - 1565 nm	29	-	-	dB
Polarization mode dispersion	PMD	-	-	-	0.20	ps
Single Mode Fiber Pigtail						
Mode field diameter	$Ø_{mf}$	-	-	10.5	-	µm
Outer diameter of tight buffer	$Ø_{tb}$	-	-	250	-	µm
Outer diameter of loose tube	$Ø_{lt}$	-	-	900	-	µm
Length of pigtail	-	-	1	-	-	m

Figure D.2: JDS Uniphase model CQF874-308C

Specifications

Limiting Values						
Parameter	**Symbol**	**Conditions**	**Min**		**Max**	**Unit**
Optical Amplifier Diode						
Reverse voltage	V_R	-	-		2	V
Forward current	I_F	**CQF872/208**	-		450	mA
		CQF872/308	-		600	mA
Module						
Case operating temperature range	T_{op}	T_{chip} = 25 °C, I_{op} = 300 mA	-5		70	°C
Storage temperature range	T_{stg}	-	-40		85	°C
Fiber Pigtail						
Bending radius	R	-	35		-	mm
Tensile strength fiber to case	F	-	-		5	N
Additional Characteristics (R_{th} = 10 kW unless otherwise specified)						
Parameter	**Symbol**	**Conditions**	**Min**	**Typ**	**Max**	**Unit**
Optical Amplifier Diode						
Gain bandwidth	BW	**CQF872/208,** 3 dB bandwidth	50	80	-	nm
		CQF872/308, 3 dB bandwidth	50	70	-	nm
Fiber-to-fiber gain	G_{ff}	**CQF872/208,** 1525 nm - 1565 nm	15	17	-	dB
		CQF872/308, 1525 nm - 1565 nm	20	22	-	dB
Operating current	I_{op}	**CQF872/208**	-	250	-	mA
		CQF872/308	-	300	-	mA
3 dB saturation output power (CW)	P_{3dB}	1545 nm	9	10	-	dBm
Gain ripple	ΔG_{flat}	1525 nm - 1565 nm	-	< 0.5	1.0	dB
Gain peak wavelength	λ_{peak}	-	-	1530	-	nm
Optical noise figure	NF	Fiber-to-fiber (P_{in} = -25 dBm)	-	8	9	dB
Polarisation dependent gain	PDG	1525 nm - 1565 nm	-	< 1.0	1.5	dB
Forward voltage	V_F	-	-	-	2.25	V
Thermistor						
Resistance	R_{th}	T_{th} = 25 °C	9.5	10	10.5	kΩ
Thermistor constant	B	-	3800	-	4100	K
Thermoelectric Cooler (ΔT = 45 °C)						
Cooler current	I_{cool}	-	-	1.1	1.3	A
Cooler voltage	V_{cool}	-	-	2.5	3.0	V
Single Mode Fiber Pigtail						
Mode field diameter	$Ø_{mf}$	-	-	9.0	-	µm
Outer diameter of tight buffer	$Ø_{tc}$	-	-	900	-	µm
Length of pigtail	-	-	1	-	-	m

Figure D.3: JDS Uniphase model CQF872-308C

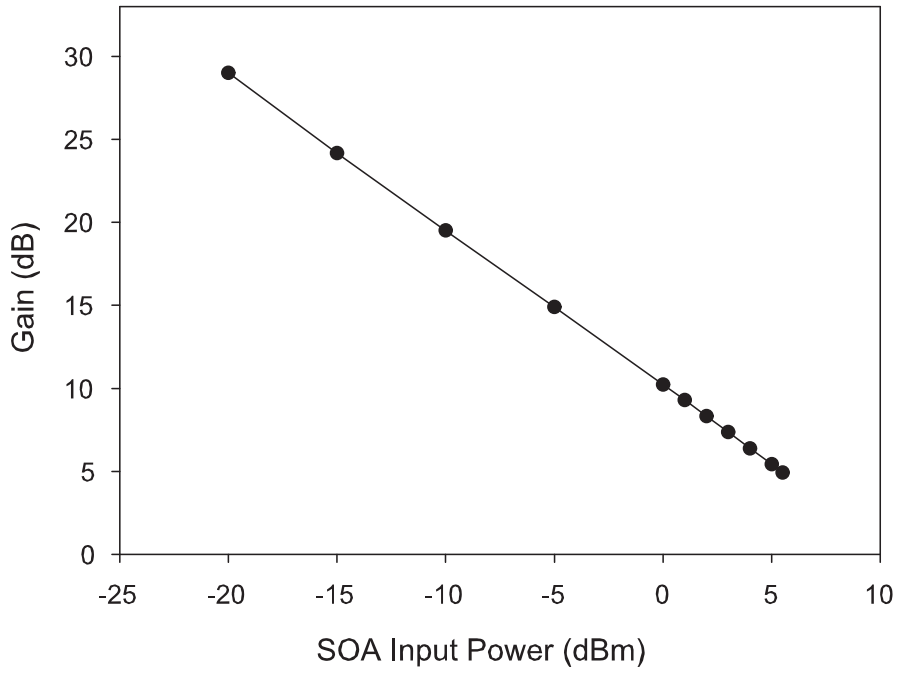

Figure D.4: Measured gain curve for the Alcatel model 1901 at a pump current of 200 mA

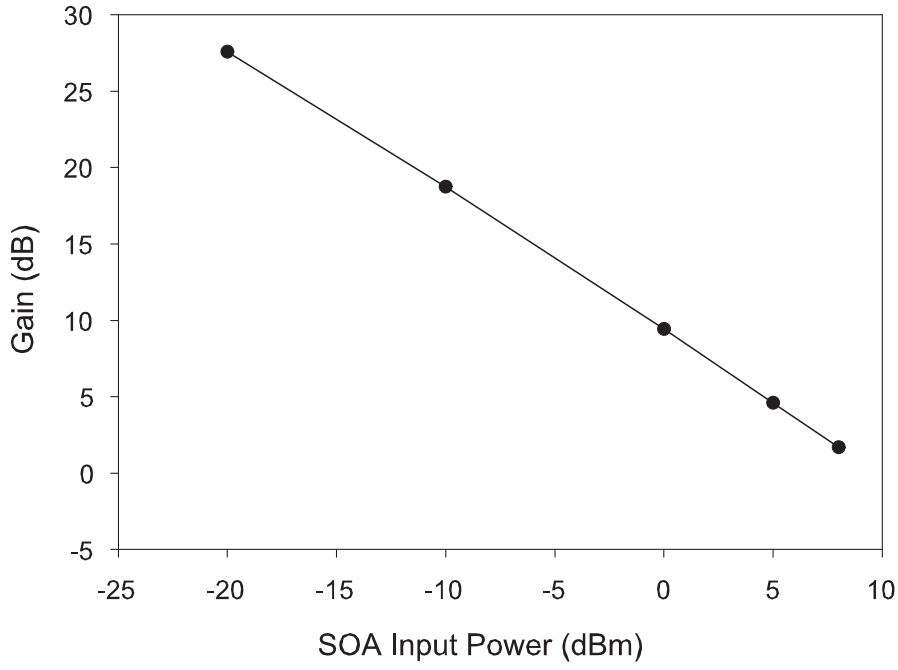

Figure D.5: Measured gain curve for the JDS CQF874 at a pump current of 450 mA

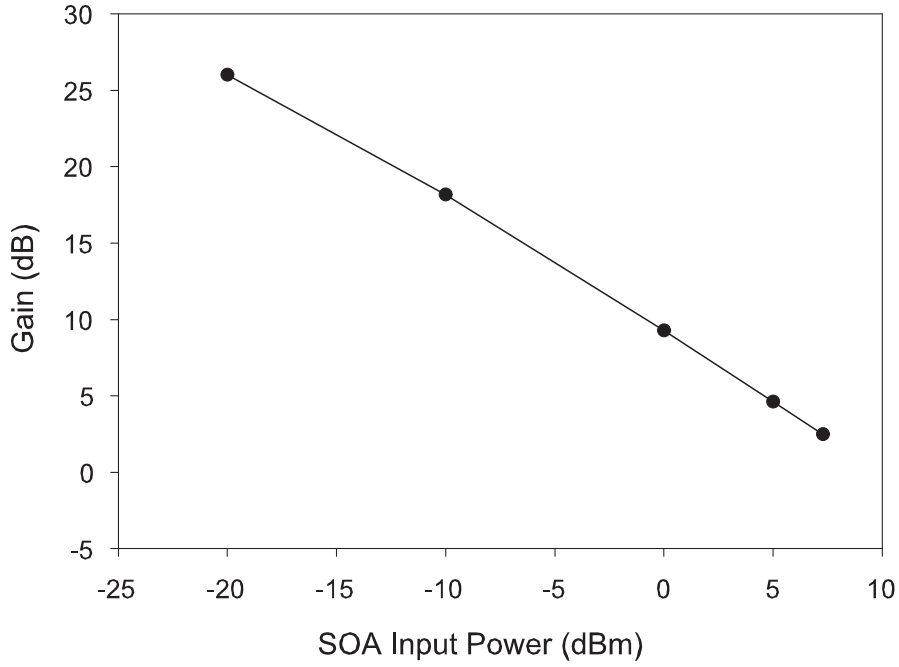

Figure D.6: Measured gain curve for the JDS CQF872 at a pump current of 450 mA

Bibliography

[1] G. Agrawal. *Fiber-Optic Communication Systems*. John Wiley & Sons, inc., 3rd edition, 2002.

[2] B. Whitman and M. Kunigonis. Fibre Access Deployment Worldwide – Market Drivers, Politics and Technology Choices. In *Proc. European Conf. on Opt. Comm. (ECOC) 2004, paper Mo3.1.2*, pages 6–9, 2004.

[3] J. Campbell. Coarse WDM makes waves in metro/access markets. *WDM Solutions*, November 2000.

[4] J.-J. Petiote. Low-cost components give coarse WDM an edge. *WDM Solutions*, January 2001.

[5] G.J. Pendock and D.D. Sampson. Transmission Performance of High Bit Rate Spectrum-Sliced WDM systems. *IEEE Journal of Lightwave Technology*, 14(10):2141–2148, 1996.

[6] K. Kitayama, H. Sotobayashi, and N. Wada. Optical Code Division Multiplexing (OCDM) and Its Applications to Photonic Networks. *IEICE Trans. Fundamentals*, E82 A(12), 1999.

[7] S.S. Wagner and T.E. Chapuran. Broadband High-density WDM Transmission Using Superluminescent Diodes. *Electronics Letters*, 26(11):696–697, 1990.

[8] S.-J. Kim, J.-H. Han, J.-S. Lee, and C.-S. Park. Suppression of Intensity Noise in 10Gb/s Spectrum-Sliced Incoherent Light Channel Using Gain-Saturated Semiconductor Optical Amplifiers. *Electronics Letters*, 35(12):1000–1001, 1999.

[9] T. Pfeiffer et al. Coarse WDM/CDM/TDM concept for optical packet transmission in metropolitan and access networks supporting 400 channels at 2.5 Gb/s peak rate. *IEEE Journal of Lightwave Technology*, 18(12):1928–1938, 2000.

[10] F. Koyama, T. Yamatoya, and K. Iga. Highly Gain-Saturated GaInAsP/InP SOA Modulator for Spectrum-Sliced Light Source. In *Conference on Indium Phosphide and Related Materials*, pages 439–442, 2000.

[11] J.W. Goodman. *Statistical Optics*. John Wiley & Sons, Inc., 2000.

[12] H. Hodara. Statistics of Thermal and Laser Radiation. In *Proceedings of the IEEE*, volume 53, pages 696–704, 1965.

[13] G.-H. Duan and E. Georgiev. Non-White Photodetection Noise at the Output of an Optical Amplifier. *IEEE Journal of Quantum Electronics*, 37(8):1008–1014, 2001.

[14] H.S. Kim, R.P.H. Haaksman, T.P. Newson, and D.J. Richardson. Noise Properties and Phase Resolution of Interferometer Systems Interrogated by Narrowband Fiber ASE Sources. *IEEE Journal of Lightwave Technology*, 17(11):2327–2335, 1999.

[15] D. Derickson, editor. *Fiber Optic Test and Measurement*. Hewlett-Packard Professional Books. Prentice Hall PTR.

[16] B.N. Taylor and C.E. Kuyatt. Guidelines for Evaluating and Expressing the Uncertainty of NIST Measurement Results. Technical Note 1297, National Institute of Standards and Technology (NIST), September 1994.

[17] P.R. Morkel, R.I. Laming, and D.N. Payne. Noise Characteristics of High-Power Doped-Fibre Superluminescent Sources. *Electronics Letters*, 26(2):96–98, 1990.

[18] P.R. Morkel, R.I. Laming, H.O. Edwards, and D.N. Payne. Elimination of Excess Photon Noise from Fibre Super-Radiant Sources. In *Proc. Conference on Lasers and Electro-optics (CLEO), paper TUH76*, pages 154–155, 1990.

[19] A.J. Keating, W.T. Holloway, and D.D. Sampson. Feedforward Noise Reduction of Incoherent Light for Spectrum-Sliced Tranmission at 2.5 Gb/s. *IEEE Photonics Technology Letters*, 7(12):1513–1515, 1995.

[20] J.-H. Han, J.-W. Ko, J.-S. Lee, and S.-Y. Shin. 0.1-nm Narrow Bandwidth Transmission of a 2.5 Gb/s Spectrum-Sliced Incoherent Light Channel Using an All-Optical Bandwidth Expansion Technique at the Receiver. *IEEE Photonics Technology Letters*, 10(10):1501–1503, 1998.

[21] F. Koyama. High Power Superluminescent Diodes for Multi-Wavelength Light Source. In *IEEE LEOS Annu. Meeting, paper TuY2*, pages 333–334, 1999.

[22] S.-J. Kim, J.-H. Han, J.-S. Lee, and C.-S. Park. Intensity Noise Suppression in Spectrum-Sliced Incoherent Light Communication Systems Using a Gain Saturated Semiconductor Optical Amplifier. *IEEE Photonics Technology Letters*, 11(8):1042–1044, 1999.

[23] M. Zhao, G. Morthier, and R. Baets. Analysis and Optimization of Intensity Noise Reduction in Spectrum-Sliced WDM Systems Using a Saturated Semiconductor Optical Amplifier. *IEEE Photonics Technology Letters*, 14(3):390–392, 2002.

[24] J.E. Carroll. *Rate Equations in Semiconductor Electronics*. Cambridge University Press, 1990.

[25] M.E. Bray and M.J. O'Mahony. Cascading Gain-Saturation Semiconductor Laser-Amplifier Wavelength Translators. In *IEE Proceedings in Optoelectronics*, volume 143, pages 1–6, 1996.

[26] L.A. Coldren and S.W. Corzine. *Diode Lasers and Photonic Integrated Circuits*. John Wiley & Sons, Inc., 1995.

[27] M. Shtaif and G. Eisenstein. Noise Properties of Nonlinear Semiconductor Optical Amplifiers. *Optics Letters*, 21(22):1851–1853, 1996.

[28] L. Kazovsky, S. Benedetto, and A. Willner. *Optical Fiber Communication Systems*. Artech House, 1996.

[29] A.D. McCoy, B.C. Thomsen, M. Ibsen, and D.J. Richardson. Experimental Study on Receiver Filtering Effects in a Spectrum-Sliced Incoherent Light WDM System Using SOA Based Noise Reduction. In *Proc. European Conf. on Opt. Comm. (ECOC) 2003, paper We4P155*, pages 866–867, 2003.

[30] M. Munroe, J. Cooper, and M.G. Raymer. Spectral Broadening of Stochastic Light Intensity-Smoothed by a Saturated Semiconductor Optical Amplifier. *IEEE Journal of Quantum Electronics*, 34:548–551, 1998.

[31] G.P. Agrawal and N.A. Olsson. Self-Phase Modulation and Spectral Broadening of Optical Pulses in Semiconductor Laser Amplifiers. *IEEE Journal of Quantum Electronics*, 25(11):2297–2306, 1989.

[32] S. Diez, C. Schmidt, R. Ludwig, H.G. Weber, K. Obermann, S. Kindt, I. Koltchanov, and K. Petermann. Four-Wave Mixing in Semiconductor Optical Amplifiers for Frequency Conversion and Fast Optical Switching. *IEEE Journal of Quantum Electronics*, 3:1131–1145, 1997.

[33] R.W. Boyd. *Nonlinear Optics*. Elsevier Science, 2nd edition, 2003.

[34] G. Agrawal. *Nonlinear Fiber Optics*. Academic Press, 4th edition, 2003.

[35] M. Shtaif and G. Eisenstein. Experimental Study of the Statistical Properties of Nonlinearly Amplified Signals in Semiconductor Optical Amplifiers. *IEEE Photonics Technology Letters*, 9(7):904–906, 1997.

[36] M. Shtaif and G. Eisenstein. Noise Characteristics of Nonlinear Semiconductor Optical Amplifiers in the Gaussian Limit. *IEEE Journal of Quantum Electronics*, 32:1801–1809, 1996.

[37] A. Papoulis. *Probability, Random Variables, and Stochastic Processes*. McGraw-Hill, Inc., 3rd edition, 1991.

[38] M.P. Mullane and J.G. McInerney. Sensitivity of the Linewidth Enhancement Factor to Structure and Threshold Level in Strained Semiconductor Lasers. In *Proc. Conference on Lasers and Electro-optics (CLEO), paper CTuA60*, pages 180–181, 2000.

[39] D.J. Gallant J. Stohs, D.J. Bossert and S.R.J. Brueck. Gain, Refractive Index Change, and Linewidth Enhancement Factor in Broad-Area GaAs and InGaAs Quantum-Well Lasers. *IEEE Journal of Quantum Electronics*, 37:1449–1459, 2001.

[40] A.D. McCoy, P. Horak, B.C. Thomsen, M. Ibsen, M.R. Mokhtar, and D.J. Richardson. Improving Signal Quality in a Spectrum-Sliced WDM System Using SOA-Based Noise Reduction. *IEEE Photonics Technology Letters*, 17(1):241–243, 2005.

[41] T.W. Berg and J. Mørk. Ultrafast Optical Signal Processing using Semiconductor Quantum Dot Amplifiers. In *IEEE LEOS Annu. Meeting, paper TuZ2*, pages 321–322, 2002.

[42] J.S. Lee, Y.C. Chung, and D.J. DiGiovanni. Spectrum-Sliced Fiber Amplifier Light Source for Multichannel WDM Applications. *IEEE Photonics Technology Letters*, 5(12):1458–1461, 1993.

[43] L. Boivin, M. Wegmuller, M.C. Nuss, W.H. Knox, Y. Sun, A.K. Srivastava, J.W. Sulhoff, and C. Wolf. Transmission over 362 km of 110 Channels at 2.35 Gb/s from a Spectrum-Sliced Femtosecond Laser. *IEEE Photonics Technology Letters*, 11(10):1319–1321, 1999.

[44] M.H. Reeve, A.R. Hunwicks, W. Zhao, S.G. Methley, L. Bickers, and S. Hornung. LED Spectral Slicing For Single-Mode Local Loop Applications. *Electronics Letters*, 24(7):389–390, 1988.

[45] P. Healey, P. Townsend, C. Ford, L. Johnston, P. Townley, I. Lealman, L. Rivers, S. Perrin, and R. Moore. Spectral slicing WDM-PON using Wavelength-seeded reflective SOAs. *Electronics Letters*, 37(19):1181–1182, 2001.

[46] A.D. McCoy, B.C. Thomsen, M. Ibsen, and D.J. Richardson. Filtering Effects in a Spectrum-Sliced Incoherent Light WDM System Using SOA Based Noise Reduction. *IEEE Photonics Technology Letters*, 16(2):680–682, 2004.

[47] K. Akimoto, J. Kani, M. Teshima, and K. Iwatsuki. Spectrum-Sliced 25-GHz spaced, 155 Mb/s x 32 channel WDM access. In *Proc. Conf. on Lasers and Electro-optics (CLEO) 2001*, pages II:556–557, 2001.

[48] http://www.hytek.com/pdf/hy6410.pdf.

[49] T.-Y. Kim, S.-J. Kim, and C.-S. Park. Intensity Noise Suppression of 2.5 Gb/s Spectrum-Sliced Incoherent Signal Using a Gain-Saturated SOA Injected by Broadband Light. In *Proc. Optoelectronics Communications Conference (OECC)*, pages 46–47, 2004.

[50] T. Yamatoya and F. Koyama. Optical Preamplifer Using Optical Modulation of Amplified Spontaneous Emission in Saturated Semiconductor Optical Amplifier. *IEEE Journal of Lightwave Technology*, 22(5):1290–1295, 2004.

[51] M. Menif, P. Lemieux, W. Mathlouthi, and L.A. Rusch. Error-Free Transmission for Incoherent Broad-Band Optical Communications Systems Using Incoherent-to-Coherent Wavelength Conversion. *IEEE Journal of Lightwave Technology*, 23(1):287–294, 2005.

[52] G. Keiser. *Fiber Optic Communication Systems*. McGraw-Hill Series in Electrical and Computer Engineering, 3rd edition, 2000.

[53] B. Sklar. *Digital Communications: Fundamentals and Applications*. Englewood Cliffs, NJ:PTR Prentice Hall Inc., 1988.

[54] J.G. Proakis. *Digital Communications*. McGraw-Hill Series in Electrical and Computer Engineering, 3rd edition, 1995.

[55] J.G. Proakis and D.G. Manolakis. *Digital Signal Processing, Principles, Algorithms and Applications*. Prentice Hall Inc., 3rd edition, 1996.

[56] H. Fathallah, L.A. Rusch, and S. LaRochelle. Passive Optical Fast Frequency-hop CDMA Communications System. *IEEE Journal of Lightwave Technology*, 17(3):397–405, 1999.

[57] E.H. Dinan and B. Jabbari. Spreading Codes for Direct Sequence CDMA and Wideband CDMA Cellular Networks. *IEEE communications*, pages 48–54, 1998.

[58] A.J. Viterbi. *CDMA Principles of Spread Spectrum.* Addison-Wesley Wireless Communications Series, 1995.

[59] C.F. Iam. To Spread or Not to Spread - the Myths of Optical CDMA. In *Optical Fiber Communications Conference (OFC)*, pages TuV6–1 – TuV6–3 Vol.2, 2001.

[60] H.P. Sardesai, C.C. Chang, and A.M. Weiner. A Femtosecond Code-Division Multiple-Access Communication System Test Bed. *IEEE Journal of Lightwave Technology*, 16(11):1953–1964, 1998.

[61] R.A. Griffin, D.D. Sampson, and D.A. Jackson. Demonstration of Data Transmission Using Coherent Correlation to Reconstruct a Coded Pulse Sequence. *IEEE Photonics Technology Letters*, 4(5):513–515, 1992.

[62] D. Zaccarin and M. Kavehrad. An optical CDMA system based on spectral encoding of LED. *IEEE Photonics Technology Letters*, 5(4):479–482, 1993.

[63] N. Karafolas and D. Uttamchandani. Optical Fiber Code Division Multiple Access Networks: A Review. *Optical Fiber Technology*, 2(2):149–168, 1996.

[64] M. Kavehrad and D. Zaccarin. Optical Code-Division-Multiplexed Systems Based on Spectral Encoding of Noncoherent Sources. *IEEE Journal of Lightwave Technology*, 13(3):534–545, 1995.

[65] X. Zhou et al. Code for Spectral Amplitude Coding Optical CDMA Systems. *Electronics Letters*, 36(8):728–729, 2000.

[66] J.A. Salehi, A.M. Weiner, and J.P. Heritage. Coherent Ultrashort Light Pulse Code-Division Multiple Access Communication Systems. *IEEE Journal of Lightwave Technology*, 8(3):478–491, 1990.

[67] Z. Wei, H.M.H. Shalaby, and H. Ghafouri-Shiraz. Modified Quadratic Congruence Codes for Fiber Bragg-Grating-Based Spectral-Amplitude-Coding Optical CDMA systems. *IEEE Journal of Lightwave Technology*, 19(9):1274–1281, 2001.

[68] Z. Wei, H. Ghafouri-Shiraz, and H.M.H. Shalaby. New Code Families for Fiber-Bragg-Grating-Based Spectral-Amplitude-Coding Optical CDMA Systems. *IEEE Photonics Technology Letters*, 13(8):890–892, 2001.

[69] G.A. Magel, G.D. Landry, R.J. Baca, D.A. Harper, and C.A. Spillers. Transmission of Eight Channels x 622 Mbit/s and 15 Channels x 155 Mbit/s using Spectral Encoded Optical CDMA. *Electronics Letters*, 37(21):1307–1308, 2001.

[70] M. Ibsen, M.K. Durkin, M.J. Cole, and R.I. Laming. Sinc-sampled Fiber Bragg Gratings for Identical Multiple Wavelength Operation. *IEEE Photonics Technology Letters*, 10(6):842–844, 1998.

[71] Attolight Corp., Montréal, Québec, Canada. *AttoReconstructor User Manual*, 2001. www.attolight.com.

[72] S. Taccheo, P. Laporta, O. Svelto, and G. De Geronimo. Theoretical and experimental analysis of intensity noise in a codoped erbium-ytterbium glass laser. *Applied Phys. B*, 66:19–26, 1998.

[73] G. A. Ball, G. Hull-Allen, C. Holten, and W. Morey. Low noise single frequency linear fibre laser. *Electronics Letters*, 29(18):1623–1625, 1993.

[74] Lei Xu, Ivan Glesk, Darren Rand, Varghese Baby, and Paul R. Prucnal. Suppression of beating noise of narrow-linewidth erbium-doped fiber ring lasers by use of a semiconductor optical amplifier. *Optics Letters*, 28(10):780–782, 2003.

[75] A.D. McCoy, L.B. Fu, M. Ibsen, B.C. Thomsen, and D.J. Richardson. Intensity Noise Suppression in Fibre DFB Laser Using Gain Saturated SOA. *Electronics Letters*, 40(2):107–109, 2004.

[76] M. Ibsen, E. Ronnekleiv, G. J. Cowle, M. O. Berendt, O. Hadeler, M N. Zervas, and R. I. Laming. Robust high power (>20mW) all-fibre DFB lasers with unidirectional and truly single polarisation outputs. In *Proc. Conference on Lasers and Electro-optics (CLEO), paper CWE4*, 1999.

[77] J. L. Brooks, M. Tur, B. Y. Kim, K. A. Fesler, and H. J. Shaw. Fiber-optic interferometric sensor arrays with freedom from source phase-induced noise. *Optics Letters*, 11(7):473–475, 1986.

[78] V.N. Yoong. Single-Frequency Fibre Lasers for Optical Networks. 15-month report, Optoelectronics Research Centre, University of Southampton, August 2004.

[79] VPI Photonics, Holmdel, New Jersey. *VPI Transmission Maker User Manual*, March 2003. www.VPIphotonics.com.

[80] M. Sugawara, N. Hatori, T. Akiyama, Y. Nakata, and H. Ishikawa. Quantum-dot semiconductor optical amplifiers for high bit-rate signal processing over 40 Gbit/s. In *Proc. Conference on Lasers and Electro-optics (CLEO), paper TuA1-5*, pages 260–262, 2001.

[81] K.E. Stubkjaer. Nonlinear gain dynamics in quantum-dot optical amplifiers and its application to optical communication devices. *IEEE Journal on Selected Topics in Quantum Electronics*, 6(6):1059–1065, 2000.

[82] J.-J. Bernard and Monique Renaud. Semiconductor optical amplifiers. *SPIE OE Magazine*, pages 36–38, September 2001.

[83] E. Hecht. *Optics*. Addison Wesley Longman, Inc., 4th edition, 2002.

List of Publications

- **A.D. McCoy**, B.C. Thomsen, M. Ibsen and D.J. Richardson, Experimental Study on Receiver Filtering Effects in a Spectrum-Sliced Incoherent Light WDM System Using SOA Based Noise Reduction, *In Proc. European Conf. on Opt. Comm. (ECOC) 2003, paper We4P155*, pp. 866-867.

- **Anoma D. McCoy**, L. B. Fu, M. Ibsen, Benn C. Thomsen and D. J. Richardson, Intensity Noise Suppression in fibre DFB laser Using gain saturated SOA, *Electronics Letters*, Vol.40, pp. 107-108, 2004.

- **A.D. McCoy**, B.C. Thomsen, M. Ibsen and D.J. Richardson, Filtering Effects in a Spectrum-Sliced WDM System Using SOA Based Noise Reduction, *IEEE Photonics Technology Letters*, Vol. 16, pp. 680-682, 2004.

- **Anoma D. McCoy**, L. B. Fu, M. Ibsen, Benn C. Thomsen and D. J. Richardson, Relaxation Oscillation Noise Suppression in Fibre DFB Lasers Using a Semiconductor Optical Amplifier, *In Proc. Conference on Lasers and Electro-optics (CLEO) 2004, paper CWA56.*

- **A. D. McCoy**, P. Horak, B.C. Thomsen, M. Ibsen, M. R. Mokhtar and D.J. Richardson, Optimisations for Improved Signal Quality in a Spectrum-Sliced WDM System Using SOA-Based Noise Reduction, *Proc. European Conf. on Opt. Comm. (ECOC) 2004, paper Tu4.6.4* pp.274-275.

- **Anoma D. McCoy**, P. Horak, M. Ibsen, B.C. Thomsen and D.J. Richardson, Intensity noise reduction of incoherent sources using semiconductor optical amplifiers, *In Asilomar Conference on Signals, Systems and Computers 2004*, (Invited paper).

- **A. D. McCoy**, P. Horak, B.C. Thomsen, M. Ibsen, M.R. Mokhtar and D.J. Richardson, Improving Signal Quality in a Spectrum-Sliced WDM System Using SOA-Based Noise Reduction, *IEEE Photonics Technology Letters*, Vol.17 (1), pp.241-243, 2005.

- **Anoma D. McCoy**, P. Horak, B.C. Thomsen, M. Ibsen and D.J. Richardson, Noise Suppression of Incoherent Light Using a Gain Saturated SOA: Implications for spectrum-sliced WDM systems, *IEEE Journal of Lightwave Technology*, (accepted for publication).